UNIVERSIDAD NACIONAL AUTÓNOMA DE MÉXICO

PROGRAMA DE MAESTRÍA Y DOCTORADO EN INGENIERÍA
INGENIERÍA CIVIL – HIDRÁULICA

Modelo numérico para la evaluación de zonas de inundación inducida por marea de tormenta y tsunamis

TESIS
QUE PARA OPTAR POR EL GRADO DE:
DOCTOR EN INGENIERÍA

PRESENTA:
Sébastien de BRYE

TUTOR PRINCIPAL
Dr. Rodolfo Silva Casarín, Instituto de Ingeniería
COMITÉ TUTOR
Dr. Óscar Fuentes Mariles, Instituto de Ingeniería
Dr. Carlos A. Escalante Sandoval, Facultad de Ingeniería
Dr. Moisés Berezowsky Verduzco, Instituto de Ingeniería
Dr. Edgar Gerardo Mendoza Baldwin, Instituto de Ingeniería

MÉXICO D.F., abril 2013

Jurado asignado

Presidente:	Dr. Oscar Fuentes Mariles
Secretario:	Dr. Carlos A. Escalante Sandoval
Vocal:	Dr. Rodolfo Silva Casarín
1er Suplente:	Dr. Moisés Berezowsky Verduzco
2do Suplente:	Dr. Edgar Gerardo Mendoza Baldwin

Lugar donde se realizó la tesis
Instituto de Ingeniería
Universidad Nacional Autónoma de México
Circuito Escolar s/n, Ciudad Universitaria
Delegación Coyoacán, C.P. 04510
México Distrito Federal
MÉXICO

Tutor de tesis
Dr. Rodolfo Silva Casarín

Pour mes parents, mes grand-parents et mes frères,
qui sont tout simplement ma fierté.

Agradecimientos

A la UNAM y al Instituto de Ingeniería por abrirme sus puertas y darme esa oportunidad como extranjero de proseguir mis estudios en el campus Ciudad Universitaria de México.

Al Posgrado de la Facultad de Ingeniería y a su querido personal por su gran ayuda con los trámites, y por haber hecho posible poder llegar a la meta.

Al Consejo Nacional de Ciencia y Tecnología (CONACyT) por brindarme el apoyo económico, esencial a la realización de mis estudios de doctorado.

Al Doctor Rodolfo Silva por su paciencia, su confianza y por haberme alentado hasta el final. Gracias también por haber sido un ejemplo durante esos años con tu admirable y apasionada dedicación al trabajo. Un agradecimiento particular a tu esposa Jill Taylor por su apoyo constante y desinteresado al momento de redactar en inglés.

Al Doctor Edgar Mendoza por su apoyo y por ser un buen amigo. Gracias por haberme ayudado a madurar en el plan profesional y por los muy buenos momentos compartidos.

A los Doctores Carlos Escalante, Óscar Fuentes y Moisés Berezowsky por haber seguido esta investigación y por sus sugerencias y comentarios en la culminación de la tesis.

Un premier remerciement particulier au Professeur Rémi Abgrall pour les quelques minutes qu'il a pu m'accordées et pour son aide décisive quant à la réalisation de ce travail.

Professor Maarten Dingemans of Delft Hydraulics is also gratefully acknowledged for providing the experimental data sets of the "Wave evolution over a submerged bar" test case.

Un especial agradecimiento al Doctor Adrián Pedrozo por aportarme su apoyo incondicional en un momento clave y de ahí ser parte de mi investigación. Muchas gracias por dedicarme tiempo y atención, proporcionarme valiosos consejos y orientación profesional, y finalmente por convertirte en un buen amigo.

Bien sûr, une grande dédicace et très sincère reconnaissance à ma famille et tout particulièrement mes parents, grand-parents maternels et frangins adorés, sans qui je ne serais rien ni personne. Je ne saurais trouver les mots pour extérioriser mes pensées et vous remercier de m'avoir inculqué ces grands principes et valeurs de la vie que j'essaie de suivre au quotidien.

Cet effort, c'est beaucoup à vous que je le dois, merci du fond du cœur de m'avoir toujours soutenu malgré la distance et encouragé jusqu'au bout. Je vous aime tous très fort.

Un pensamiento también a los que fueron mi segunda familia acá en México, mi hermano Albert, Jeka, Marce, Pily, Juan, Nat, Ale, Lalo y Remzy, con quienes he tenido el placer de compartir un hogar. A mis amigos del gym, don Arthur, Hugo el chino, Georges, Rodro el taysoncito y el Benjas, gracias por la buena actitud deportista de siempre y el cotorreo chilo.

Y bueno pues para el final, un profundo agradecimiento a mis camaradas y amigos del II-UNAM que tengo el privilegio de conocer. De generación en generación, algunos se han convertido en grandes amistades y dejaron su marca en mi corazón para siempre. El papá Goyo, Germán y Diana, el Gabo, Angie, mi pariente Gerard y Bella, Brayan, mi carnal Sergio el borre y Cindy, James, Dalila, diime Raúl, mi hermano el Cuau y Gabi, Abril, mi primo el paru Jair, Gibrán el pariente, el compa Miguel, Mireille, Itxaso, Ruby, mijo Miguel, Juan Pablo y Leila, César el chicharrín, el Toño, Pedro, Alencar el Cayo... Gracias por todo lo que aprendí de ustedes y por las sabias enseñanzas que me llevo. Gracias por llevarme a conocer el México lindo y querido, su pueblo, su tierra, su idioma, su música, su baile, su tradición. Simplemente gracias por haberme soportado todos los días y hacer de esta etapa una experiencia increíble e inolvidable. Un fuerte abrazo para todos.

Resumen

El tema principal de esta investigación está relacionado con la modelación de la propagación de ondas marinas y surge de una cierta manera de una falta de información científica para los tomadores de decisión, al momento de enfrentarse a la amenaza de eventos extremos tal como son las mareas de tormenta o los tsunamis en las costas Mexicanas. De hecho, estos fenómenos marítimos son bastante recurrentes en México y con alta capacidad de tomar vidas humanas y causar serios daños costeros socioeconómicos e inundaciones tierra adentro. De manera más específica, este trabajo pretende implementar una herramienta numérica académica para la simulación de ondas largas. Después de revisar las características y las condiciones de validez de las teorías de onda analíticas así como las técnicas de modelación matemática, se restringe el enfoque en los modelos tipo Boussinesq. Al extender la validez en aguas someras al menos a unas condiciones de aguas intermedias, dichos modelos dispersivos abarcan el campo de aplicación más grande en cuanto a la propagación de ondas marinas, permitiendo así una reproducción fiable de ondas largas hasta relativamente cortas. De ahí, se propone el desarrollo de un modelo tipo Boussinesq de alto orden en dos dimensiones horizontales, lo cual se basa en un sistema de ecuaciones completamente no lineales y dispersivas al primer orden, con una descripción multi-capa de la distribución vertical del flujo. El modelo incluye, al orden de aproximación, los términos de vorticidad vertical en la ecuación de conservación de cantidad de movimiento. Luego se presenta una estimación del error de truncamiento del modelo matemático, en función del número de capas. También se describe una metodología para optimisar las propiedades lineales y no lineales intrínsecas del modelo, a partir de una elección adecuada de las posiciones de las capas y de sus respectivas variables internas de velocidad. Para llevar a cabo la discretización numérica del modelo en una dimensión horizontal, se usa el marco del método de Galerkin discontinuo. En particular, el esquema se basa en un método local de Galerkin discontinuo para la discretización espacial, mientrás que para la discretización temporal se utiliza un algoritmo de Runge-Kutta a variación total decreciente de alto orden. Los flujos numéricos son diseñados para asegurar la estabilidad del esquema. Finalmente, por la simulación de dos casos prueba clásicos de referencia, se valida el solucionador numérico en el caso de una capa. En primer lugar, se considera la propagación de tres ondas solitarias sobre un fondo plano con diferente no linealidad. La presencia de un tren dispersivo de ondas cortas es detectada detrás de los solitones no lineales y confirmada por un modelo RANS. En segundo lugar, son reproducidos dos escenarios de dispersión de onda sobre una barra sumergida. El impacto del orden de precisión sobre la solución calculada es además examinado. El modelo de una capa muestra un buen comportamiento para ondas débilmente dispersivas con valores del kh inferiores al límite de condición de aguas profundas igual a π. Se ilustra la eficiencia numérica del código por medio de un análisis de tiempo de

cómputo para unas combinaciones dadas del orden y de la resolución de malla. El modelo de una capa es aplicado luego a la modelación de marea de tormenta forzada por medio del término fuente de gradiente de presión, y muestra una respuesta dispersiva interesante. Por último, se presenta el caso de un soliton peraltándose sobre una pendiente constante. Se considerarán casos adicionales de validación para un sistema de varias capas en unas futuras líneas de investigación.

Résumé

Le sujet de cette étude est étroitement relié à la modélisation de la propagation des ondes marines et naît d'un certain manque d'information scientifique pour les preneurs de décision, quand il s'agit de faire face à la menace d'évènements extrêmes comme les ondes de tempête ou encore les tsunamis sur les côtes Mexicaines. D'ailleurs, ces phénomènes maritimes sont plutôt récurrents au Mexique, avec une forte capacité à ôter des vies humaines et à provoquer de sérieux dégâts côtiers socio-économiques en plus des inondations à l'intérieur des terres. Concrètement, ce travail vise de ce fait à implémenter un outil numérique académique pour la simulation d'ondes longues. Après une révision des caractéristiques et des conditions de validité des théories d'onde analytiques et des techniques de modélisation mathématiques, on concentre l'attention sur les modèles de type Boussinesq. En prolongeant la validité en eau peu profonde à au moins des conditions d'eau intermédiaires, ces modèles présentent le champ d'application le plus étendu en ce qui concerne la propagation des ondes marines, permettant ainsi une reproduction fiable d'une bonne gamme de longueurs d'ondes, allant des ondes longues jusqu'à des ondes relativement courtes. On propose du coup de développer un modèle de type Boussinesq d'ordre élevé en deux dimensions horizontales, basé sur un système d'équations complètement non linéaires et dispersives à l'ordre un, avec une description multi-couche de la distribution verticale du flux. A l'ordre de l'approximation, le modèle inclut les termes de vorticité verticale dans l'équation de conservation de quantité de mouvement. On présente ensuite une estimation de l'erreur de troncature du modèle mathématique, en fonction du nombre de couches. Par ailleurs, on décrit une méthodologie pour optimiser les propriétés linéaires et non linéaires intrinsèques du modèle, à partir d'un choix adéquat des positions des couches ainsi que de leurs respectives variables internes de vitesse. Pour mener à bien la discrétisation numérique du modèle en une dimension horizontale, on s'intéresse à la méthode de Galerkin discontinue. En particulier, le schéma est basé sur une méthode locale de Galerkin discontinue pour la discrétisation spatiale, alors que pour la discrétisation temporelle on utilise un algorithme de Runge-Kutta à variation totale décroissante d'ordre élevé. Les flux numériques sont choisis de façon à assurer la stabilité du schéma. Finalement, on valide le solveur numérique dans le cas d'une couche, par la simulation de deux cas tests classiques de référence. On considère d'abord la propagation de trois ondes solitaires de non linéarité différente sur un fond plat. La présence d'un train dispersif d'ondes courtes est détectée derrière les solitons non linéaires et confirmée par un modèle RANS. En second lieu, on reproduit deux scénarios de dispersion d'ondes au dessus d'une barre immergée. L'impact de l'ordre de précision sur la solution calculée est alors examiné. Le modèle à une couche montre un bon comportement pour des ondes faiblement dispersives dont les valeurs du kh ne dépassent pas la limite de condition d'eau profonde égale à π. On illustre l'efficacité

numérique du code grâce à une analyse de temps de calcul pour des combinaisons données de l'ordre et de la résolution de maillage. Le modèle à une couche est par la suite appliqué à la modélisation d'onde de tempête forcée par le biais du terme source de gradient de pression, et montre une réponse dispersive intéressante. Un dernier test présente enfin la levée d'un soliton sur une pente constante. Des cas test additionnels de validation pour un système à plusieurs couches seront considérés dans le cadre des prochaines lignes de recherche de ce travail.

Abstract

The main topic of this investigation is related to water wave propagation modelling and emerges from some lack of scientific information for decision-makers, when facing the real threat of extreme events like storm surges or tsunamis on Mexican coasts. Actually, such maritime phenomena are quite recurrent in Mexico and still able to take human lives and cause serious socio-economic coastal damage and inland flooding. More specifically, this work aims at the implementation of an academic numerical tool for the simulation of long waves. After revising the characteristics and conditions of validity of analytical wave theories and mathematical modelling techniques, the attention is directed to Boussinesq type models. These dispersive models present the largest field of action as for the propagation of water waves, by extending the shallow water validity to at least intermediate water conditions, then allowing a reliable reproduction of long to relatively short waves. A high order Boussinesq type model is thus proposed and developed in two horizontal dimensions, which is based on a set of fully nonlinear and first order dispersive equations and a multi-layer description of the vertical distribution of the flow. Vertical vorticity terms are retained into the momentum equation up to the order of the approximation. An estimation of the truncation error of the mathematical model is then presented, according to the number of layers. A methodology is also described to get the intrinsic linear and nonlinear properties of the model optimised by choosing adequately the position of layers and the respective velocity variables inside. The numerical discretisation of the model is further carried out in one horizontal dimension using a discontinuous Galerkin framework. In particular, the basis of the scheme is established through a local discontinuous Galerkin (LDG) method for the spatial discretisation, while for the time discretisation a high order total variation diminishing Runge-Kutta algorithm is utilised. Numerical fluxes are designed to ensure the stability of the scheme. Finally, the numerical solver is validated for one layer by means of the simulation of two classic benchmark test cases. Firstly, the propagation over a flat bed of three solitary waves with different nonlinearity is considered. The presence of a dispersive tail of short waves is detected behind nonlinear solitons and confirmed by a RANS model. Secondly, two wave dispersion scenarios over a submerged bar are reproduced. Moreover, the impact of different orders of accuracy is assessed on the computed solution. The one-layer model shows good behaviour for weakly dispersive waves up to kh values close to the deep water limit π. The numerical efficiency of the code is then illustrated by a CPU-time analysis for given combinations of the order and mesh resolution. The one-layer model is further applied to storm surge modelling through a pressure source term forcing and show an interesting dispersive response. Lastly, the shoaling of a soliton over a constant slope is presented. Additional test cases with a multi-layer system will be considered in future work.

Contents

List of Figures

Chapter 1

Introduction

Nowadays, even with a heightened global awareness of extreme maritime phenomena, the occurrence of natural disasters with severe coastal damage and/or large loss of human life still becomes increasingly frequent. Amongst the most devastating events, recently we remember the Indian Ocean tsunami (December 2004) and hurricane Katrina in New Orleans (August 2005), whose numbers speak for themselves. Caused by a tectonic subduction of the India plate under the Burma plate, the Sumatra-Andaman earthquake, of magnitude M_{w} 9.2 on the moment magnitude scale, triggered tsunamis inundating the coasts of most landmasses bordering the Indian Ocean with waves up to 30 m high, and killed over 230,000 people in Indonesia, Malaysia, Thailand, Myanmar, Bangladesh, India, Sri Lanka, the Maldives, Somalia, Kenya, Tanzania, the Seychelles, Madagascar and South Africa. Eventually, nations all over the world donated more than $14 billion in humanitarian aid to attend to stricken regions (Jayasuriya and McCawley, 2010). During hurricane Katrina, Louisiana reported average winds of 140 km/h with gusts of 183 km/h; torrential rain of 203 to 305 mm fell along the track inland from the northern Gulf coast, and storm surge flooding of 7.6 to 8.5 m and 3 to 6 m above normal tide level occurred along portions of the Mississippi coast and the southeastern Louisiana coast respectively (NHC, NOAA). In brief, with catastrophic damage estimated at $75 billion and approximately 1200 reported deaths, Katrina is the costliest and one of the deadliest U.S. hurricanes on record. Now, while the number of casualties after such tragedies may be seen to be in decrease, thanks to the simple education of people and better anticipation, based on past experience, the material damage can still be enormous, as in October 2012 when hurricane Sandy paralysed New York City.

1.1 Current issues in coastal engineering

Concern and social pressure increase ever more for civil protection departments to improve the capacity to react quickly, by making decisions, activating and coordinating emergency procedures, and alerting local populations at an opportune time about safety precautions to incoming tsunami waves or the approach of a tropical cyclone with an induced storm surge in a high wind sea. That is where the scientific community can intercede by bringing some solid knowledge about geofluid dynamics and the propagation and transformation of waves from deep to shallow waters. Strongly based on physics and mathematics, the development

of small and finite amplitude wave theories for sea surface gravity waves and the growth field of unsteady numerical simulations appear to provide valuable help in the understanding of oceanic processes involved in a relatively easy and cheap way, since in general they save us from any scaled experimental test. That kind of information with risk assesments of regions liable to flood, commonly based on analyses of both the vulnerability and hazard (Escudero C. *et al.*, 2012), are fundamental for the establishment of coastal and port management plans to order the design, construction and maintenance of some protection infrastructure, and for the implementation of strategies for the evacuation of people. Moreover, by applying a flooding model on local topographies, it is possible to identify the way the water flows inland, and to design evacuation circuits with systems of by-channels to redirect this flow seaward, in order to protect neighboring urban zones and their inhabitants.

In the following subsections, a brief review is presented of the Mexican situation in view of natural maritime hazards, the categorisation of existing water wave theories according to their domain of applicability and the weight of numerical simulation in coastal engineering.

1.1.1 Mexico: exposure to extreme events and challenges

With more than 11000 km of coastline identified in total and a national waters area covering about 2.5% of the territory, the availability of maritime resources in Mexico is indisputable. However, the efficiency of the exploitation is not optimal and suffers from a certain lack of environmental sustainability. Apart from some shortage of educational, technological and economic opportunities for local coastal communities to profit from this inexhaustible natural resource, people also live with the permanent threat of geologically associated and hydrometeorological phenomena such as tsunamis and hurricane induced storm surges.

Tsunami hazards

Japanese harbour waves or tsunamis, are oceanic long waves generated by sudden movements of the seabed, causing quasi-instantaneous vertical displacements of a substantial mass of water, which are finally restored as high energy waves by gravity. The generation of tsunamis is commonly ascribed to earthquakes, submarine landslides, volcanic activity and much rarer but statistically possible meteorite impact. Invisible in deep waters, the amplitude of a tsunami grows due to shoaling until it looks like a huge bore when viewed from the beach, able to demolish and sweep everything away over quite long distances inland.

Most of the tsunamis reported in Mexico were observed on the Pacific coast (Figure 1.1) and were of seismic origin. This is not surprising given the location of the country, firstly along the San Andres transform fault between the Pacific and North America tectonic plates and secondly on one of Earth's subduction zones, where the ocean floor of the Cocos plate is forcing its way down beneath the continental edge of the North American plate along the Mesoamerican trench. Notwithstanding, Mexico is also exposed to distant tsunamis, as shown by historic records of waves issued from coseismic moves with epicentres in Japan (March 2011), Russia, Alaska, Chile (February 2010).

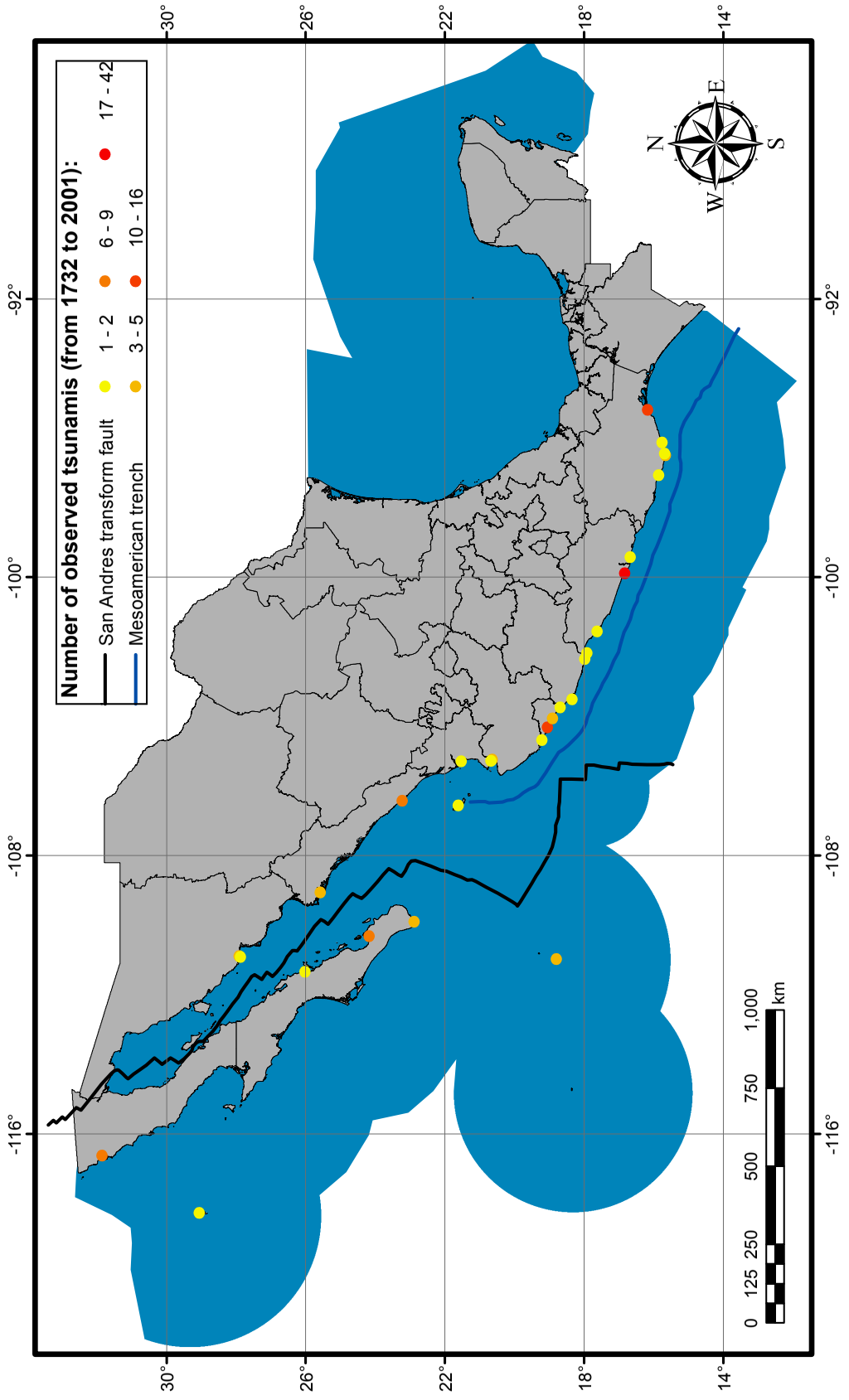

Figure 1.1: Impact of tsunamis on Mexican coasts (geographical coordinates)

To date, there is no detailed free access national database for the impact of tsunamis on Mexican territory. Despite the real will of the government to generate such information in order to encourage related academic research, it is still necessary to use for instance the available data of the U.S. National Oceanic and Atmospheric Administration (NOAA). Regarding tsunami prevention, recording tide-gauges set up along Pacific coast are of little use since information cannot be checked in time because their location is too close to the shoreline. For future protection, the challenge for Mexico would be to modernise these stations to satellite telemetry, to get real time processing of the information so that an alert can be emitted about the danger. In such a case, conventional safety rules consist in moving away from the sea or retreating upland. The case of distant tsunamis is easier to anticipate thanks to the Pacific Tsunami Warning Center operated by NOAA.

Hurricane storm surge hazards

Tropical cyclones are usually classified depending on the growing intensity of sustained winds: we count the tropical depression, the tropical storm and five levels of hurricane on the Saffir-Simpson Hurricane Wind Scale, for maximal velocities above 119 km/h (NHC, NOAA). In the western North Pacific Ocean, hurricanes are called typhoons, while similar storms in the Indian Ocean and South Pacific Ocean are called cyclones. Due to its location on the Tropic of Cancer, Mexico is affected every year in the hurricane season (approximately from May 15 to November 30) from both Pacific and Atlantic fronts (Figure 1.2). According to the National Disaster Prevention Center (CENAPRED for its abbreviation in Spanish), 17% of the annual average of 23 tropical cyclones strike or arrive at less than 100km from the coast, of which 14 occur in Pacific Ocean and 9 in the Gulf of Mexico and the Caribbean. Lately, two memorable tragedies left their mark on Mexican people's minds: hurricanes Gilbert (September 1988) and Wilma (October 2005). Gilbert crossed Yucatan peninsula as a category 5 hurricane before making its final landfall in Tamaulipas: economic losses were estimated at about $766 million with more than 250 deaths. By comparison, the slow-moving hurricane Wilma struck Cozumel island and the Yucatan peninsula at level 4 intensity, before emerging over the Gulf of Mexico 2 days later toward Florida. Silva *et al.* (2009) reported huge waves of 12 m, devastating winds of 250 km/h and storm surge flooding, with consequent tourist infrastructure damage, shortage of drinking water supplies and power cuts (CFE, 2012). A heavy economic toll valued at about $7500 million and 8 deaths, in addition to a quasi-total erosion of the Cancun beach system, with more than 7 million cubic meters of sand removed from the shoreline by powerful currents of 2 m/s, leaving 68% of the beach front as bedrock (Silva C. *et al.*, 2012) were the consequences.

Regarding hurricane associated hazards, strong winds with gusts of over 300 km/h, heavy rainfall, large wind waves, storm surge flooding and landslides can be mentioned. Along the coast, storm surge is often the greatest threat to life and property. Caused by an abnormal creeping rise of water driven by the low pressure weather system, storm surge is produced by this water being pushed toward the shore. Basically, rotating whipping winds and the low pressure act over the ocean surface, causing the water to pile up higher than the ordinary astronomical tide level. Nevertheless, the impact on surge of the low pressure associated with the storm is minimal in comparison to the effect of the wind. Furthermore, the destructive

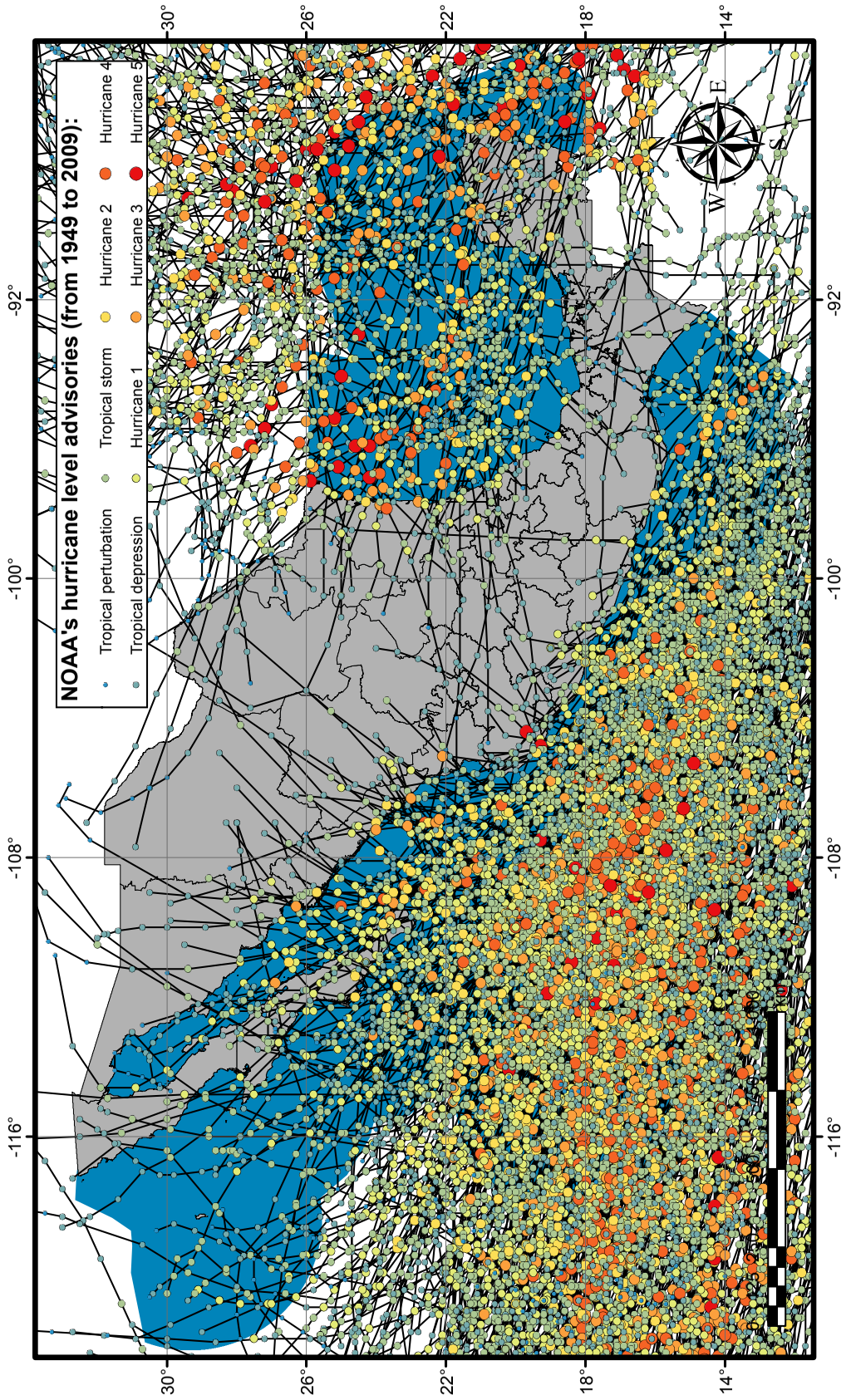

Figure 1.2: Impact of hurricanes in Mexico (geographical coordinates)

power of the surge is strengthened by battering waves, since the propagation inland of these waves is made possible by the surge itself. As described on the website of NHC from NOAA, storm surges are very complex phenomena because of a high sensitivity to factors like storm size and intensity, forward speed, angle of approach to the coast, central pressure and steepness of the continental shelf. Another major and influential factor for the severity of local damage, is the time elapsed by the hurricane over land (Wilma). Archived information about tropical cyclones recorded in the Atlantic, Pacific and Indian Oceans can be consulted on the hurricane webpage of Unisys Weather.

Without doubt, tropical cylones are the most recurring natural threat of hydrometeorological origin in Mexico, ahead of tsunamis. That is why the government started investing money in 2000 for the creation of an early warning system (Sistema de Alerta Temprana para Ciclones Tropicales or SIAT CT in Spanish), whose primary goal was to improve the coordination of initial responses to people's needs such as life and health protection, food and water supply and temporary lodging, in order to prevent and mitigate such events. Initially structured in four alert levels, it is concerned with the interaction between the main actors of the National Civil Protection System (SINAPROC for its abbreviation in Spanish), including the coastal populations, related institutes of scientific and social research and the media. Opportune, formal warnings launch a series of systematised activities for each integral part of the system, according to the intensity, the trajectory and the position of the cyclone. Having shown its efficiency during the confrontation of powerful hurricanes Isidore and Kenna in 2002, SIAT was reviewed and updated in 2003 to standardise the alert procedures of all SINAPROC members for a faster organised response and a truly effective coordination.

Last but not least, a realization of the repercussions of anthropogenic changes and climate changes on the vulnerability of both the expanding coastal conglomerations and beaches is vital. Mexico should impose a stricter, informed control on coastal construction and curb the blind overexploitation of tourist destinations such as those of Quintana Roo. The case of Cancun remains dramatic since hurricane Wilma, with a manmade increase of the rigidity of the Nichupte lagoon system to the detriment of its resilience to storm events (Silva C. *et al.*, 2012). As a result, there is now a lower capacity for breaching renewal for the lagoon water and a severe accrued loss of beach (Ruiz Martínez, 2009).

1.1.2 Inadequacy of water wave theories

A wave is completely specified by its height H, its period T or length L, and the local water depth h. Using these characteristics, some dimensionless parameters can be defined, namely the relative depth h/L, the wave steepness H/L and the wave height to water depth ratio H/h. The raison d'être of wave theories arises from the need to quantify wave characteristics from these basic quantities, for the determination of design waves for a specific site and type of coastal work; we mean here the water surface profile, the forward speed or celerity of the wave form, water particle velocities, accelerations and motion paths, the dynamic pressure field of the wave, potential and kinetic components of energy fluxes, etc... Wave theories are based on the governing assumptions of the homogeneity and incompressibility of the seawater and a horizontal, impermeable and stationary bottom. In addition, during the

propagation of most surface ocean waves, surface tension capillary forces may be neglected and rotation viscous forces only become important in the thin boundary layers present at the bottom and at the air-water interface, leaving gravity, inertia and pressure gradients as the dominant restoring forces. Water wave theories were thus developed using the inviscid velocity potential under the assumption of an irrotational flow.

Finite amplitude wave theories are generally of two types. Numerical theories employ complex variables and Fourier series for the solution of potential flow equations with numerical iterative techniques to optimise coefficients, while analytical theories expand the velocity potential as a power series within a perturbation approach. Evidently, both lead to infinite series solutions of the wave boundary problem, truncated at the desired order. The main drawback of the former remains the limitation to a set of broadly tabulated numbers, as a function of selected values of the basic wave parameters (see the stream function theory of Dean, 1965, 1974). On the other hand, the latter yields explicit expressions for wave characteristics, but at the price of a restriction to a range of relative water depths h/L and some deficiency for large wave steepnesses near breaking conditions, even when carried to high orders.

Analytical theories

Since there is no general solution to the system composed of the Laplace equation and the three gravity wave boundary conditions, all wave theories issue from some form of approximation. For the small amplitude wave theory of Airy (1845), also known as the linear theory of Airy, both parameters H/h and H/L are assumed to be small compared to unity, so that kinematic and dynamic surface boundary conditions can be linearised and applied at the still water level rather than at the free surface. This first order theory, based on a sinusoidal description of waves, can consequently be applied throughout the range of relative water depths h/L, provided $H/h \ll 1$ in shallow water or $H/L \ll 1$ in deep water. Unlike the linear theory, nonlinear or finite amplitude wave theories relax the requirement that either H/h or H/L be small, then taking the other ratio as the small perturbation parameter, in order to derive valid theories for finite amplitude waves over some specific range of wave conditions. A finite H/L results in a theory useful in deep water (e.g. the theory of Stokes, 1847) whereas a finite H/h results in a theory more appropriate for shallow water (e.g. the cnoidal theory based on work done by Korteweg and de Vries (1895) and further synthesised in Wiegel (1960, 1964)). While Stokes' theory uses a simple series of trigonometric functions, the cnoidal theory involves Jacobian elliptical functions hardly applicable in practice. Both wave forms are characterised by sharper and larger amplitude crests in return for flatter and smaller amplitude troughs, a situation all the more accentuated in the case of the cnoidal wave. For shallower waters, a first order solitary wave theory, with a surface displacement completely above the still water line and useful for tsunamis, was firstly presented by Boussinesq (1872) and later attempts to develop it to higher orders were made (e.g. McCowan (1891), Laitone (1960), etc...). With a crest and no trough, it is of infinite wave period and length. As for some interesting features, the truncation at first order of the nonlinear Stokes' expansion leads to the linear small amplitude wave theory of Airy, and deep and shallow water limits of the first order cnoidal wave are respectively the wave of Airy and the solitary wave of Boussinesq.

For a mathematical description and corresponding literature of all these theories, readers are referred to Dean and Dalrymple (1991) and Sorensen (1993). For the circumstances under which analytical small and finite amplitude wave theories can be applied, Figure 1.3, taken from Hedges (1995) and supported by both theory and reference to laboratory measurements, provides useful guidance. In relatively shallow water, the Ursell number HL^2/h^3 mainly governs the suitability of theories to describe wave conditions, while in deep water, it is the wave steepness H/L. It may be noted that the range of validity of linear theory is reassuringly wide, covering all of the transitional water depths for most wave steepnesses encountered in practice (Reeve *et al.*, 2004). In spite of its limitations, this theory, extensively used in practice, has been shown to yield surprisingly realistic results for conditions that markedly deviate from the small amplitude assumption.

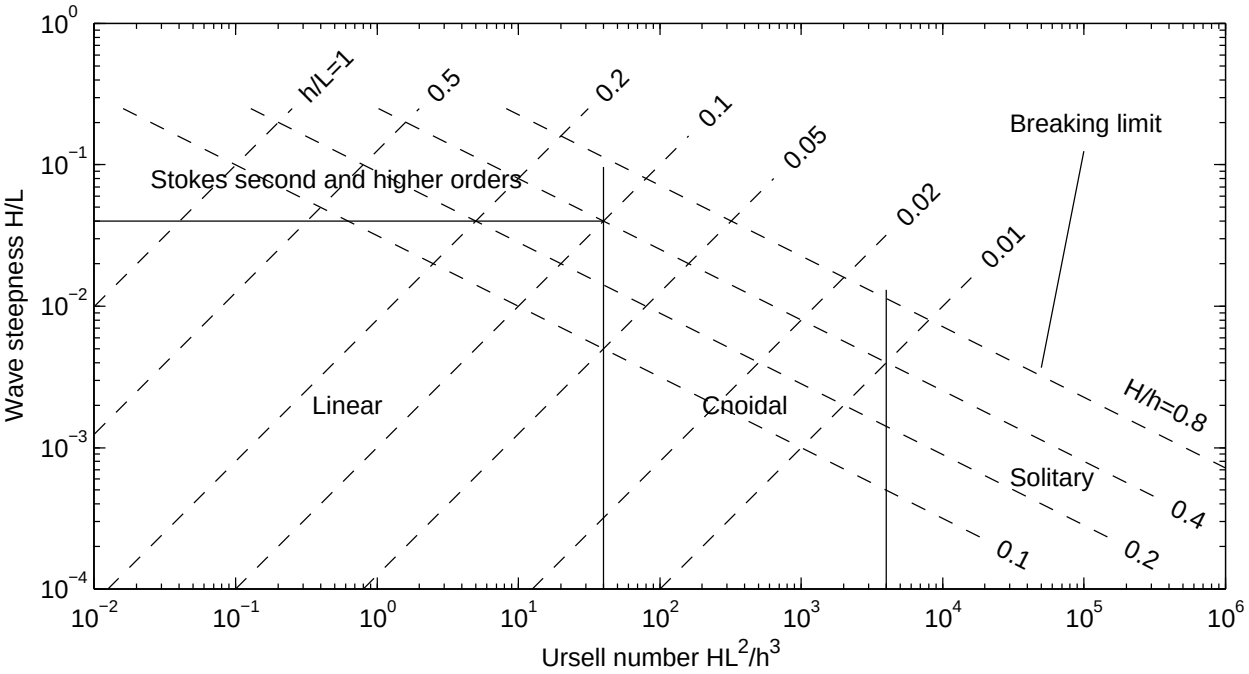

Figure 1.3: Approximate regions of validity of analytical wave theories

Main limitations

Describing the properties of monochromatic wave trains, with the same height and length from wave to wave, these theories are valid for regular gravity waves but are inappropriate for much more complex and irregular wind generated wave surface profiles, where statistical distribution type analyses are required. Moreover, wave theories are limited to constant depth and unidirectional wave propagation conditions, where shoaling, breaking, runup and three-dimensional wave transformations like refraction and diffraction cannot occur. Besides, wave theories do not pretend to reproduce them. Then, in order to be able to investigate wave propagation events over two-dimensional real bathymetries, variable depth numerical modelling appears to be the most attractive alternative for ocean and coastal engineers.

1.1.3 Advances in numerical simulation

Today, the use of water wave simulation tools is essential in coastal engineering. Despite the fact that the range of existing numerical models seems wide enough, it is important to continue the improvement of both their accuracy and efficiency. On the one hand, calculation domains can cover quite big areas for large scale simulations, in the order of thousands of miles. Usually in those cases, the need for high order discretisation schemes is acknowledged to allow the use of coarse grids, since from a computational point of view and assuming the consistency of the schemes, the consideration of extremely refined meshes to reach the desired accuracy, with consequent low temporal increments to ensure the numerical stability, is not an acceptable option. On the other hand, a better numerical efficiency, with maybe a parallel coding, allows us to get closer to a quasi-ideal real time simulation. Indeed, at the time of the generation of a tsunami, wave model predictions such as the number and height of waves, as well as the time to reach the shoreline, will be timely only if the code runs faster than the physical time. This situation is typically referred to as the ideal simulation.

In any case, before being made available to users, a numerical model requires serious attention and commitment for a proper validation and a suitable calibration when necessary. The validation has to be done by comparing computed results with known analytical and other numerical solutions, and experimental or field data, within the realms of possibility. Wave theories are derived to be used for that purpose. Once validated, the model can be applied to simulate plausible scenarios or real events. It is clear that numerical simulation has a lot of future in all domains, provided people always keep control of the models and never forget the meaning of an approximation; a critical eye on results while taking account of randomness and margins of error is indispensable.

Regarding mathematical modelling options, the most complete set of equations to govern the physics of any hydraulic problem is the standard three-dimensional compressible system of Navier-Stokes equations. However, the heavy computational requirements of these equations make them unsuitable for the simulation of ocean waves, especially as the compressibility of the seawater and the viscosity of the flow can be ignored to the magnitude of scales in play (from meso to macroscales). In that sense, the implementation of a model able to propagate all wave lengths and reproduce all wave transformation processes at all spatiotemporal scales, still appears numerically inconceivable in ocean modelling. So that means scales have to be separated and hypotheses made, so the complexity of the system can be reduced to a problem solvable in reasonable times with currently available microprocessors. Water wave propagation models are generally classified by the form of solution delivered: firstly the phase-resolving models yielding harmonic solutions (by the use of complex numbers) and an implicit propagation of waves, and secondly the non phase-resolving models providing transient solutions with an explicit propagation in time of waves. Corresponding advances under both linear and nonlinear approaches are reviewed in the next two paragraphs.

Linear models

The first linear numerical attempts to model the inshore transformation of deep water wave spectra used ray theory based on optic and geometric bases such as Snell's law of refraction

(e.g. Abernethy and Gilbert, 1975). Basically, from a discretisation of the offshore wave spectrum in both horizontal direction and frequency and a ray-tracing refraction and shoaling analysis, a spectral description of nearshore wave conditions at a point could be obtained and further improved with an empirical incorporation of nonlinear surf zone processes such as breaking (Bouws *et al.*, 1985). Extended from regular bottoms with parallel isobaths to slightly irregular bathymetries, ray theory is still restricted to small amplitude waves as it relies on the linear theory of Airy (1845). Unfortunately, these semi-graphic approaches do not account for diffraction and reflection, and result in some quite plodding and drawn out manual calculation procedures. Developed more than three decades ago, spectral ray models are now almost obsolete with very limited engineering applications, regardless of their modest computational requirements and proved effectiveness (Reeve *et al.*, 1996).

A significant step in the development of linear models was the introduction of the mild slope equation (MSE), first derived by Berkhoff (1972) and described more concisely by Smith and Sprinks (1975). Resulting from the linearised equation of an irrotational flow in three dimensions, the MSE estimates the transformation of a monochromatic linear wave train over an impermeable seabed under the assumption of a slowly varying depth. The approximated elliptic differential equation can deal with relatively complex wave fields in deep and transitional waters with satisfactory accuracy. Based on the small amplitude wave theory, it does not apply in shallow water for long wave conditions. The MSE includes the implicit resolution of the main wave transformations such as refraction, shoaling, diffraction and reflection (e.g. Mike 21 EMS module (DHI Water and Environment, 2007a) of the Danish Hydraulic Institute). However, a somewhat arduous treatment of boundary conditions and the high requirements needed in both computational efforts and resources (a minimum of grid nodes per wavelength is recommended for finite difference schemes) make it hardly applicable to large coastal areas. Some more computationally efficient and stable procedures were developed by Li and Anastasiou (1992) and Li (1994), but still remain expensive. We may mention the extension of elliptic models to irregular waves by Al-Mashouk *et al.* (1992) and Li *et al.* (1993), with a methodology consisting in the linear superposition of a series of computations for individual direction/frequency pairs of a wave spectrum.

Some work that neglects some of the processes was done in order to simplify the MSE and enable computationally efficient algorithms. Copeland (1985) transformed the equation into a hyperbolic form, but achieving numerical convergence was shown to be difficult within this approach. Another common simplification is the parabolic approximation of the MSE, giving rise to the refraction-diffraction models (e.g. Mike 21 PMS module (DHI Water and Environment, 2007b) of the Danish Hydraulic Institute, the REF/DIF model (Kirby *et al.*, 2002) of the University of Delaware and the OLUCA model (GIOC, 1999, 2000) of the University of Cantabria). These models are able to reproduce refraction and shoaling, but disregard reflection and assume that diffraction effects are weak in the direction of wave propagation, through an expansion in the Padé series. Only small angular deviations from the initial direction of propagation are allowed then, a constraint further relaxed after some improvements on the approximation by McDaniel (1975), Kirby (1986b) and Dalrymple and Kirby (1988). Parabolic models are the most widely used for practical engineering purposes, thanks to more efficient numerical implementations. They deliver good approximations when

diffraction is weak, that is to say for small irregularities of the bottom or non parallel depth contours, but present some serious drawbacks when diffraction becomes important in the presence of islands or structures. Of course, without reflection, they are useless for resonance studies.

Additional simplifications of parabolic approximations can be derived, yielding the remaining basic refraction and diffraction models. Indeed, if diffraction terms are completely removed from previous refraction-diffraction equations, models that only take into consideration refraction and shoaling are obtained. Correspondingly named refraction models, they appear as an easier and much less tedious alternative to ray theory, with less rectriction on the irregularity of the seafloor (e.g. REFRACT model (Dalrymple, 1991) of the University of Delaware). Now, if those equations are reduced to horizontal bottom conditions, they form the diffraction models which eliminate all bathymetric variation effects, then only treating vertical impermeable structure induced diffraction problems. An interesting feature of the latter is that explicit analytical solutions can be encountered to get the diffraction coefficient, even though sometimes the presentation of results on dimensionless diagrams, as in the Shore Protection Manual (1984), looks more appropriate due to the use of Bessel numbers in systems of cylindrical coordinates. For real practical cases, both refraction and diffraction models can be utilised to study refraction with shoaling and diffraction separately, before combining results to try to get a coupling of both analyses.

To get back to the MSE, originally derived for impermeable bottoms and valid for bed slopes up to 1:3 (Booij, 1983), several studies have been carried out from its basic version to try to eliminate these restrictions. By expanding bottom boundary conditions to a slowly varying mean water level, Kirby (1986a) presented an extended version of the mild slope equation (EMSE), and Massel (1993) proposed a new approximation including the effect of evanescent modes. A little later, Chamberlain and Porter (1995) derived the modified mild slope equation (MMSE) with the inclusion of second order bathymetric terms, thus removing the mild slope limitation, while Porter and Staziker (1995) extended it to evanescent modes with new boundary conditions. In order to reproduce energy losses from breaking and bottom friction, dissipation terms were incorporated in the MMSE by Dingemans (1997a) in a similar way to Kirby and Dalrymple (1994). Based on the homogeneous and isotropic media theory of Sollitt and Cross (1972) to let Darcy's law be applicable, the first consideration of porous structures within the mild slope approximation was proposed by Rojanakamthorn *et al.* (1989, 1990), for breaking and non breaking waves travelling over an arbitrary finite porous layer. Silva *et al.* (2002) then proposed a derivation of the MMSE capable of describing known scaterring properties of porous ripple beds, based on the previous work of Mase and Takeba (1994) and studies of the kinematics and dynamics of wave interaction with permeable breakwaters by Losada *et al.* (1996). The new equation was finally extended to evanescent modes in Silva *et al.* (2003). Applications to wave-porous struture interaction, from regular to random unidirectional and multidirectional waves through the use of a transfer function, are presented by Silva *et al.* (2006a, 2006b). In general, in the face of its computational disadvantages, the MMSE is widely used to date to predict linear wave patterns in harbours and coastal regions with complex geometries (e.g. WAPO model (Silva Casarín, 2008) of the National Autonomous University of Mexico by Silva *et al.* (2005)). Finally, recent related

publications look at the derivation of analytical solutions under specific bed profiles (e.g. Xie and Liu, 2012), as helpful data for the validation of mild slope type models.

Among linear wave propagation models, the MMSE is certainly the most complete and robust physical equation for steady harmonic solutions. Nonetheless, linear models suffer from their restriction of validity to deep water sine waves because of the first order approximation. They are clearly useless for the reproduction of the nonlinear asymmetrical steepness of shoaling waves in shallow water. At this point, concerned with the simulation of long waves that typically dominate coastal wave fields, as well as intermediate and moderately short waves that emerge from locally involved nonlinearities close to the breaking point in the internal surf zone, let us take an interest in nonlinear modelling, for a more realistic shallow water hydrodynamics.

Nonlinear models

Often depth-integrated equations have been pointed out as the way forward for the modelling of unsteady nonlinear wave interactions in shallow water, therefore making them a promising option for the study of wave propagation in coastal regions. This family of equations is comprised of the well known shallow water equations (SWE), firstly introduced into a one-dimensional version for nonsteady flow in open flat bed channels by Barré de Saint-Venant (1871), and Boussinesq type equations, derived from the classical Boussinesq equations of Peregrine (1967). Resulting from the integration over the entire water column of the wave motion equations, depth-integrated equations can be encountered under different levels of nonlinearity, where weakly and fully nonlinear forms are generally achieved. By some projection of primitive governing equations onto the (x, y) horizontal plane, both are based on a polynomial approximation for the vertical flow distribution so that the initial three-dimensional problem is reduced to a two-dimensional one. These models are formulated accordingly in terms of the free surface displacement and representative horizontal flow components, which can be either depth-averaged (shallow water models) or evaluated at a certain elevation $z = \kappa(x, y, t)$ (Boussinesq type models). In the first set of equations, vertical velocities of fluid particles are neglected while a constant polynomial is utilised for the vertical profile of horizontal components: the model is depth-averaged. Here the validity of solution for these equations is limited to the longest waves, like tides, storm surges or tsunamis, for which any depth is shallow. In contrast, for Boussinesq type equations the vertical profile of velocities is approximated by at least first and second degree polynomials for vertical and horizontal components respectively, which enables better accuracy for deeper water conditions. Through this, the mathematical description is able to simulate shorter waves in large coastal areas, like storm waves that naturally move at the free surface of storm surges under the effect of hurricanes, for instance. Models based on these mathematical functions are usually characterised by a range of validity expressed in terms of maximal achievable kh values, where $k = \frac{2\pi}{L}$ is the wavenumber and h is still the local water depth.

Shallow water models are quite useful to simulate bay and estuarine hydrodynamic responses to river discharges and tidal forcing (e.g. H2D model of the University of Cantabria by Castanedo Bárcena (2000)) as well as the generation of storm surges (e.g. MATO model of the

National Autonomous University of Mexico by Posada V. *et al.* (2010)). They are also largely used for the propagation of tsunami waves over relatively smooth bathymetries (e.g. GeoClaw module from the Clawpack software package by LeVeque *et al.* (2011), a powerful large scale simulation tool based on a very efficient dynamic Adaptive Mesh Refinement (AMR) procedure). However, for an additional approximated reproduction of storm wind generated waves that accompany those surges, or for the simulation of tsunamis over more complex seabed topographies, for example with the presence of high depth gradients able to produce non negligible wave dispersion, the choice of Boussinesq models can be recommended for more realistic wave surface profiles and run-up estimations (e.g. Mike 21 BW module (DHI Water and Environment, 2007c) of the Danish Hydraulic Institute, FUNWAVE-Geowave model (Kirby *et al.*, 1998) of the University of Delaware by Wei *et al.* (1995), and COULWAVE model (Lynett and Liu, 2002) of Cornell University by Lynett (2002)). In addition to the Coriolis acceleration, both types of equations can incorporate turbulent efforts, as well as some empirical forcing and dissipation source terms for capillarity effects and the wind and bed shear stresses. Notwithstanding, whereas such terms are commonly added in an ad hoc manner to the inviscid equations, Kim *et al.* (2009) demonstrated that it is not necessary to do so and these terms can be included through a physically consistent derivation from the viscous primitive equations. Besides, it is clear from their work that one cannot properly add the quadratic bottom friction term without also adding a number of extra terms in the integrated governing equations. As a rule, while numerically harder to implement than shallow water equations, Boussinesq type models are capable of reproducing the combined effects of most wave phenomena of interest in coastal and harbour engineering, with an extension of the domain of applicability from shallow to at least transitional waters. Particularly robust for the transformation of surface gravity waves by coastal structures and in the vicinity of the breaking zone, they represent a good base to model breaking dissipative effects, run-up and run-down processes, sediment transport, etc...

1.2 Boussinesq type modelling

One of the main assets of Boussinesq type equations over shallow water equations is the approximation of the wave dispersion physical process, responsible for the separation of sea and swell wave states. The linear theory of surface gravity waves shows by means of the dispersion relation that in deep water, the wave celerity is in inverse proportion to the frequency of the wave component considered. Low frequency waves therefore travel faster than high frequency waves. The initially random wave field, as generated in a storm, then disintegrates when it moves out of the storm in fields of more regular waves, with low frequencies in the lead and high frequencies in the trailing edge: this is the frequency dispersion. Apart from becoming more and more regular, waves also change from short to long crested waves, due to the dispersion of wave frequencies in their respective initial direction of propagation in the storm: this is the direction dispersion. Waves that have thus dispersed across the ocean are called swell (Holthuijsen, 2007). A regular monochromatic wave train can also suffer dispersion and harmonic generation over submerged bars in shallow waters, induced by nonlinear energy transfers that normally occur under bathymetric effects and result in the release of bound (phase-locked) harmonics into shorter free waves.

In this work, we mainly focus on Boussinesq type models, as they are the most dependable option to date to simulate the propagation of extreme nonlinear long waves such as tsunamis or storm surges in coastal waters, thanks to a well founded treatment of dispersion through the addition of mixed and at least third order spatial derivative terms to the leading order shallow water terms. Actually, long wave equations would be recovered by an elimination of dispersive terms from any set of Boussinesq type equations. Two important dimensionless parameters are associated with Boussinesq type equations: the nonlinearity is characterised by the wave amplitude to water depth ratio $\varepsilon = \frac{a}{h}$, and the dispersion is characterised by the water depth to wave length ratio $\mu = \frac{h}{l}$. While ε may be considered as arbitrary, Boussinesq type derivations require the weak dispersion assumption $\mu^2 \ll 1$. In practice, there are many ways to obtain a set of Boussinesq type equations, since derivations can be started from the potential flow or momentum equations, according to the assumed (or not) irrotationality of the flow. They produce dispersive mathematical formulations that can be written in terms of various kinematic variables, whether the velocity potential or the horizontal velocity: specifically the depth-averaged value, the bottom, still water or surface value, or an arbitrary z-elevation respective evaluation can be utilised, and Taylor series expansions are generally applied to switch from one to another. A corresponding exhaustive revision of the state of the art of Boussinesq type modelling background is presented below.

1.2.1 First order dispersive equations

The pioneering work by Boussinesq (1872), limited to a horizontal bed, allowed frequency dispersion through a non-hydrostatic pressure distribution, altered by a linear variation of the vertical velocity from zero at the bottom to a maximum at the free surface. Extended to uneven bottoms in one dimension by Mei and Le Méhauté (1966), with some minor algebraic corrections on the characteristic form of the equations updated in Madsen and Mei (1969), a set of equations for varying depths in two horizontal dimensions was finally presented by Peregrine (1967). Today referred to as the standard Boussinesq equations and originally given under two different forms including the mean and still water velocities chosen for the dependent variables, the mathematical model of Peregrine (1967) provided the starting point for the development of Boussinesq theory and its use in wave propagation problems. Taken from the conventional dispersive perturbation method, with μ^2 taken as the small expansion parameter, the original assumptions at the same order of weak dispersion and weak nonlinearity with $\varepsilon = O(\mu^2)$ restricted their utilisation to shallow water areas and small nonlinear effects since only first order terms $O(\varepsilon)$ and $O(\mu^2)$ were retained. A few years later and under the same hypothesis, Dingemans (1973) presented an investigation aimed at the introduction of second order dispersive terms $O(\varepsilon\mu^2)$ and $O(\mu^4)$ into Boussinesq equations; however, he provided neither accuracy analyses nor computations.

Later efforts aimed to extend the range of applicability of Boussinesq equations by improving their linear dispersion characteristics within the first order dispersive approximation, notably by the introduction of Padé approximants for the exact theoretical dispersion relationship of Airy (1845). Amongst other related publications, where various forms of the standard Boussinesq equations are studied, the book of Whitham (1974) and papers of Svendsen (1974)

and Mei (1983) illustrate the sensitivity of the accuracy of linear dispersion properties to the choice of the velocity variable and to the mixture of spatial and temporal derivatives in the governing equations, for increasing wavenumbers. In the case of a constant depth in a single horizontal dimension, Witting (1984) inspired Boussinesq model developers by modifying the straightforward Taylor expansion of the velocity with the introduction of calibration coefficients for the optimisation of the phase celerity. The newly parameterised linear dispersion relation was matched with a Taylor expansion about $kh = 0$ of Airy's squared celerity up to $(kh)^4$ by a [2/2] Padé expansion in kh. As a result, linear properties were greatly enhanced with a 5% phase error close to the deep water limit $kh = \pi$, against the previous 5% phase error at $kh \approx 0.44\pi$ of the [0/2] Padé expansion corresponding to the best phase properties registered for the Boussinesq equations, and associated with the depth-averaged version recommended by Whitham (1974). Later, and under the same horizontal bottom assumption, Madsen *et al.* (1991) manipulated the dispersive terms into the two-dimensional system of depth-averaged equations solved by Abbott *et al.* (1984), with the introduction of an additional weighted third order derivatives term to the momentum equations; this term was added by invoking the linear long wave equation so that it reduced to zero in shallow water without affecting the accuracy. An alternative form of the Boussinesq equations was therefore presented with some possible improvements in linear dispersion characteristics by considering the free coefficient as a curve fitting parameter in the process of obtaining the best overall agreement with Airy's theory; in that sense, slight deviations from the [2/2] Padé approximant of Witting (1984) were shown to lead for example to phase errors of less than 3% for the range $0 \leqslant kh \leqslant 1.5\pi$. This work was closely extended to mildly sloping bottoms and an ensuing linear shoaling analysis in Madsen and Sørensen (1992). Finally, Nwogu (1993) achieved similar improvements by using a velocity at an arbitrary distance $z = \gamma h\,(x, y)$ from the still water level as the dependent variable for uneven bottoms in two horizontal dimensions. Following the methodology of Madsen *et al.* (1991) with a small sacrifice of low wavenumber accuracy for accuracy at higher wavenumbers, Nwogu proposed an optimum value $\gamma = -0.53$ for the reference elevation that minimises the sum of the relative error of the phase speed over the entire range $0 \leqslant kh \leqslant \pi$ to less than 2%.

Furthermore, the weak nonlinearity limitation might be eliminated by dropping ε as a scaling parameter in the derivation of the dispersive approximation. In fact, Serre (1953) had been the first to try combining the lowest order dispersion with full nonlinearity, using a z-independent horizontal velocity. Nevertheless, the assumption of such a uniform vertical distribution for this velocity was shown to prevent his approximation from any significant improvements on frequency dispersion, in comparison to the classical weakly nonlinear forms of Boussinesq equations, hence making the equations of Serre (1953) somewhat unattractive (Dingemans, 1997b). Later, fully nonlinear versions of the two-dimensional first order dispersive Boussinesq equations for variable depths, based on the judicious arbitrary z-level approach of Nwogu (1993), were lately derived by Liu (1994) from the mass conservation and Euler momentum equations, and Wei *et al.* (1995) from the boundary value problem for an inviscid and irrotational wave motion expressed in terms of the velocity potential, with terms $O\left(\varepsilon^n \mu^2\right)$ retained $\forall n \in \mathbb{N}$. A detailed review and discussion about all these Boussinesq type formulations and their applications can be found in Madsen and Schäffer (1999). In order to complete these nonlinearity enhancements, Kennedy *et al.* (2001) generalised the

reference elevation concept of Nwogu (1993) to a time varying component dependent on the free surface elevation: $z = \gamma h(x, y) + \delta\zeta(x, y, t)$, then allowing a considerable optimisation of nonlinear performance for the equations of Wei *et al.* (1995) by an adequate choice of the new free parameter δ. Thereby, from a second order Stokes (1847) type Fourier analysis and by setting the linearity coefficient to the [2/2] Padé approximation of Witting (1984) $\gamma = \sqrt{1/5} - 1 \approx -0.55$, he matched a power series expansion about $kh = 0$ of the second order component of the free surface elevation with the same expansion of the full second order Stokes solution up to $(kh)^4$, with the value $\delta = 17\sqrt{5}/200 \approx 0.19$.

1.2.2 Higher order approximations

Since the work of Dingemans (1973), other authors had been working on solutions to raise the dispersion accuracy in Boussinesq type equations without having to add higher order dispersive terms. Then, Schröter *et al.* (1994) and Schäffer and Madsen (1995) pursued the same methodology by merging the approaches of Nwogu (1993) and Madsen *et al.* (1991), in order to achieve the more accurate [4/4] Padé approximation for the linear dispersion and some new improvements on linear shoaling properties. Acceptable agreements with the linear theory of Airy (1845) were obtained up to $kh \approx 6$, at almost twice the deep water limit. At this point, it seems important to recall that these equations are not developed to a higher order than the classical Boussinesq equations. Thus, the underlying expressions for the vertical distribution of velocities cannot be trusted in the extended depth range in which the surface elevation is still very well described (Schäffer and Madsen, 1995). To mend these shortcomings, higher order Boussinesq type approximations were then investigated. A series of more complex Boussinesq type derivations, introduced from the potential flow equations with second order in dispersion, can be appreciated in Madsen and Schäffer (1998). Through the same dispersion enhancement procedures and accuracy analyses, this time performed with emphasis on linear dispersion, shoaling characteristics and nonlinear properties for large wavenumbers, a comparison is made between several formulations, on the one hand given to different levels of nonlinearity, on the other hand written in terms of the depth-averaged velocity and particle velocities at the still water level or at the arbitrary vertical location. Once again, the superiority of the arbitrary z-elevation form over the depth-averaged form is underlined, even at a lower dispersive order where almost the same linear and nonlinear characteristics can still be achieved. Similar enhancements under a mild slope assumption at $O(\mu^4)$ for linear dispersion accuracy, shoaling properties and nonlinear characteristics, can be found in Zou (1999) within a depth-averaged velocity formulation and Zou (2000) for a more general calibration velocity variable.

Closely, Gobbi *et al.* (2000) derived a fully nonlinear second order Boussinesq type model, by extending the equations of Wei *et al.* (1995) to $O(\mu^4)$ with a fourth order polynomial in z for the velocity potential. As a result, a much better representation of the internal kinematics than $O(\mu^2)$ first order dispersive approximations, especially in the intermediate to deep water range was achieved. This formulation used a new dependent variable as the weighted average of the velocity potential evaluated at two distinct elevations in the water column. The weight and positions were chosen to achieve the [4/4] Padé approximant of the exact linear dispersion relationship of Airy (1845), with a certain flexibility left for the weight value.

Presented for a two-dimensional horizontal bottom in Gobbi *et al.* (2000), the description of the model for variable water depths can be found in Gobbi and Kirby (1999), together with the discretisation scheme and some one-dimensional numerical applications. More recently, Lynett (2002) proposed a multi-layer system for the first order equations of Liu (1994) to get a very high order Boussinesq type equations model, with a series of quadratic polynomials matching at layer interfaces, then allowing the reproduction of even more complex vertical profiles for the internal kinematics. He used the general approach of Kennedy *et al.* (2001) for the vertical location of layer interfaces and horizontal velocity variables, and an optimisation of linear and nonlinear properties was performed by adjusting the arbitrary coefficients through some overall error minimisation processes over given specific kh ranges, with respect to the known analytical properties of water waves. Errors in the wave speed, group velocity and shoaling gradient were included for the linear part, while errors in the second order free surface correction and subharmonic/superharmonic transfer amplitudes for bichromatic wave interactions were taken into account for the nonlinear part. Generally speaking, linear characteristics of a N-layer model are equivalent to a $[2N/2N]$ Padé approximation (Lynett and Liu, 2004b). In the case of the two-layer model, numerically implemented and described in detail in Lynett and Liu (2004a), linear and nonlinear behaviours were shown to be relatively well captured up to $kh \approx 6$. For comparison, a less thorough linear optimisation, undertaken by Lynett (2002), examining only the phase celerity and the group velocity, indicated a very good linear accuracy up to $kh \approx 15$ for the three-layer model and to $kh \approx 22$ for the four-layer model. It is emphasised here that the multi-layer approach enables the model to control and extend its own limit of validity from intermediate to fairly deep water regimes, without the need to raise the order of the dispersive approximation, hence retaining at most third order derivatives and a relatively simple system of equations. Meanwhile, Hsiao *et al.* (2002) derived a Boussinesq type model for waves propagating over a permeable bed, taking the equations of Liu (1994) for the free flow region and a fluid phase volume-averaged momentum equation in terms of the intrinsic velocity and pore pressure for the permeable layer. Optimal positions for the evaluation of velocities in both layers can finally be calculated according to their thickness ratio, through least-square error minimisations for the phase speed and damping rate over a specific kh range.

In general, these high order Boussinesq type models result in a better linear behaviour than the nonlinear one, and Agnon *et al.* (1999) presented a different procedure to achieve the same accuracy in both linear and nonlinear properties within a mild slope approximation. Unlike the traditional way well described in Madsen and Schäffer (1998), the solution of the problem is basically decoupled into two parts: a truncation to a finite order through Padé approximants for the infinite power series solution of the Laplace equation in a time-independent domain for the linear part, and a marching in time using the exact free surface boundary conditions for the nonlinear part. The separation of the approached linearity and exact nonlinearity allows the accuracy of linear dispersion and shoaling to be fully carried over to the nonlinear interaction part of the system. Written from the still water level, the infinite series was further generalised to an expansion from the arbitrary z-level of Nwogu (1993) in Madsen *et al.* (2002, 2003), together with attached optimisations of linear velocity vertical profiles by some error minimisation processes, a comparison between various truncation methods and some one-dimensional numerical tests. For up to fifth-derivative operators

involved in the finite series approximation, model analyses report linear and nonlinear wave characteristics of an accuracy up to $kh \approx 40$, leading to a major improvement over previous Boussinesq type formulations. Finally, these high order Boussinesq type equations were extended to fully nonlinear and highly dispersive water waves interacting with a rapidly varying bathymetry in Madsen *et al.* (2006), with some smoothing procedure for the arbitrary expansion level needed to remove the effects of small scale undulations of the bottom. A full re-derivation of these equations in a more general framework, including both potential and velocity formulations, can be found in Bingham *et al.* (2009), with some corrections and consistency refinements as regards the order of approximation. In parallel, Zou and Fang (2008) proposed, analysed and validated three alternative forms of a second order Boussinesq type model, based on a direct extension of the equations of Serre (1953) to the next higher order. The most complete version, with full nonlinearity up to $O(\mu^4)$, resulted very close in accuracy to the model of Gobbi *et al.* (2000).

1.3 Objectives and novelty of the investigation

With all the above mentioned studies in mind, this work is to be seen in the present context of international lines of research and some need for Mexico to start generating its own academic numerical nonlinear models, to be able to compete with foreign simulation tools.

The main objective of the investigation consists in developing from scratch a high order Boussinesq type model, for the propagation of water waves. The dispersive model has to be able to reproduce wave generation by a moving seabed, and transformation processes such as wave-wave and wave-current interactions, bathymetric refraction and nonlinear shoaling, diffraction and reflection near structures, accurate in relation to local kh values. The matter of viscosity and the associated turbulence will not be treated here within the model, as this dissipation of energy is negligible on large scale simulations, except maybe at the free surface where the wave breaking dissipative mechanism could have significant effects on the flow and would require some specific attention.

To reach such a scope, the multi-layer technique of Lynett and Liu (2004b) is applied to a rotational version of the fully nonlinear equations of Liu (1994). Indeed, it is proposed to allow some vertical vorticity and the formation of horizontal eddies, that generally govern tsunami induced flows in harbour basins (Lynett *et al.*, 2012). Regarding the division into layers of the water column, it is, from a mathematical and numerical point of view, surely the most efficient approach ever proposed for Boussinesq type equations. It enhances the deep water accuracy with shallow water flow based equations, leading to a model able to cover the entire range of possible wave lengths, depending on the number of layers considered. Initially thought to simulate long surface gravity waves such as tsunamis and storm surges, the model will be then satisfactorily applicable to shorter wind waves and those emerging from nonlinear interactions in the nearshore area, where both actually coexist during hurricanes. In addition, the governing equations are intended to be solved with a more sophisticated numerical algorithm than the predictor-corrector finite difference routine implemented in the FUNWAVE code of Wei *et al.* (1995), and reused in the COULWAVE code by Lynett (2002).

The proposed model employs the discontinuous Galerkin (DG) method for the numerical resolution of these equations. In fact, a similar scheme has been recently presented by Engsig-Karup *et al.* (2006), who used a discontinuous Galerkin finite element method (DG-FEM) for the equations of Madsen *et al.* (2002) and obtained encouraging results. Besides, their work has been extended to 2D problems (see Engsig-Karup *et al.*, 2008). Following the observed success in the utilisation of DG-based methods for the discretisation of Boussinesq type equations, this study aims to use the latest developments of the DG method for computational fluid dynamics, in the presence of high order derivatives.

As for some specific objectives, the following methodology is considered:

- Carry out the complete derivation of a multi-layer set of Boussinesq type equations;
- Initiate and validate the numerical implementation in one horizontal dimension;
- Illustrate the accuracy and efficiency of the model through some application test cases.

1.4 Organisation of the thesis

The present document is structured in five main chapters, including the Introduction. The following lines give a brief description of their respective contents:

- Chapter 2 presents the derivation of the Boussinesq type mathematical model, an evaluation of the truncation error due to the dispersive truncation of the equations and a methodology for the calibration of the model to the theory of Stokes (1847).
- Chapter 3 introduces the resolution strategy followed and the numerical scheme implemented for both space and time discretisations in one horizontal dimension.
- Chapter 4 illustrates the results obtained for two validation test cases of the one-layer model: the constant depth propagation of solitary waves and the interaction of regular wave trains with a submerged bar. An application of the code to the simulation of pressure forced storm surges and solitary wave shoaling is then examined.
- Finally, the conclusions derived from the present investigation are given in chapter 5, with some future lines of research for the continuation of the work.

Chapter 2

High order Boussinesq type model

This chapter is essentially dedicated to the detailed mathematical derivation, an accuracy evaluation and some optimisation clues for the intrinsic properties of a two-dimensional fully nonlinear Boussinesq type model. The governing equations result from a first order dispersive expansion of the incompressible Euler system (Liu, 1994) within a multi-layer description of the system (Lynett, 2002), which addresses them the status of high order Boussinesq type approximation amongst the other truly higher order expansions (e.g. Gobbi *et al.*, 2000).

2.1 Definition of the multi-layer problem

In the following, the Cartesian coordinate system is adopted, with horizontal axes x and y located on the still water plane and the vertical axis z pointing upwards from the still water level (SWL). The water column is divided into an arbitrary number N of imaginary layers, numbered from the top to the bottom and having exactly the same physical properties including density. In order to ensure the continuous medium characterisation of the fluid, the continuity of both pressure and velocity variables is enforced at layer interfaces through some additional internal boundary conditions. In the next subsections, the multi-layer problem is set out and the starting assumptions for the derivation of the model are expounded.

2.1.1 Geometry of the system

A full definition sketch of the general N-layer system is presented in Figure 2.1, given all the characteristic scales and dimensional dependent variables relative to the wave motion:

- a_0 and l_0 are the characteristic wave amplitude and wave length.
- h_0 and d_n are the characteristic water depth and thickness of the layer n.
- $b_n = \sum_{m=1}^{n} d_m$ is the characteristic depth of the layer n, and by convention $b_0 = a_0$.
- At each point of the layer n, the fluid flow can be described by $\boldsymbol{U}_n = (U_n, V_n)^{\mathrm{T}}$, W_n and p_n, designating respectively the horizontal and vertical particle velocities and the total pressure, which are spatiotemporal variables in function of (x, y, z, t); the evaluation of $\boldsymbol{U}_n$ at the specific depth $\kappa_n(x, y, t)$ is noted $\boldsymbol{u}_n = \boldsymbol{U}_n(x, y, z = \kappa_n(x, y, t), t)$.

- $\forall\ 1 \leqslant n \leqslant N-1$, $\eta_n(x,y,t)$ marks the interface between layers n and $n+1$ with respect to the still water level, while top and bottom borders are given by the free surface elevation $\eta_0 = \zeta(x,y,t)$ and the seabed location $\eta_N = -h(x,y,t)$.

It is pointed out that the model is applicable to uneven bathymetries, including a time-dependency of the bottom function h for the simulation of submarine landslides.

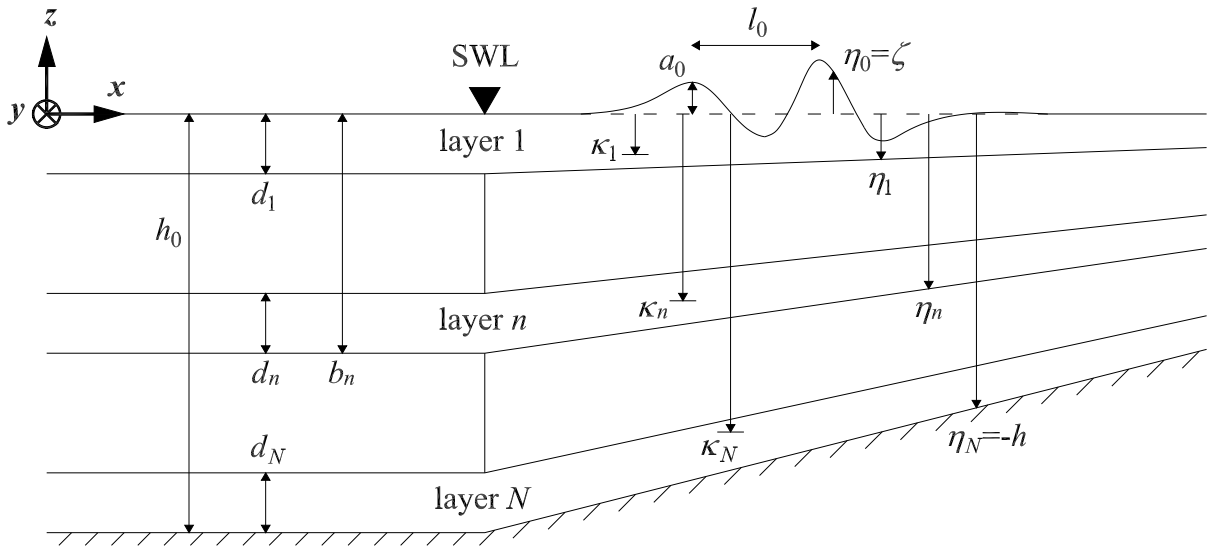

Figure 2.1: Geometric layout of the multi-layer system

2.1.2 Simplifying hypotheses

Following the general framework of all Boussinesq type derivations, we define the nonlinearity and dispersion dimensionless parameters, for both the overall system and the layer n:

$$\varepsilon_0 = \frac{a_0}{h_0}\,,\ \mu_0 = \frac{h_0}{l_0}\,,\ \varepsilon_n = \frac{a_0}{d_n}\,,\ \mu_n^2 = \frac{d_n h_0}{l_0^2} \tag{2.1}$$

It should be noted that these parameters are closely related by $\varepsilon_0\mu_0^2 = \varepsilon_n\mu_n^2$.

Now, the derivation of the model rests on the next fundamental hypotheses:

- The fluid, in this case the (sea)water, is assumed incompressible; the meaning here, in the mathematical sense of the term, of this very common hypothesis in numerical ocean engineering is explored in the following subsection.

- To the magnitude of scales involved during the propagation of oceanic waves, viscous effects can be assumed insignificant so that the flow is considered inviscid.

- As the depth-integration of the equations purely bans waves from curling and breaking, the flow is assumed laminar and the turbulence is fully neglected.

- Regarding the dispersive expansion of equations, the needed long wave perturbation analysis is based here on the new weak dispersion assumption $\mu_n^2 \ll 1$ and then utilises μ_n^2 as the small parameter in the power series developments; it can be noted that this condition is less restrictive than the usual $\mu_0^2 \ll 1$ assumption of the classical one-layer Boussinesq type approximations, regardless of the order of accuracy.
- Horizontal vorticity is assumed to be at least second order $O\left(\mu_n^4\right)$, whereas components of the vertical vorticity start at order zero $O\left(1\right)$; thereby in this case, the next first order dispersive derivation only allows the full reproduction of horizontal eddies.

2.1.3 Incompressibility of the fluid

This subsection aims to justify the incompressibility hypothesis in the ocean context. Generally speaking, the continuity equation for mass conservation reads

$$\frac{\mathrm{d}\rho}{\mathrm{d}t} + \rho \nabla . \boldsymbol{u} = 0 \tag{2.2}$$

where ρ is the density and $\boldsymbol{u} = (u, v, w)^{\mathrm{T}}$ the three-dimensional velocity of fluid particles.

Let the following characteristic scales of the motion be defined:

- Characteristic length L;
- Characteristic velocity U;
- Characteristic time $T = L/U$;
- Characteristic pressure $P = \rho U^2$.

By definition, compressibility effects can be disregarded when $\left|\frac{\mathrm{d}\rho}{\rho}\right| \ll 1$, that is to say when $\left|\frac{1}{\rho}\frac{\mathrm{d}\rho}{\mathrm{d}t}\right| \ll \frac{1}{\mathrm{d}t} \sim \frac{U}{L}$, which is equivalent to $|\nabla . \boldsymbol{u}| \ll \frac{U}{L}$ given the equation (2.2).

Noting that $\frac{1}{\rho}\frac{\mathrm{d}\rho}{\mathrm{d}t} = \frac{1}{\rho}\frac{\mathrm{d}\rho}{\mathrm{d}p}\frac{\mathrm{d}p}{\mathrm{d}t}$ and using the basic definition of the sound celerity $c^2 = \left.\frac{\partial p}{\partial \rho}\right|_s$ in the fluid, the condition of incompressibility then becomes $\left|\frac{1}{\rho c^2}\frac{\mathrm{d}p}{\mathrm{d}t}\right| \ll \frac{U}{L}$.

The momentum Euler equation, written in the vectorial form, reads

$$\rho \frac{\mathrm{d}\boldsymbol{u}}{\mathrm{d}t} = -\nabla p + \rho \boldsymbol{g} \tag{2.3}$$

where $\boldsymbol{g} = (0, 0, -g)^{\mathrm{T}}$ represents the acceleration vector of gravity.

The multiplication by $\boldsymbol{u}$ of this equation immediately gives

$$\begin{aligned} \rho \boldsymbol{u} . \frac{\mathrm{d}\boldsymbol{u}}{\mathrm{d}t} &= -\boldsymbol{u} . \nabla p + \rho \boldsymbol{u} . \boldsymbol{g} \\ \frac{1}{2}\rho \frac{\mathrm{d}\boldsymbol{u}^2}{\mathrm{d}t} &= -\boldsymbol{u} . \nabla p - \rho w g \end{aligned} \tag{2.4}$$

Using the equation (2.4), the term $\frac{\mathrm{d}p}{\mathrm{d}t} = \frac{\partial p}{\partial t} + \boldsymbol{u}.\nabla p$ can be developped as follows:

$$\frac{\mathrm{d}p}{\mathrm{d}t} = \frac{\partial p}{\partial t} - \frac{1}{2}\rho\frac{\mathrm{d}\boldsymbol{u}^2}{\mathrm{d}t} - \rho w g \tag{2.5}$$

So that the condition of incompressibility now reads

$$\left|\frac{1}{\rho c^2}\frac{\partial p}{\partial t} - \frac{1}{2c^2}\frac{\mathrm{d}\boldsymbol{u}^2}{\mathrm{d}t} - \frac{wg}{c^2}\right| \ll \frac{U}{L} \tag{2.6}$$

In order to justify this inequality, two conditions are studied separately.

- Condition 1 (Mach number $M = \frac{U}{c}$):

$$\left|\frac{1}{\rho c^2}\frac{\partial p}{\partial t} - \frac{1}{2c^2}\frac{\mathrm{d}\boldsymbol{u}^2}{\mathrm{d}t}\right| \ll \frac{U}{L} \tag{2.7}$$

  Using the previous characteristic scales, the inequality (2.7) reduces to

$$\begin{aligned}
\left|\frac{1}{\rho c^2}\frac{P}{T} - \frac{1}{2c^2}\frac{U^2}{T}\right| &\ll \frac{U}{L} \\
\left|\frac{1}{\rho c^2}\frac{\rho U^2 U}{L} - \frac{1}{2c^2}\frac{U^2 U}{L}\right| &\ll \frac{U}{L} \\
\left|M^2\frac{U}{L} - \frac{M^2}{2}\frac{U}{L}\right| &\ll \frac{U}{L} \\
\left|\frac{M^2}{2}\right| &\ll 1 \\
M^2 &\ll 1
\end{aligned} \tag{2.8}$$

  The sound celerity in oceanic waters is approximately $c \approx 1470$ m/s, so that for the average velocity of a tsunami wave of 750 km/h (208 m/s), a value still largely superior to the average forward speed of a hurricane, this first condition is likely to be always verified within the present long wave simulation context in play.

- Condition 2 (scale height $H_{\mathrm{sc}} = \frac{c^2}{g}$):

$$\left|\frac{wg}{c^2}\right| \ll \frac{U}{L} \tag{2.9}$$

  Similarly, with the similitude $w \sim U$, the condition (2.9) is reduced to

$$\begin{aligned}
\left|\frac{Ug}{c^2}\right| &\ll \frac{U}{L} \\
\left|\frac{Lg}{c^2}\right| &\ll 1 \\
L &\ll H_{\mathrm{sc}}
\end{aligned} \tag{2.10}$$

  Given the ocean scale height $H_{\mathrm{sc}} \approx 220$ km, this second condition shall be satisfied by considering simulation spatial scales small enough in comparison to this value.

Consequently from (2.7) and (2.9), it can be deduced that

$$\left|\frac{1}{\rho c^2}\frac{\partial p}{\partial t} - \frac{1}{2c^2}\frac{\mathrm{d}\boldsymbol{u}^2}{\mathrm{d}t}\right| + \left|\frac{wg}{c^2}\right| \ll \frac{U}{L} \tag{2.11}$$

Finally, the following inequality validates the condition of incompressibility (2.6):

$$\left|\frac{1}{\rho c^2}\frac{\partial p}{\partial t} - \frac{1}{2c^2}\frac{\mathrm{d}\boldsymbol{u}^2}{\mathrm{d}t} - \frac{wg}{c^2}\right| \leqslant \left|\frac{1}{\rho c^2}\frac{\partial p}{\partial t} - \frac{1}{2c^2}\frac{\mathrm{d}\boldsymbol{u}^2}{\mathrm{d}t}\right| + \left|\frac{wg}{c^2}\right| \ll \frac{U}{L} \tag{2.12}$$

2.1.4 Influence of inertial forces

Any ocean wave modelling subject requires an adequate coordinate system. The system most commonly used in coastal engineering is the rectilinear Cartesian coordinate system (x, y, z), in which the earth is assumed to be flat. In fact, a spherical coordinate system $\left(r, \frac{\pi}{2} - \phi, \theta\right)$ would be more realistic, but it is also much more complicated to implement. The usual convention, followed here, consists in defining a local plane at the surface of the earth, in which the x axis points east, the y axis points north and the z axis points upward from the mean ocean level, in the direction opposite to the gravitational vector (see Figure 2.2). A correction of horizontal distances is then applied to account for the sphericity of the earth.

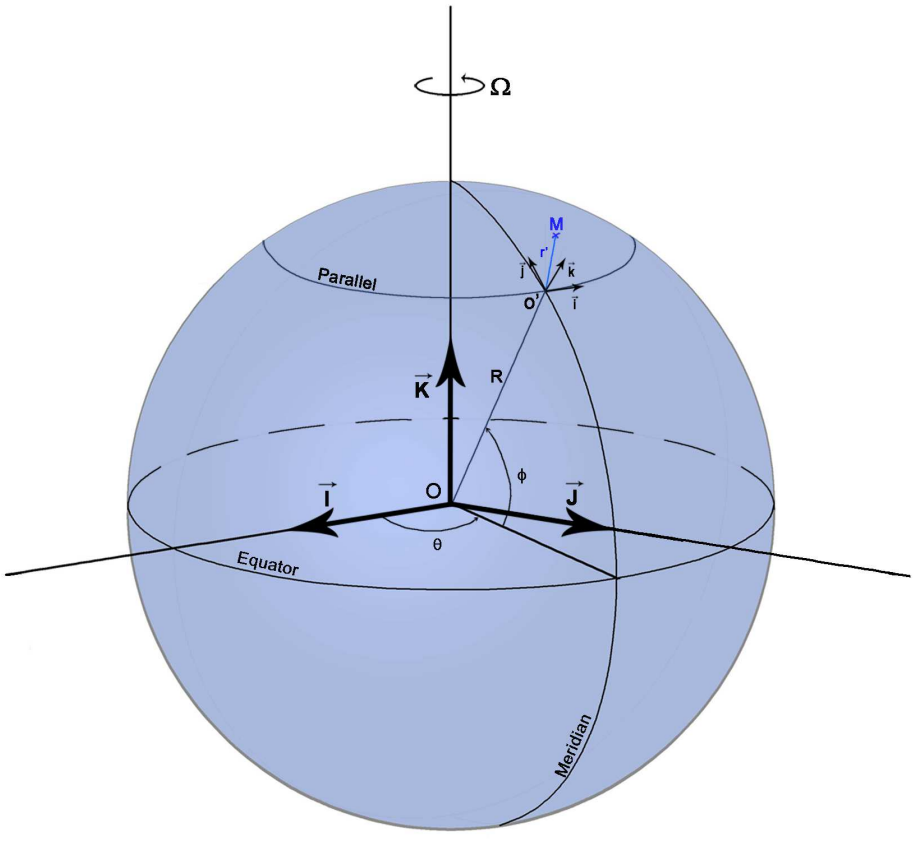

Figure 2.2: Conventional local coordinate system in ocean engineering

Amongst the main forces acting on a fluid particle in the ocean, we may cite gravity, the pressure gradient, the bottom friction and inertial forces. Actually, rather than a true force, the latter is a compensation device to account for the acceleration of the particle induced by the rotation of the earth $\boldsymbol{\Omega}$ (Knauss, 1996). Inertial forces are conventionally quantified by a fictitious volumetric force $\boldsymbol{F}_\Omega$, directly related to this acceleration $\boldsymbol{a}_\Omega$ by $\boldsymbol{F}_\Omega = -\rho \boldsymbol{a}_\Omega$. The force $\boldsymbol{F}_\Omega$ is generally split into two terms: the well known Coriolis kinematic component $\boldsymbol{F}_\mathrm{c}$ and a static driving component $\boldsymbol{F}_\mathrm{e}$. For most problems, the accelerations and forces in play are sufficiently large so that inertial effects can be ignored. However, in the case of large scale simulations, for example the oceanic propagation of tsunamis, the Coriolis acceleration can have significative effects on the kinematics of the flow and should be included in the governing equations of numerical models. Regarding the leading order terms of the static driving acceleration, the z component is usually folded into the gravity value g, while the y component seems to be simply ignored without apparent reason. A derivation of inertial accelerations in the rotating local Cartesian frame of reference is presented below.

Relative motion

The studied system is the earth, characterised by its centre O and radius R (Figure 2.2). We denote by O′ a point on the surface of the earth and by M some oceanic fluid particle. Let $\mathcal{R} = (\mathrm{O}; \mathbf{I}, \mathbf{J}, \mathbf{K})$ be the fixed frame of reference in space, $\mathcal{R}' = (\mathrm{O}'; \mathbf{i}, \mathbf{j}, \mathbf{k})$ the usual rotating mobile frame of reference and $\boldsymbol{\Omega} = \Omega \mathbf{K}$ the angular velocity vector of $\mathcal{R}'$ with respect to $\mathcal{R}$. By convention, the absolute total derivative in time with respect to $\mathcal{R}$ of some variable $\boldsymbol{\varphi}$ is written $\left(\frac{\mathrm{d}\boldsymbol{\varphi}}{\mathrm{d}t}\right)_{(\mathcal{R})} = \dot{\boldsymbol{\varphi}}$, and the relative derivative with respect to $\mathcal{R}'$ is written $\left(\frac{\mathrm{d}\boldsymbol{\varphi}}{\mathrm{d}t}\right)_{(\mathcal{R}')} = \dot{\boldsymbol{\varphi}}'$.

Before calculating inertial accelerations, we recall the fundamental theorem of Poisson that gives the total derivative in time of any unitary vector $\mathbf{e}$ in a rotating frame of reference:

$$\dot{\mathbf{e}} = \boldsymbol{\Omega} \times \mathbf{e} \tag{2.13}$$

This property can be easily verified by projecting the three basis unitary vectors $\mathbf{i}$, $\mathbf{j}$, $\mathbf{k}$ of the rotating frame of reference $\mathcal{R}'$ on the basis $(\mathbf{I}, \mathbf{J}, \mathbf{K})$ of the fixed frame of reference $\mathcal{R}$:

$$\begin{aligned} \mathbf{i} &= -\sin\theta \mathbf{I} + \cos\theta \mathbf{J} \\ \mathbf{j} &= -\sin\phi\cos\theta \mathbf{I} - \sin\phi\sin\theta \mathbf{J} + \cos\phi \mathbf{K} \\ \mathbf{k} &= \cos\phi\cos\theta \mathbf{I} + \cos\phi\sin\theta \mathbf{J} + \sin\phi \mathbf{K} \end{aligned} \tag{2.14}$$

The position vector $\overrightarrow{\mathrm{OM}}$ of the fluid particle M is given by

$$\begin{aligned} \boldsymbol{r} &= \boldsymbol{R} + \boldsymbol{r}' \\ &= R\mathbf{k} + (x\mathbf{i} + y\mathbf{j} + z\mathbf{k}) \\ &= x\mathbf{i} + y\mathbf{j} + (R+z)\,\mathbf{k} \end{aligned} \tag{2.15}$$

The total velocity $\left(\frac{\mathrm{d}\boldsymbol{r}}{\mathrm{d}t}\right)_{(\mathcal{R})}$ of the fluid particle M with respect to $\mathcal{R}$ reads

$$\begin{aligned} \dot{\boldsymbol{r}} &= (\dot{x}\mathbf{i} + \dot{y}\mathbf{j} + \dot{z}\mathbf{k}) + \left(x\dot{\mathbf{i}} + y\dot{\mathbf{j}} + (R+z)\,\dot{\mathbf{k}}\right) \\ &= \dot{\boldsymbol{r}}' + x\boldsymbol{\Omega} \times \mathbf{i} + y\boldsymbol{\Omega} \times \mathbf{j} + (R+z)\,\boldsymbol{\Omega} \times \mathbf{k} \\ &= \dot{\boldsymbol{r}}' + \boldsymbol{\Omega} \times \boldsymbol{r} \end{aligned} \tag{2.16}$$

The total acceleration $\left(\frac{\mathrm{d}^2\boldsymbol{r}}{\mathrm{d}t^2}\right)_{(\mathcal{R})} = \left(\frac{\mathrm{d}\dot{\boldsymbol{r}}}{\mathrm{d}t}\right)_{(\mathcal{R})}$ of the fluid particle M with respect to $\mathcal{R}$ reads

$$\begin{aligned}\ddot{\boldsymbol{r}} &= (\ddot{x}\mathbf{i} + \ddot{y}\mathbf{j} + \ddot{z}\mathbf{k}) + \left(\dot{x}\dot{\mathbf{i}} + \dot{y}\dot{\mathbf{j}} + \dot{z}\dot{\mathbf{k}}\right) + \dot{\boldsymbol{\Omega}} \times \boldsymbol{r} + \boldsymbol{\Omega} \times \dot{\boldsymbol{r}} \\ &= \ddot{\boldsymbol{r}}' + 2\boldsymbol{\Omega} \times \dot{\boldsymbol{r}}' + \dot{\boldsymbol{\Omega}} \times \boldsymbol{r} + \boldsymbol{\Omega} \times (\boldsymbol{\Omega} \times \boldsymbol{r})\end{aligned} \tag{2.17}$$

Finally, the expression (2.17) for the absolute total acceleration $\boldsymbol{a}_\mathrm{a}$ can be rewritten as the sum of a relative total acceleration $\boldsymbol{a}_\mathrm{r}$, which is the acceleration measured by an earth observer and generally reproduced by numerical models, and the inertial acceleration $\boldsymbol{a}_\Omega$ composed of the Coriolis acceleration term $\boldsymbol{a}_\mathrm{c}$ and a driving acceleration term $\boldsymbol{a}_\mathrm{e}$, as follows:

$$\begin{aligned}\boldsymbol{a}_\mathrm{a} &= \boldsymbol{a}_\mathrm{r} + \boldsymbol{a}_\Omega \\ \boldsymbol{a}_\Omega &= \boldsymbol{a}_\mathrm{c} + \boldsymbol{a}_\mathrm{e}\end{aligned} \tag{2.18}$$

where each component $\boldsymbol{a}_\mathrm{r}$, $\boldsymbol{a}_\mathrm{c}$ and $\boldsymbol{a}_\mathrm{e}$ respectively reads

$$\begin{aligned}\boldsymbol{a}_\mathrm{r} &= \ddot{\boldsymbol{r}}' = \dot{\boldsymbol{u}}' \\ \boldsymbol{a}_\mathrm{c} &= 2\boldsymbol{\Omega} \times \dot{\boldsymbol{r}}' = 2\boldsymbol{\Omega} \times \boldsymbol{u}' \\ \boldsymbol{a}_\mathrm{e} &= \dot{\boldsymbol{\Omega}} \times \boldsymbol{r} + \boldsymbol{\Omega} \times (\boldsymbol{\Omega} \times \boldsymbol{r})\end{aligned} \tag{2.19}$$

Coriolis acceleration

The Coriolis acceleration $\boldsymbol{a}_\mathrm{c}$ in (2.19) can be explicitly evaluated in the local mobile coordinate system by projecting $\boldsymbol{\Omega}$ on the rotating frame of reference $\mathcal{R}'$:

$$\boldsymbol{a}_\mathrm{c} = 2\Omega \begin{pmatrix} 0 \\ \cos\phi \\ \sin\phi \end{pmatrix} \times \begin{pmatrix} u' \\ v' \\ w' \end{pmatrix} = 2\Omega \begin{pmatrix} \cos\phi\, w' - \sin\phi\, v' \\ \sin\phi\, u' \\ -\cos\phi\, u' \end{pmatrix} \tag{2.20}$$

The Coriolis acceleration directly depends on the velocity components of the particle. This acceleration allows the interpretation of many phenomena at the surface of the earth, for example the motion of air masses and hurricanes, and the trajectory deviation of long-range projectiles and during free fall. Actually, some particle in motion at the surface of the earth suffers an east deflection in the Northern Hemisphere and a west deflection in the Southern Hemisphere. For displacements along meridians, this acceleration is due to the fact that different parts of the earth rotate with different velocities according to the distance from the rotation axis. For displacements along parallels, this acceleration results from the centrifugal or centripetal force induced by the rotation, according to a motion in the same direction or in the opposite direction to the rotation.

Driving acceleration

The driving acceleration $\boldsymbol{a}_\mathrm{e}$ in (2.19) is composed of two characteristic terms, commonly referred to as a tangential component $\boldsymbol{a}_\mathrm{et}$ and a centripetal component $\boldsymbol{a}_\mathrm{ec}$:

$$\boldsymbol{a}_\mathrm{e} = \boldsymbol{a}_\mathrm{et} + \boldsymbol{a}_\mathrm{ec} \tag{2.21}$$

where both components $\boldsymbol{a}_{\mathrm{et}}$ and $\boldsymbol{a}_{\mathrm{ec}}$ respectively read

$$\begin{aligned} \boldsymbol{a}_{\mathrm{et}} &= \dot{\boldsymbol{\Omega}} \times \boldsymbol{r} \\ \boldsymbol{a}_{\mathrm{ec}} &= \boldsymbol{\Omega} \times (\boldsymbol{\Omega} \times \boldsymbol{r}) \end{aligned} \tag{2.22}$$

By assuming a constant angular rotation of the earth, the tangential acceleration in (2.22) is zero, so that the driving acceleration is reduced to the centripetal acceleration:

$$\boldsymbol{a}_{\mathrm{e}} = \boldsymbol{\Omega} \times (\boldsymbol{\Omega} \times \boldsymbol{r}) \tag{2.23}$$

and can be expressed in the rotating frame of reference $\mathcal{R}'$ as

$$\boldsymbol{a}_{\mathrm{e}} = \Omega^2 \begin{pmatrix} 0 \\ \cos\phi \\ \sin\phi \end{pmatrix} \times \left[\begin{pmatrix} 0 \\ \cos\phi \\ \sin\phi \end{pmatrix} \times \begin{pmatrix} x \\ y \\ R+z \end{pmatrix} \right] = \Omega^2 \begin{pmatrix} -x \\ \sin\phi\cos\phi\,(R+z) - \sin^2\phi\, y \\ -\cos^2\phi\,(R+z) + \cos\phi\sin\phi\, y \end{pmatrix} \tag{2.24}$$

It can be noted that the driving acceleration is a function of position only and is independent of velocity. They can be important in determining the gravitational field of the earth and establishing the related equal potential surfaces (Knauss, 1996).

Finally, it is noted that the position of the fluid particle M is described by its latitude ϕ and its coordinates (x, y, z) in the local rotating frame of reference $\mathcal{R}'$. As for the earth, it is characterised by its volumetric mean radius $R \approx 6371.0\,\mathrm{km}$ and its angular velocity $\Omega = \frac{2\pi}{T_{\mathrm{sideral}}} \approx \frac{2\pi}{86164.091} \approx 7.2921159\mathrm{e}^{-5}$ rad/s, calculated from the sideral day.

2.2 Mathematical formulation of governing equations

Usually, by nondimensionalising the governing equations of a given fluid dynamics problem, one makes the physical parameters of the system appear. In the Boussinesq context, once such parameters are identified, the idea basically consists of approximating the dispersion process from a long wave perturbation analysis expanded in terms of the respective parameter.

According to previous hypotheses, the inviscid response of the (sea)water to some flow motion can be described by the Euler momentum equations coupled to the incompressible continuity equation, and the dynamic and kinematic closure boundary conditions of the model.

Before performing a nondimensionalisation of the complete primitive system of equations, some suitable characteristic scales proper to the studied problem must be defined. We recall here the characteristic scales previously mentioned in the first section:

- Characteristic water depth h_0;
- Characteristic layer thickness d_n;
- Characteristic height of the wave motion a_0;
- Characteristic length of the wave motion l_0;
- Characteristic time of the wave motion $t_0 = l_0/\sqrt{gh_0}$.

2.2.1 Nondimensionalisation of the Euler system

One way to nondimensionalise the Euler equations and the boundary conditions is following Lynett (2002). Dimensionless variables are thus defined from the characteristic scales of the system in the following way (dimensional variables are denoted with asterisks):

$$\begin{aligned} (x,y) = \frac{(x^*,y^*)}{l_0}\,, \quad z_n = \frac{z^*}{d_n} \text{ for } z^* \in \text{layer } n\,, \quad t = \frac{t^*}{t_0}\,, \quad h = \frac{h^*}{h_0} \\ \zeta = \frac{\zeta^*}{a_0}\,, \quad \eta_n = \frac{\eta_n^*}{b_n}\,, \quad p_n = \frac{p_n^*}{\rho g a_0}\,, \quad \boldsymbol{U}_n = \frac{\boldsymbol{U}_n^*}{\varepsilon_0\sqrt{gh_0}}\,, \quad W_n = \frac{W_n^*}{\varepsilon_0\mu_0\sqrt{gh_0}} \end{aligned} \tag{2.25}$$

where ρ and g represent the (sea)water density and the gravity acceleration.

Equations of motion

The dimensional incompressible Euler system of equations reads inside the layer n:

$$\begin{cases} \nabla.\boldsymbol{U}_n + \dfrac{\partial W_n}{\partial z} = 0 \\ \dfrac{\partial \boldsymbol{U}_n}{\partial t} + \boldsymbol{U}_n.\nabla\boldsymbol{U}_n + W_n\dfrac{\partial \boldsymbol{U}_n}{\partial z} = -\dfrac{1}{\rho}\nabla p_n \\ \dfrac{\partial W_n}{\partial t} + \boldsymbol{U}_n.\nabla W_n + W_n\dfrac{\partial W_n}{\partial z} = -\left(\dfrac{1}{\rho}\dfrac{\partial p_n}{\partial z} + g\right) \end{cases} \tag{2.26}$$

where $\nabla = (\partial/\partial x, \partial/\partial y)^{\mathrm{T}}$ denotes the horizontal gradient operator.

The nondimensionalisation of (2.26) using the variables given in (2.25) then leads to

$$\begin{cases} \dfrac{d_n}{h_0}\nabla.\boldsymbol{U}_n + \dfrac{\partial W_n}{\partial z_n} = 0 \\ \dfrac{\partial \boldsymbol{U}_n}{\partial t} + \varepsilon_0\boldsymbol{U}_n.\nabla\boldsymbol{U}_n + \varepsilon_n W_n\dfrac{\partial \boldsymbol{U}_n}{\partial z_n} = -\nabla p_n \\ \mu_n^2\left(\dfrac{\partial W_n}{\partial t} + \varepsilon_0\boldsymbol{U}_n.\nabla W_n\right) + \varepsilon_0\mu_0^2 W_n\dfrac{\partial W_n}{\partial z_n} = -\left(\dfrac{\partial p_n}{\partial z_n} + \dfrac{1}{\varepsilon_n}\right) \end{cases} \tag{2.27}$$

External boundary conditions

The fluid domain is bounded by the free surface and the seabed. The respective dimensional dynamic and kinematic conditions along both moving boundaries are given by

$$\begin{aligned} & p_1 = p_{\mathrm{atm}}\,, \text{ at } z = \zeta \\ & W_1 = \left.\frac{\mathrm{d}z}{\mathrm{d}t}\right|_{z=\zeta} = \frac{\partial\zeta}{\partial t} + \boldsymbol{U}_1.\nabla\zeta\,, \text{ at } z = \zeta \\ & W_N = \left.\frac{\mathrm{d}z}{\mathrm{d}t}\right|_{z=-h} = -\frac{\partial h}{\partial t} - \boldsymbol{U}_N.\nabla h\,, \text{ at } z = -h = \eta_N \end{aligned} \tag{2.28}$$

and in nondimensional form by

$$\begin{aligned} p_1 &= \frac{p_{\rm atm}}{\rho g a_0}\,,\ \text{at } z_1 = \varepsilon_1\zeta \\ W_1 &= \frac{\partial\zeta}{\partial t} + \varepsilon_0 \boldsymbol{U}_1.\nabla\zeta\,,\ \text{at } z_1 = \varepsilon_1\zeta \\ W_N &= -\frac{1}{\varepsilon_0}\frac{\partial h}{\partial t} - \boldsymbol{U}_N.\nabla h\,,\ \text{at } z_N = -\frac{h_0}{d_N}h = \frac{b_N}{d_N}\eta_N \end{aligned} \tag{2.29}$$

Internal boundary conditions

In addition, a continuity condition for pressure and velocities is imposed at layer interfaces. These internal boundary conditions read in terms of dimensional variables:

$$\begin{aligned} p_n &= p_{n+1}\,,\ \text{at } z = \eta_n\,,\ 1 \leqslant n \leqslant N-1 \\ \boldsymbol{U}_n &= \boldsymbol{U}_{n+1}\,,\ \text{at } z = \eta_n\,,\ 1 \leqslant n \leqslant N-1 \\ W_n &= W_{n+1}\,,\ \text{at } z = \eta_n\,,\ 1 \leqslant n \leqslant N-1 \end{aligned} \tag{2.30}$$

and in nondimensional form, (2.30) becomes

$$\begin{aligned} p_n &= p_{n+1}\,,\ \text{at } z_n = \frac{b_n}{d_n}\eta_n \text{ and } z_{n+1} = \frac{b_n}{d_{n+1}}\eta_n\,,\ 1 \leqslant n \leqslant N-1 \\ \boldsymbol{U}_n &= \boldsymbol{U}_{n+1}\,,\ \text{at } z_n = \frac{b_n}{d_n}\eta_n \text{ and } z_{n+1} = \frac{b_n}{d_{n+1}}\eta_n\,,\ 1 \leqslant n \leqslant N-1 \\ W_n &= W_{n+1}\,,\ \text{at } z_n = \frac{b_n}{d_n}\eta_n \text{ and } z_{n+1} = \frac{b_n}{d_{n+1}}\eta_n\,,\ 1 \leqslant n \leqslant N-1 \end{aligned} \tag{2.31}$$

The derivation of the multi-layer first order dispersive model presented below does not take account of inertial terms. However, the inclusion of these forces is trivial and would start from the addition of accelerations (2.20) and (2.24) into the dimensional Euler system (2.26), by setting $\boldsymbol{u}' \equiv (\boldsymbol{U}, W)^{\rm T}$ for the relative velocity of the rotating frame of reference.

2.2.2 Approximation of velocities and pressure

The long wave perturbation analysis now consists in expanding the dimensionless physical dependent variables, in this case the velocities and pressure of the layer n, as an infinite power series of the assumed small dispersion parameter μ_n^2 of the form:

$$\varphi_n = \sum_{m=0}^{+\infty} \mu_n^{2m}\varphi_n^{[m]}\,,\ \varphi = \boldsymbol{U}, W, p \tag{2.32}$$

In addition, given the vector vorticity $\boldsymbol{\omega}_n$ defined as the rotational of the velocity field as

$$\boldsymbol{\omega}_n = \nabla \times (\boldsymbol{U}_n, W_n)^{\rm T} = \left(\frac{\partial W_n}{\partial y} - \frac{\partial V_n}{\partial z_n}, \frac{\partial U_n}{\partial z_n} - \frac{\partial W_n}{\partial x}, \frac{\partial V_n}{\partial x} - \frac{\partial U_n}{\partial y}\right)^{\rm T}, \tag{2.33}$$

the previous hypotheses on the vorticity of the flow can then be written in the following way, for both horizontal and vertical components:

$$\begin{aligned} &\frac{\partial \boldsymbol{U}_n^{[0]}}{\partial z_n} = 0\,,\ \nabla W_n^{[0]} - \frac{\partial \boldsymbol{U}_n^{[1]}}{\partial z_n} = 0 \\ &\nabla \times \boldsymbol{U}_n = \frac{\partial V_n}{\partial x} - \frac{\partial U_n}{\partial y} = O\left(1\right) \end{aligned} \tag{2.34}$$

Vertical velocity

The application of expansion (2.32) to velocity variables within the continuity equation in (2.27) and both kinematic boundary conditions in (2.29), leads at leading order to

$$\begin{aligned} &\frac{d_n}{h_0}\nabla.\boldsymbol{U}_n^{[0]} + \frac{\partial W_n^{[0]}}{\partial z_n} = 0\,,\ \text{for}\ \frac{b_n}{d_n}\eta_n \leqslant z_n \leqslant \frac{b_{n-1}}{d_n}\eta_{n-1}\,,\ 1 \leqslant n \leqslant N \\ &W_1^{[0]} = \frac{\partial \zeta}{\partial t} + \varepsilon_0 \boldsymbol{U}_1^{[0]}.\nabla\zeta\,,\ \text{at}\ z_1 = \varepsilon_1\zeta \\ &W_N^{[0]} = -\frac{1}{\varepsilon_0}\frac{\partial h}{\partial t} - \boldsymbol{U}_N^{[0]}.\nabla h\,,\ \text{at}\ z_N = -\frac{h_0}{d_N}h \end{aligned} \tag{2.35}$$

By integrating the continuity equation in (2.35) with respect to z_n, the expression of the first order component of the vertical velocity W_n can be explicitly found:

$$W_n^{[0]} = -z_n\left(\frac{d_n}{h_0}\nabla.\boldsymbol{U}_n^{[0]}\right) + A_n\left(x,y,t\right) \tag{2.36}$$

where terms $A_n\left(x,y,t\right)$ are integration constants independent of z_n, which can be calculated using both the seabed and internal continuity kinematic conditions in (2.35) and (2.31):

- Application of the seabed condition:
  In layer N, the vertical velocity (2.36) reads at the bottom location:

$$W_N^{[0]}\left(z_N = -\frac{h_0}{d_N}h\right) = \frac{h_0}{d_N}h\left(\frac{d_N}{h_0}\nabla.\boldsymbol{U}_N^{[0]}\right) + A_N \tag{2.37}$$

  Equalling $W_N^{[0]}\left(z_N = -\frac{h_0}{d_N}h\right)$ to its expression in (2.35) gives the value of A_N:

$$A_N = -\nabla.\left(h\boldsymbol{U}_N^{[0]}\right) - \frac{1}{\varepsilon_0}\frac{\partial h}{\partial t} \tag{2.38}$$

- Application of the internal continuity condition for W:
  By defining the auxiliary variable $S_n^{[0]} = \frac{d_n}{h_0}\nabla.\boldsymbol{U}_n^{[0]}$, the vertical velocity (2.36) now reads at the interface η_n from both layers n and $n+1$:

$$\begin{aligned} &W_n^{[0]}\left(z_n = \frac{b_n}{d_n}\eta_n\right) = -\frac{b_n}{d_n}\eta_n S_n^{[0]} + A_n \\ &W_{n+1}^{[0]}\left(z_{n+1} = \frac{b_n}{d_{n+1}}\eta_n\right) = -\frac{b_n}{d_{n+1}}\eta_n S_{n+1}^{[0]} + A_{n+1} \end{aligned} \tag{2.39}$$

By applying the kinematic continuity condition in (2.31) for the vertical velocity W through internal layer interfaces, a relation between A_n and A_{n+1} is obtained:

$$A_n = A_{n+1} - \eta_n \left(\frac{b_n}{d_{n+1}} S_{n+1}^{[0]} - \frac{b_n}{d_n} S_n^{[0]} \right) \tag{2.40}$$

From (2.38) and (2.40), the complete expression of A_n, $1 \leqslant n \leqslant N-1$ is easily calculated:

$$A_n = -\nabla . \left(h \boldsymbol{U}_N^{[0]} \right) - \frac{1}{\varepsilon_0} \frac{\partial h}{\partial t} - \sum_{m=n}^{N-1} \eta_m \left(\frac{b_m}{d_{m+1}} S_{m+1}^{[0]} - \frac{b_m}{d_m} S_m^{[0]} \right) \tag{2.41}$$

So that the leading order component of the vertical velocity in the layer n can be written

$$W_n^{[0]} = -z_n S_n^{[0]} - T_n^{[0]} \tag{2.42}$$

where auxiliary variables $S_n^{[0]}$ and $T_n^{[0]}$ are given by

$$\begin{aligned} S_n^{[0]} &= \frac{d_n}{h_0} \nabla . \boldsymbol{U}_n^{[0]} \\ T_n^{[0]} &= \nabla . \left(h \boldsymbol{U}_N^{[0]} \right) + \frac{1}{\varepsilon_0} \frac{\partial h}{\partial t} + \sum_{m=n}^{N-1} \eta_m \left(\frac{b_m}{d_{m+1}} S_{m+1}^{[0]} - \frac{b_m}{d_m} S_m^{[0]} \right) , \ 1 \leqslant n \leqslant N-1 \\ T_N^{[0]} &= \nabla . \left(h \boldsymbol{U}_N^{[0]} \right) + \frac{1}{\varepsilon_0} \frac{\partial h}{\partial t} \end{aligned} \tag{2.43}$$

Horizontal velocity

From the hypothesis on vorticity components given in (2.34), the first order component of the horizontal velocity $\boldsymbol{U}_n$ can then be calculated as $\boldsymbol{U}_n^{[1]} = \int \nabla W_n^{[0]} \, \mathrm{d}z_n$:

$$\boldsymbol{U}_n^{[1]} = -\frac{z_n^2}{2} \nabla S_n^{[0]} - z_n \nabla T_n^{[0]} + \boldsymbol{B}_n \left(x, y, t \right) \tag{2.44}$$

where terms $\boldsymbol{B}_n \left(x, y, t \right)$ are integration constants independent of z_n.

At first order, the dispersive expansion (2.32) of the horizontal velocity reads

$$\boldsymbol{U}_n \left(x, y, z_n, t \right) = \boldsymbol{U}_n^{[0]} \left(x, y, t \right) + \mu_n^2 \boldsymbol{U}_n^{[1]} \left(x, y, z_n, t \right) + O\left(\mu_n^4 \right) \tag{2.45}$$

which, by replacing $\boldsymbol{U}_n^{[1]}$ by its expression in (2.44), becomes

$$\boldsymbol{U}_n = \boldsymbol{U}_n^{[0]} - \mu_n^2 \left(\frac{z_n^2}{2} \nabla S_n^{[0]} + z_n \nabla T_n^{[0]} - \boldsymbol{B}_n \right) + O\left(\mu_n^4 \right) \tag{2.46}$$

The evaluation $\boldsymbol{u}_n$ of $\boldsymbol{U}_n$ at the specific depth $\kappa_n \left(x, y, t \right)$ then reads

$$\boldsymbol{u}_n = \boldsymbol{U}_n^{[0]} - \mu_n^2 \left(\frac{\kappa_n^2}{2} \nabla S_n^{[0]} + \kappa_n \nabla T_n^{[0]} - \boldsymbol{B}_n \right) + O\left(\mu_n^4 \right) \tag{2.47}$$

So that $\boldsymbol{U}_n$ can now be expressed in terms of $\boldsymbol{u}_n$ by subtracting (2.47) from (2.46):

$$\boldsymbol{U}_n = \boldsymbol{u}_n - \mu_n^2 \left(\frac{z_n^2 - \kappa_n^2}{2} \nabla S_n^{[0]} + (z_n - \kappa_n) \nabla T_n^{[0]} \right) + O\left(\mu_n^4\right) \tag{2.48}$$

Finally, considering the general relation $\boldsymbol{u}_n = \boldsymbol{U}_n^{[0]} + O\left(\mu_n^2\right)$ in (2.47), the first order dispersive approximation of the horizontal velocity $\boldsymbol{U}_n$ can be rewritten as

$$\boldsymbol{U}_n = \boldsymbol{u}_n - \mu_n^2 \left(\frac{z_n^2 - \kappa_n^2}{2} \nabla S_n + (z_n - \kappa_n) \nabla T_n \right) + O\left(\mu_n^4\right) \tag{2.49}$$

where

$$\begin{aligned} S_n &= \frac{d_n}{h_0} \nabla . \boldsymbol{u}_n \\ T_n &= \nabla . \left(h \boldsymbol{u}_N\right) + \frac{1}{\varepsilon_0} \frac{\partial h}{\partial t} + \sum_{m=n}^{N-1} \eta_m \left(\frac{b_m}{d_{m+1}} S_{m+1} - \frac{b_m}{d_m} S_m \right), \ 1 \leqslant n \leqslant N-1 \\ T_N &= \nabla . \left(h \boldsymbol{u}_N\right) + \frac{1}{\varepsilon_0} \frac{\partial h}{\partial t} \end{aligned} \tag{2.50}$$

In the same way, the expression (2.42) of the vertical component $W_n^{[0]}$ can be updated to

$$w_n = -z_n S_n - T_n \tag{2.51}$$

So that the zero order dispersive approximation of the vertical velocity W_n reads

$$W_n = -z_n S_n - T_n + O\left(\mu_n^2\right) \tag{2.52}$$

Pressure

Now, to determine the pressure field in layer n, the vertical momentum equation given in (2.27) and the previous dispersive expansions of both horizontal (2.49) and vertical (2.52) velocities are used. Keeping leading order terms only, this equation reads

$$\mu_n^2 \left(\frac{\partial w_n}{\partial t} + \varepsilon_0 \boldsymbol{u}_n . \nabla w_n \right) + \varepsilon_0 \mu_0^2 w_n \frac{\partial w_n}{\partial z_n} + O\left(\mu_0^2 \mu_n^2, \mu_n^4\right) = -\frac{\partial p_n}{\partial z_n} - \frac{1}{\varepsilon_n} \tag{2.53}$$

The pressure p_n can then be simply calculated by replacing w_n by its expression in (2.51) before integrating the equation with respect to z_n, using both the free surface and internal continuity dynamic conditions in (2.29) and (2.31) to evaluate the integration constant.

In the case of layer 1, the expression of the pressure field thereby reads

$$\begin{aligned} p_1 =& \frac{p_{\text{atm}}}{\rho g a_0} - (z_1 - \varepsilon_1 \zeta) \left[\frac{1}{\varepsilon_1} + \varepsilon_0 \mu_0^2 \left(\frac{z_1 + \varepsilon_1 \zeta}{2} S_1^2 + T_1 S_1 \right) \right. \\ & \left. - \mu_1^2 \left(\frac{z_1 + \varepsilon_1 \zeta}{2} \left(\frac{\partial S_1}{\partial t} + \varepsilon_0 \boldsymbol{u}_1 . \nabla S_1 \right) + \frac{\partial T_1}{\partial t} + \varepsilon_0 \boldsymbol{u}_1 . \nabla T_1 \right) \right] + O\left(\mu_0^2 \mu_1^2, \mu_1^4\right) \end{aligned} \tag{2.54}$$

In the same way, the pressure field in layer n, $2 \leqslant n \leqslant N$, results as follows:

$$\begin{aligned} p_n =& \frac{p_{\text{atm}}}{\rho g a_0} + \zeta - \frac{z_n}{\varepsilon_n} - \left(z_n - \frac{b_{n-1}}{d_n}\eta_{n-1}\right)\left[\varepsilon_0\mu_0^2\left(\frac{z_n + \frac{b_{n-1}}{d_n}\eta_{n-1}}{2}S_n^2 + T_n S_n\right)\right. \\ & \left. -\mu_n^2\left(\frac{z_n + \frac{b_{n-1}}{d_n}\eta_{n-1}}{2}\left(\frac{\partial S_n}{\partial t} + \varepsilon_0 \boldsymbol{u}_n.\nabla S_n\right) + \frac{\partial T_n}{\partial t} + \varepsilon_0 \boldsymbol{u}_n.\nabla T_n\right)\right] \\ & - \sum_{m=1}^{n-1}\left(\frac{b_m}{d_m}\eta_m - \frac{b_{m-1}}{d_m}\eta_{m-1}\right)\left[\varepsilon_0\mu_0^2\left(\frac{\frac{b_m}{d_m}\eta_m + \frac{b_{m-1}}{d_m}\eta_{m-1}}{2}S_m^2 + T_m S_m\right)\right. \\ & \left. -\mu_m^2\left(\frac{\frac{b_m}{d_m}\eta_m + \frac{b_{m-1}}{d_m}\eta_{m-1}}{2}\left(\frac{\partial S_m}{\partial t} + \varepsilon_0 \boldsymbol{u}_m.\nabla S_m\right) + \frac{\partial T_m}{\partial t} + \varepsilon_0 \boldsymbol{u}_m.\nabla T_m\right)\right] \\ & + O\left(\mu_0^2\mu_1^2, ..., \mu_0^2\mu_n^2, \mu_1^4, ..., \mu_n^4\right) \end{aligned} \tag{2.55}$$

2.2.3 Derivation of dispersive equations

This subsection is aimed at a brief description of the derivation of the model under the multi-layer approach. The continuity equation is piecewisely integrated over the entire water depth, the horizontal momentum equation is developed for the superficial layer in terms of $\boldsymbol{u}_1$, and the internal kinematic continuity condition for the horizontal velocity $\boldsymbol{U}$ is used for the determination of lower layer velocities $\boldsymbol{u}_n$, $2 \leqslant n \leqslant N$.

Continuity equation

The continuity equation in (2.27) is integrated over the layer n as follows:

$$\int_{z_n=\frac{b_n}{d_n}\eta_n}^{z_n=\frac{b_{n-1}}{d_n}\eta_{n-1}} \left(\frac{d_n}{h_0}\nabla.\boldsymbol{U}_n + \frac{\partial W_n}{\partial z_n}\right) \mathrm{d}z_n = 0 \tag{2.56}$$

Then, by summing the equation (2.56) for all layers, and applying the Leibniz rule and all kinematic boundary conditions in (2.29) and (2.31) successively, the following exact expression of the depth-integrated continuity equation can be obtained:

$$\nabla.\sum_{n=1}^{N}\left(\frac{d_n}{h_0}\int_{z_n=\frac{b_n}{d_n}\eta_n}^{z_n=\frac{b_{n-1}}{d_n}\eta_{n-1}} \boldsymbol{U}_n \,\mathrm{d}z_n\right) + \frac{\partial\zeta}{\partial t} + \frac{1}{\varepsilon_0}\frac{\partial h}{\partial t} = 0 \tag{2.57}$$

Finally, by evaluating the integral in (2.57) from the expression (2.49) of the horizontal velocity $\boldsymbol{U}_n$, the first order dispersive approximation of the multi-layer mass equation reads

$$\begin{aligned} & \frac{\partial\zeta}{\partial t} + \frac{1}{\varepsilon_0}\frac{\partial h}{\partial t} + \nabla.\sum_{n=1}^{N}\left(\frac{b_{n-1}}{h_0}\eta_{n-1} - \frac{b_n}{h_0}\eta_n\right)\left[\boldsymbol{u}_n - \frac{\mu_n^2}{6}\left(\left(\frac{b_{n-1}}{d_n}\eta_{n-1}\right)^2\right.\right. \\ & \left.\left. + \frac{b_{n-1}\eta_{n-1}b_n\eta_n}{d_n^2} + \left(\frac{b_n}{d_n}\eta_n\right)^2 - 3\kappa_n^2\right)\nabla S_n \right. \\ & \left. - \frac{\mu_n^2}{2}\left(\frac{b_{n-1}}{d_n}\eta_{n-1} + \frac{b_n}{d_n}\eta_n - 2\kappa_n\right)\nabla T_n\right] + O\left(\mu_1^4, ..., \mu_N^4\right) = 0 \end{aligned} \tag{2.58}$$

The total mass flux markedly tends to zero at the shoreline when $\frac{b_{n-1}}{h_0}\eta_{n-1}-\frac{b_n}{h_0}\eta_n$, $1 \leqslant n \leqslant N$, tends to zero in (2.58). This natural shoreline boundary condition is in general automatically recovered by the fully nonlinear versions of Boussinesq type models (Wei *et al.*, 1995).

Momentum equation

The momentum equation for the superficial layer 1 is then easily obtained by substituting the expressions (2.49), (2.52) and (2.54) for velocities $\boldsymbol{U}_1$ and W_1 and the pressure p_1 into the horizontal Euler equation in (2.27), and keeping all nonlinear first order dispersive terms:

$$\begin{aligned}
&\frac{\partial \boldsymbol{u}_1}{\partial t}+\varepsilon_0\boldsymbol{u}_1.\nabla\boldsymbol{u}_1+\nabla\zeta+\frac{1}{\rho g a_0}\nabla p_{\text{atm}}+\mu_1^2\frac{\partial}{\partial t}\left(\frac{\kappa_1^2}{2}\nabla S_1+\kappa_1\nabla T_1\right)\\
&+\varepsilon_0\mu_1^2\left[\nabla\left(\frac{\kappa_1^2}{2}\boldsymbol{u}_1.\nabla S_1\right)+\nabla\left(\kappa_1\boldsymbol{u}_1.\nabla T_1\right)-\boldsymbol{u}_1\times\left(\nabla\times\left(\frac{\kappa_1^2}{2}\nabla S_1\right)\right)\right.\\
&\left.-\boldsymbol{u}_1\times\left(\nabla\times\left(\kappa_1\nabla T_1\right)\right)+\frac{z_1^2-\kappa_1^2}{2}\nabla S_1\times\left(\nabla\times\boldsymbol{u}_1\right)+\left(z_1-\kappa_1\right)\nabla T_1\times\left(\nabla\times\boldsymbol{u}_1\right)\right]\\
&+\varepsilon_0\mu_0^2\nabla\left(\frac{T_1^2}{2}-\zeta\frac{\partial T_1}{\partial t}\right)-\varepsilon_0^2\mu_0^2\nabla\left(\zeta\boldsymbol{u}_1.\nabla T_1\right)+\varepsilon_1\varepsilon_0\mu_0^2\nabla\left(\zeta T_1 S_1-\frac{\zeta^2}{2}\frac{\partial S_1}{\partial t}\right)\\
&-\varepsilon_1\varepsilon_0^2\mu_0^2\nabla\left(\frac{\zeta^2}{2}\boldsymbol{u}_1.\nabla S_1\right)+\varepsilon_1^2\varepsilon_0\mu_0^2\nabla\left(\frac{\zeta^2}{2}S_1^2\right)+O\left(\mu_0^2\mu_1^2,\mu_1^4\right)=0
\end{aligned}\tag{2.59}$$

Noticeably, this equation is slightly different from Lynett (2002), as both rotational terms $\boldsymbol{u}_1\times\left(\nabla\times\left(\frac{\kappa_1^2}{2}\nabla S_1\right)\right)$ and $\boldsymbol{u}_1\times\left(\nabla\times\left(\kappa_1\nabla T_1\right)\right)$ are no longer neglected and no assumption is made on the vertical vorticity (see (2.34)). Actually, the one and two-layer first order dispersive model implemented by Lynett was fully irrotational, with a vorticity field assumed at least of second order $O\left(\mu_n^4\right)$ for both horizontal and vertical components.

Moreover, as discussed in Hsiao *et al.* (2002), the z_1-dependency in equation (2.59) vanishes if the vertical vorticity $\nabla\times\boldsymbol{u}_1$ of layer 1 is assumed to be first order $O\left(\mu_1^2\right)$. However, the natural alternative to removing this vertical dependency consists in integrating the equation over the superficial layer as in Chen (2006). Although this approach is almost never explicitly used in practice, thus leaving the momentum equation in its non conservative form, it is supposed to be part of the derivation procedure of the so-called depth-integrated models.

Internal continuity condition for $\boldsymbol{U}$

The remaining lower layer velocities can be further calculated in function of the upper layer component, by the use of the internal kinematic continuity condition for $\boldsymbol{U}$ in (2.31), so that it is not necessary to solve a momentum equation within all layers:

$$\begin{aligned}
&\boldsymbol{u}_n+\frac{\mu_n^2}{2}\left[\left(\kappa_n^2-\left(\frac{b_{n-1}}{d_n}\eta_{n-1}\right)^2\right)\nabla S_n+2\left(\kappa_n-\frac{b_{n-1}}{d_n}\eta_{n-1}\right)\nabla T_n\right]-\boldsymbol{u}_{n-1}\\
&-\frac{\mu_{n-1}^2}{2}\left[\left(\kappa_{n-1}^2-\left(\frac{b_{n-1}}{d_{n-1}}\eta_{n-1}\right)^2\right)\nabla S_{n-1}+2\left(\kappa_{n-1}-\frac{b_{n-1}}{d_{n-1}}\eta_{n-1}\right)\nabla T_{n-1}\right]\\
&+O\left(\mu_{n-1}^4,\mu_n^4\right)=0\,,\ 2\leqslant n\leqslant N
\end{aligned}\tag{2.60}$$

Equations (2.58), (2.59) and (2.60) are the coupled governing equations for fully nonlinear first order dispersive waves under the multi-layer approach of Lynett (2002). The N-layer model has now been reduced from the $4N$ unknowns $\boldsymbol{U}_n$, W_n and p_n of the initial three-dimensional problem, to $2N+1$ unknowns ζ and $\boldsymbol{u}_n$ for the depth-integrated two-dimensional problem.

2.2.4 Back to the dimensional form

Once the multi-layer fully nonlinear Boussinesq type first order dispersive mathematical model is derived, governing equations are rewritten in the original dimensional form using (2.25). This simplified form will be used later for the numerical approximation of the model.

The auxiliary variables (2.50) are first redefined in dimensional form as

$$\begin{aligned} Q_n &= \nabla.\boldsymbol{u}_n \\ R_n &= \nabla.\left(h\boldsymbol{u}_N\right) + \frac{\partial h}{\partial t} + \sum_{m=n}^{N-1} \eta_m \left(Q_{m+1} - Q_m\right) \ , \ 1 \leqslant n \leqslant N-1 \\ R_N &= \nabla.\left(h\boldsymbol{u}_N\right) + \frac{\partial h}{\partial t} \end{aligned} \tag{2.61}$$

So that the vertical profiles of velocities (2.49) and (2.52), and pressure (2.54) and (2.55) are now respectively given in dimensional form by:

$$\boldsymbol{U}_n = \boldsymbol{u}_n - \frac{z^2-\kappa_n^2}{2}\nabla Q_n - \left(z-\kappa_n\right)\nabla R_n \tag{2.62}$$

$$W_n = -zQ_n - R_n \tag{2.63}$$

$$\begin{aligned} p_1 =& p_{\text{atm}} + \rho g\left(\zeta - z\right) + \rho\frac{z^2-\zeta^2}{2}\left(\frac{\partial Q_1}{\partial t} + \boldsymbol{u}_1.\nabla Q_1 - Q_1^2\right) \\ &+ \rho\left(z-\zeta\right)\left(\frac{\partial R_1}{\partial t} + \boldsymbol{u}_1.\nabla R_1 - R_1 Q_1\right) \end{aligned} \tag{2.64}$$

$$\begin{aligned} p_n =& p_{\text{atm}} + \rho g\left(\zeta - z\right) + \rho\frac{z^2-\eta_{n-1}^2}{2}\left(\frac{\partial Q_n}{\partial t} + \boldsymbol{u}_n.\nabla Q_n - Q_n^2\right) + \rho\left(z-\eta_{n-1}\right) \\ &\left(\frac{\partial R_n}{\partial t} + \boldsymbol{u}_n.\nabla R_n - R_n Q_n\right) + \rho\sum_{m=1}^{n-1}\left[\frac{\eta_m^2-\eta_{m-1}^2}{2}\left(\frac{\partial Q_m}{\partial t} + \boldsymbol{u}_m.\nabla Q_m - Q_m^2\right)\right. \\ &\left. + \left(\eta_m - \eta_{m-1}\right)\left(\frac{\partial R_m}{\partial t} + \boldsymbol{u}_m.\nabla R_m - R_m Q_m\right)\right] \end{aligned} \tag{2.65}$$

The continuity equation (2.58) reads in dimensional form:

$$\begin{aligned} &\frac{\partial \zeta}{\partial t} + \frac{\partial h}{\partial t} + \nabla.\sum_{n=1}^{N}\left(\eta_{n-1} - \eta_n\right)\left(\boldsymbol{u}_n - \frac{1}{6}\left(\eta_{n-1}^2 + \eta_{n-1}\eta_n + \eta_n^2 - 3\kappa_n^2\right)\nabla Q_n\right. \\ &\left. - \frac{1}{2}\left(\eta_{n-1} + \eta_n - 2\kappa_n\right)\nabla R_n\right) = 0 \end{aligned} \tag{2.66}$$

The momentum equation (2.59) within layer 1 reads in dimensional form:

$$\begin{aligned}
&\frac{\partial \boldsymbol{u}_1}{\partial t} + \boldsymbol{u}_1.\nabla\boldsymbol{u}_1 + g\nabla\zeta + \frac{1}{\rho}\nabla p_{\text{atm}} + \frac{\partial}{\partial t}\left(\frac{\kappa_1^2}{2}\nabla Q_1 + \kappa_1\nabla R_1\right) + \nabla\left(\frac{\kappa_1^2}{2}\boldsymbol{u}_1.\nabla Q_1\right) \\
&+ \nabla\left(\kappa_1\boldsymbol{u}_1.\nabla R_1\right) - \boldsymbol{u}_1 \times \left(\nabla \times \left(\frac{\kappa_1^2}{2}\nabla Q_1\right)\right) - \boldsymbol{u}_1 \times \left(\nabla \times \left(\kappa_1\nabla R_1\right)\right) \\
&+ \frac{z^2 - \kappa_1^2}{2}\nabla Q_1 \times \left(\nabla \times \boldsymbol{u}_1\right) + \left(z - \kappa_1\right)\nabla R_1 \times \left(\nabla \times \boldsymbol{u}_1\right) + \nabla\left(\frac{R_1^2}{2} - \zeta\frac{\partial R_1}{\partial t}\right) \\
&- \nabla\left(\zeta\boldsymbol{u}_1.\nabla R_1\right) + \nabla\left(\zeta R_1 Q_1 - \frac{\zeta^2}{2}\frac{\partial Q_1}{\partial t}\right) - \nabla\left(\frac{\zeta^2}{2}\boldsymbol{u}_1.\nabla Q_1\right) + \nabla\left(\frac{\zeta^2}{2}Q_1^2\right) = 0
\end{aligned} \tag{2.67}$$

Finally, the internal continuity condition (2.60) for $\boldsymbol{U}$ reads in dimensional form:

$$\begin{aligned}
&\boldsymbol{u}_n + \frac{\kappa_n^2 - \eta_{n-1}^2}{2}\nabla Q_n + \left(\kappa_n - \eta_{n-1}\right)\nabla R_n - \boldsymbol{u}_{n-1} \\
&- \frac{\kappa_{n-1}^2 - \eta_{n-1}^2}{2}\nabla Q_{n-1} - \left(\kappa_{n-1} - \eta_{n-1}\right)\nabla R_{n-1} = 0\,,\ 2 \leqslant n \leqslant N
\end{aligned} \tag{2.68}$$

2.3 Truncation error of the model

In this section, an estimation of the truncation error of the multi-layer first order dispersive model is presented from the heuristic analysis of Lynett (2002). According to equations (2.58), (2.59) and (2.60), the overall truncation error of the model can be expressed as

$$O\left(\mu_0^2\mu_1^2, \mu_1^4, \mu_2^4, ..., \mu_N^4\right) \tag{2.69}$$

Noting that $\mu_1^4 \leqslant \mu_0^2\mu_1^2$ since $d_1 \leqslant h_0$, this error is simplified to

$$O\left(\mu_0^2\mu_1^2, \mu_2^4, ..., \mu_N^4\right) \tag{2.70}$$

2.3.1 Heuristic approach

The truncation error is examined through an heuristic approach, by taking the error as a finite value instead of an order. This value is then utilised to estimate the accuracy of the model, in comparison to higher order Boussinesq type dispersive approximations.

The optimal exploitation of the multi-layer description of the water depth is achieved when the truncation error is minimal and occurs when $\mu_0^2\mu_1^2 = \mu_2^4 = ... = \mu_N^4$, that is to say when $d_1 h_0 = d_2^2 = ... = d_N^2$. Then, thicknesses d_n, $2 \leqslant n \leqslant N$ can be expressed in terms of d_1 as: $d_2 = ... = d_N = \sqrt{d_1 h_0}$, so that an equation for $\sqrt{d_1}$ is obtained from the relation $b_N = h_0$:

$$d_1 + \left(N - 1\right)\sqrt{h_0}\sqrt{d_1} - h_0 = 0 \tag{2.71}$$

The resolution of this second degree equation leads to two distinct real roots, and the inequality $d_1 \leqslant h_0$ allows the selection of the physical solution:

$$d_1 = \left(\frac{1 - N + \sqrt{\left(N-1\right)^2 + 4}}{2}\right)^2 h_0 \tag{2.72}$$

Finally, the heuristic truncation error can be expressed in function of N as follows:

$$O\left(\left(\frac{1-N+\sqrt{(N-1)^2+4}}{2}\right)^2\mu_0^4\right) \tag{2.73}$$

The truncation error of the model is shown in Figure 2.3 for up to five layers, and is compared to the error in $O(\mu_0^6)$ of the second order Boussinesq type model of Gobbi *et al.* (2000). As expected, the error decreases when the number of layers is raised. Besides, the curves of the first order multi-layer model and the second order model intersect each other at $\mu_{0\text{int}}$:

$$\mu_{0\text{int}} = \sqrt{\frac{d_1}{h_0}} = \frac{1-N+\sqrt{(N-1)^2+4}}{2} \tag{2.74}$$

It can be observed in Figure 2.3 that for $\mu_0 < \mu_{0\text{int}}$, the second order model error is lower than the multi-layer model error. However from $\mu_{0\text{int}}$, the multi-layer model becomes more accurate. In fact, compared to a one-layer model derived at any order $O\left(\mu_0^{2k}\right)$, even the two-layer model will achieve a better accuracy as μ_0 gets closer to 1.

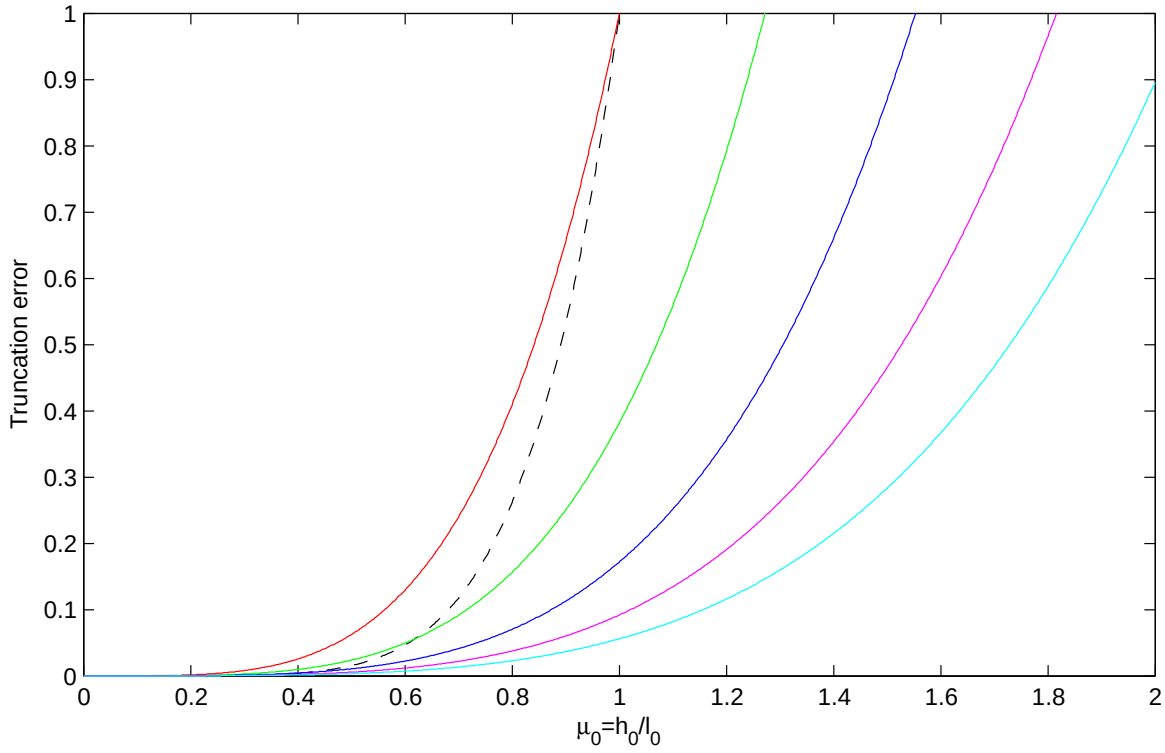

Figure 2.3: Truncation error of the multi-layer model, $N = 1$ (-), $N = 2$ (-), $N = 3$ (-), $N = 4$ (-) and $N = 5$ (-) versus the model of Gobbi *et al.* (2000) (- -)

2.3.2 Insignificance of intermediate order terms

At the time of evaluating the pressure p_n in subsection 2.2.2, the terms $O(\mu_0^2\mu_1^2)$ were neglected in the vertical momentum equation (2.53). This subsection explores the effect

the inclusion of these terms would have on the truncation error, which modifies to

$$O\left(\mu_0^2\mu_1^4, \mu_1^4, \mu_2^4, ..., \mu_N^4\right) \tag{2.75}$$

In this case, the two following situations are examined:

- $\mu_0 \leqslant 1 \Leftrightarrow \mu_0^2\mu_1^4 \leqslant \mu_1^4$, the error reduces to $O\left(\mu_1^4, \mu_2^4, ..., \mu_N^4\right)$ and reads

$$O\left(\frac{1}{N^2}\mu_0^4\right) \tag{2.76}$$

- $\mu_0 \geqslant 1 \Leftrightarrow \mu_1^4 \leqslant \mu_0^2\mu_1^4$, the error reduces to $O\left(\mu_0^2\mu_1^4, \mu_2^4, ..., \mu_N^4\right)$ and reads

$$O\left(\frac{1}{\left(1+(N-1)\,\mu_0\right)^2}\mu_0^6\right) \tag{2.77}$$

As a result, the addition of $O\left(\mu_0^2\mu_1^2\right)$ terms to the multi-layer model induces a reduction of the truncation error in Figure 2.4 for $\mu_0 \leqslant \mu_{0\text{int}2}$ (up to the intersection point of the curves):

$$\mu_{0\text{int}2} = \frac{\mu_{0\text{int}}^2\,(N-1) + \mu_{0\text{int}}}{1 - \mu_{0\text{int}}^2\,(N-1)^2} \tag{2.78}$$

Beyond this point, the error becomes increasingly greater and starts affecting the accuracy. Furthermore, the previous enhancement of accuracy is actually relatively weak compared to the additional complexity of governing equations, due to an implication of those terms, which would require the determination of the second component $W_n^{[1]}$ of the vertical velocity W_n.

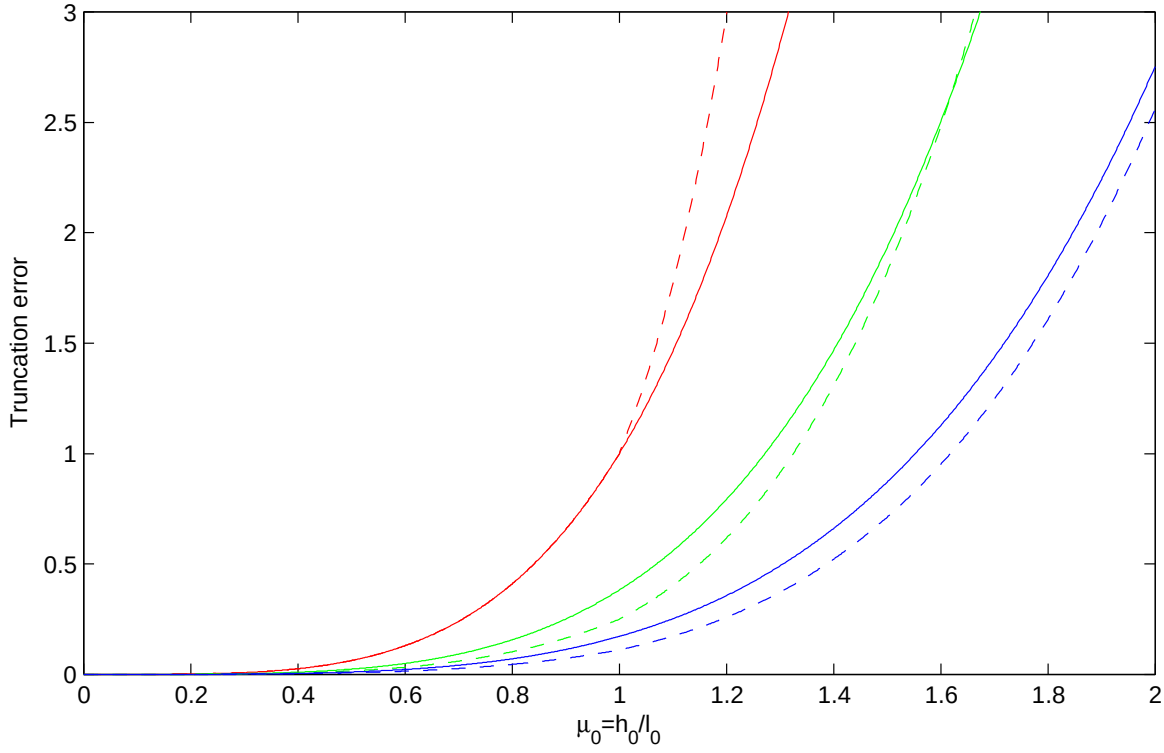

Figure 2.4: Effect of the inclusion of $O\left(\mu_0^2\mu_1^2\right)$ terms on the truncation error of the multi-layer model with the same colors as in Figure 2.3, model (-), modified model (- -)

2.3.3 Velocities in lower layers

The multi-layer model, derived in the previous section, does not explicitly solve the horizontal momentum equation within each layer, for the calculation of velocities $\boldsymbol{u}_n$. Basically, the momentum equation is solved in the superficial layer, while lower layer velocities are chosen to be determined by the internal velocity continuity condition at layer interfaces. The truncation error of an alternative model comprised of a system of N momentum equations is examined below. In such a case, this error would read $O\left(\mu_0^2\mu_1^2, ..., \mu_0^2\mu_N^2, \mu_1^4, ..., \mu_N^4\right)$ and reduce to $O\left(\mu_0^2\mu_1^2, ..., \mu_0^2\mu_N^2\right)$, which can be expressed in function of N as

$$O\left(\frac{1}{N}\mu_0^4\right) \tag{2.79}$$

This time, Figure 2.5 clearly shows an increase of the truncation error for the alternative model, which supports in some way the choice made for the calculation of velocities. Finally, we recall the great feature of the multi-layer approach and the ability of the model to control its own range of validity by only playing with the arbitrary number N of layers.

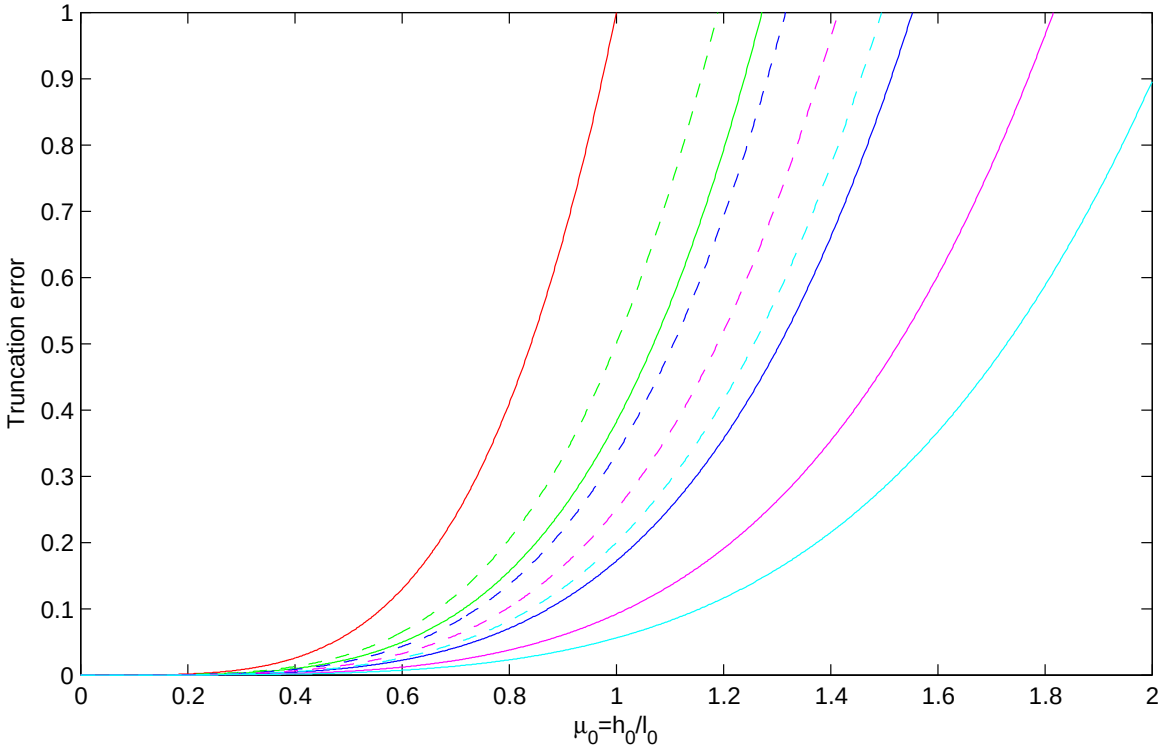

Figure 2.5: Effect of the alternative modelling on the truncation error of the multi-layer model with the same colors as in Figure 2.3, model (-), alternative model (- -)

2.4 Calibration of the model properties

As part of any Boussinesq type derivation, the intrinsic dispersion properties of the governing equations are generally optimised through a sort of calibration of the model to the known

theoretical properties of deep water waves, fully described by the analytical theory of Stokes (1847). In the case of an overall b^{th} order calibration, the arbitrary vertical location η_n of the layers and the respective internal depths κ_n to which horizontal velocities are numerically evaluated can be mathematically described from the suggestion of Lynett (2002) by

$$\begin{aligned} \eta_n &= \alpha_n h + \sum_{q=1}^{b-1} \beta_{nq} \frac{\zeta^q}{h^{q-1}} \,,\ 1 \leqslant n \leqslant N-1 \\ \kappa_n &= \gamma_n h + \sum_{q=1}^{b-1} \delta_{nq} \frac{\zeta^q}{h^{q-1}} \,,\ 1 \leqslant n \leqslant N \end{aligned} \tag{2.80}$$

Then, the user-defined coefficients are taken as calibration parameters: α_n and γ_n are used to optimise linear properties with a calibration of first order terms, while β_{nq} and δ_{nq} are used to optimise nonlinear properties with a calibration of higher order terms.

In the next two subsections, we discuss the main ideas of both linear and nonlinear analyses in the case of a second order calibration procedure, where the expressions of variables η_n and κ_n in (2.80) reduce to the approach of Kennedy *et al.* (2001):

$$\begin{aligned} \eta_n &= \alpha_n h + \beta_n \zeta \,,\ 1 \leqslant n \leqslant N-1 \\ \kappa_n &= \gamma_n h + \delta_n \zeta \,,\ 1 \leqslant n \leqslant N \end{aligned} \tag{2.81}$$

2.4.1 Linear optimisation

The phase speed, wave group velocity and linear shoaling gradient are generally examined so as to achieve optimal linear dispersion properties over a wide range of kh values. Basically, the analysis consists in making the model linear properties match at best the analytical theory of Airy (1845), or the theory of Stokes (1847) truncated to first order.

The linear phase celerity c is formally given by the linear dispersion relationship, which reads in the analytical theoretical case in its most common form:

$$\frac{c^2}{gh} = \frac{\tanh(kh)}{kh} \tag{2.82}$$

The linear dispersion relationship of the model can be obtained from a linearisation of the one-dimensional and constant water depth version of the governing equations (2.66), (2.67) and (2.68), and by substituting the first order term from the expansion of a Stokes (1847) type Fourier analysis as the assumed linear solution form, as follows:

$$(\zeta, u_n) = \left(\zeta^{(1)}, u_n^{(1)}\right) \mathrm{e}^{\mathrm{i}(kx-\sigma t)} \tag{2.83}$$

where $\sigma = kc$ is the angular wave frequency. Lynett and Liu (2004b) reported a linear dispersion relationship equivalent to a $[2N/2N]$ Padé approximant in kh (which could also be viewed as a $[N/N]$ Padé approximant in kh^2) of (2.82) for the N-layer model:

$$\frac{c^2}{gh} = \frac{1 + \sum_{n=1}^{N} N_n (kh)^{2n}}{1 + \sum_{n=1}^{N} D_n (kh)^{2n}} \tag{2.84}$$

where coefficients N_n and D_n are functions of α_n and γ_n.

The linear group velocity c_g is associated with the propagation of the wave energy or the wave envelope in irregular linear wave trains, and can be determined straightforwardly by taking the derivative of the dispersion relation: $c_g = \frac{d\sigma}{dk}$. In the analytical case, it reads

$$c_g = \frac{c}{2}\left(1 + \frac{2kh}{\sinh(2kh)}\right) \tag{2.85}$$

The linear group velocity of the model can then be easily calculated from (2.84).

The linear shoaling gradient A_x characterises the propagation of a linear wave train of amplitude a over a mildly sloping bottom h and is given by the linear shoaling equation:

$$\frac{a_x}{a} + A_x\frac{h_x}{h} = 0 \tag{2.86}$$

The analytical linear shoaling gradient can be determined from the concept of energy flux conservation $\frac{\partial}{\partial x}\left(a^2 c_g\right) = 0$ and the exact dispersion relationship (2.82) (see Madsen and Sørensen, 1992), so that after some algebraic manipulations it reads

$$A_x = \frac{G\left(1 + \frac{G}{2}\left[1 - \cosh(2kh)\right]\right)}{(1+G)^2},\ G = \frac{2kh}{\sinh(2kh)} \tag{2.87}$$

The linear shoaling gradient of the model can be calculated following the methodology described in Schäffer and Madsen (1995) and used by Lynett and Liu (2004a), for an assumed solution form of the linearised one-dimensional version of the governing equations (2.66), (2.67) and (2.68) and a truncation up to first derivative terms of the slowly varying quantities.

Finally, the linear optimisation of the model can be performed by adjusting the calibration parameters α_n and γ_n to a Padé approximation of the dispersion relationship, or through an overall error minimisation procedure of an average value built from the phase speed, group velocity and shoaling gradient errors, over a desired range of kh values.

In practice, in the case of one layer, the value $\gamma_1 = -0.53$ recommended by Nwogu (1993) can be used for an optimal elevation that minimises phase errors to 2% for $kh \in [0, \pi[$. For two, three and four layers, optimal sets of values issued from the error minimisation process are given in Lynett (2002) for an average of c, c_g and A_x errors, and in Lynett and Liu (2004b) for an average of only c and c_g errors as available numerical data.

2.4.2 Nonlinear optimisation

In the case of a second order calibration of the model, a nonlinear optimisation can be performed that makes the nonlinear dispersion properties of the model match the nonlinear second order terms of the analytical theory of Stokes (1847). The propagation of nonlinear second order Stokes steady waves and the analysis of nonlinear interactions of a linear first order Stokes bichromatic wave group are generally examined for the optimisation.

For the former case, the second order Stokes (1847) type Fourier expansion reads

$$(\zeta, u_n) = \epsilon \left(\zeta^{(1)}, u_n^{(1)}\right) \mathrm{e}^{\mathrm{i}(kx-\sigma t)} + \epsilon^2 \left(\zeta^{(2)}, u_n^{(2)}\right) \mathrm{e}^{2\mathrm{i}(kx-\sigma t)} \tag{2.88}$$

where ϵ is simply a small ordering parameter and the second order component of the solution of Stokes (1847) for the free surface elevation ζ is given by the following expression:

$$\zeta^{(2)} = \frac{k{\zeta^{(1)}}^2}{4} \frac{\cosh(kh)}{\sinh^3(kh)} (2 + \cosh(2kh)) = \frac{k{\zeta^{(1)}}^2}{4} \coth(kh) \left(3\coth^2(kh) - 1\right) \tag{2.89}$$

The nonlinear second order component of the model can then be calculated and expressed in terms of the remaining nonlinear coefficients β_n and δ_n, from the one-dimensional and constant water depth version of the governing equations (2.66), (2.67) and (2.68) and the second order Stokes (1847) type Fourier expansion (2.88) for the assumed solution form.

Second order nonlinear interactions of a linear first order Stokes (1847) bichromatic wave group can be analysed by considering the following two-wave group problem up to $O(\epsilon^2)$:

$$\begin{aligned}(\zeta, u_n) =& \epsilon \left(\zeta_1^{(1)}, u_{1n}^{(1)}\right) \mathrm{e}^{\mathrm{i}(k_1 x-\sigma_1 t)} + \epsilon \left(\zeta_2^{(1)}, u_{2n}^{(1)}\right) \mathrm{e}^{\mathrm{i}(k_2 x-\sigma_2 t)} + \epsilon^2 \left(\zeta_1^{(2)}, u_{1n}^{(2)}\right) \mathrm{e}^{2\mathrm{i}(k_1 x-\sigma_1 t)} \\ &+ \epsilon^2 \left(\zeta_2^{(2)}, u_{2n}^{(2)}\right) \mathrm{e}^{2\mathrm{i}(k_2 x-\sigma_2 t)} + \epsilon^2 \left(\zeta^+, u_n^+\right) \mathrm{e}^{\mathrm{i}(k_+ x-\sigma_+ t)} + \epsilon^2 \left(\zeta^-, u_n^-\right) \mathrm{e}^{\mathrm{i}(k_- x-\sigma_- t)}\end{aligned} \tag{2.90}$$

Where (ζ^+, u_n^+) and (ζ^-, u_n^-) are the resultant components of the sum and difference of the two first order wave frequencies $\sigma_\pm = \sigma_1 \pm \sigma_2$ and wavenumbers $k_\pm = k_1 \pm k_2$. Referred to as the super and subharmonic amplitudes respectively, the analytical free surface components $\zeta^\pm$ can be found in the second order wavemaker theory derivation by Schäffer (1996).

To find the super and subharmonic amplitudes of the model for the bichromatic interactions problem, the procedure is the same as for steady waves, substituting this time (2.90) for the assumed solution form into the one-dimensional and constant water depth equations.

Now, to close the calibration of the model with a second order general nonlinear optimisation, coefficients β_n and δ_n may be adjusted to minimise an overall error parameter including errors in the second order component of the free surface elevation and in the super and subharmonic amplitudes for up to a specific limit kh value (see Lynett, 2002 and Lynett and Liu, 2004a for minimisation based nonlinear optimisations of the two-layer model). An alternative method would be to restrict the optimisation procedure to only one case by making the model match some Taylor series about $kh = 0$ of the analytical components of the theory of Stokes (1847), and further analyse the effect of the calibration on the other case (see Kennedy *et al.*, 2001).

Chapter 3

Numerical approximation in 1D: MUOLDAO model

A brief description of the numerical implementation of the high order multi-layer Boussinesq type model is presented in this chapter. Basically, the governing equations are solved by a discontinuous Galerkin type method. In the following numerical approximation MUOLDAO (the Spanish abbreviation for Modelo Unidimensional de Ondas Largas Dispersivas de Alto Orden), we restrict our attention to one horizontal dimension x, so that both the horizontal velocity vector and horizontal nabla operator now simplify to $\boldsymbol{U}_n = U_n$ and $\nabla = \frac{\partial}{\partial x}$.

3.1 Resolution strategy

Before dealing with the numerical discretisation scheme, the somewhat crude dimensional governing equations (2.66), (2.67) and (2.68) are simplified to only one horizontal dimension x and a resolution strategy is proposed for the application of the discontinuous Galerkin (DG) method. Firstly, the auxiliary variables Q_n and R_n in (2.61) become

$$\begin{aligned} Q_n &= \frac{\partial u_n}{\partial x} \\ R_n &= \frac{\partial \left(h u_N\right)}{\partial x} + \frac{\partial h}{\partial t} + \sum_{m=n}^{N-1} \eta_m \left(Q_{m+1} - Q_m\right) \ , \ 1 \leqslant n \leqslant N-1 \\ R_N &= \frac{\partial \left(h u_N\right)}{\partial x} + \frac{\partial h}{\partial t} \end{aligned} \tag{3.1}$$

In the same way, the vertical profiles of velocities U_n and W_n in (2.62) and (2.63), and pressures p_1 and p_n, $n \geqslant 2$, in (2.64) and (2.65) are rewritten as follows:

$$U_n = u_n - \frac{z^2 - \kappa_n^2}{2} \frac{\partial Q_n}{\partial x} - \left(z - \kappa_n\right) \frac{\partial R_n}{\partial x} \tag{3.2}$$

$$W_n = -z Q_n - R_n \tag{3.3}$$

$$\begin{aligned} p_1 =& p_{\text{atm}} + \rho g\left(\zeta - z\right) + \rho\frac{z^2-\zeta^2}{2}\left(\frac{\partial Q_1}{\partial t} + u_1\frac{\partial Q_1}{\partial x} - Q_1^2\right) \\ &+ \rho\left(z-\zeta\right)\left(\frac{\partial R_1}{\partial t} + u_1\frac{\partial R_1}{\partial x} - R_1 Q_1\right) \end{aligned} \tag{3.4}$$

$$\begin{aligned} p_n =& p_{\text{atm}} + \rho g\left(\zeta - z\right) + \rho\frac{z^2-\eta_{n-1}^2}{2}\left(\frac{\partial Q_n}{\partial t} + u_n\frac{\partial Q_n}{\partial x} - Q_n^2\right) + \rho\left(z-\eta_{n-1}\right) \\ &\left(\frac{\partial R_n}{\partial t} + u_n\frac{\partial R_n}{\partial x} - R_n Q_n\right) + \rho\sum_{m=1}^{n-1}\left[\frac{\eta_m^2-\eta_{m-1}^2}{2}\left(\frac{\partial Q_m}{\partial t} + u_m\frac{\partial Q_m}{\partial x} - Q_m^2\right)\right. \\ &\left.+\left(\eta_m-\eta_{m-1}\right)\left(\frac{\partial R_m}{\partial t} + u_m\frac{\partial R_m}{\partial x} - R_m Q_m\right)\right] \end{aligned} \tag{3.5}$$

3.1.1 Systems of equations

For one horizontal dimension x, the governing equations (2.66), (2.67) and (2.68) reduce to

$$\begin{aligned} &\frac{\partial\zeta}{\partial t} + \frac{\partial h}{\partial t} + \frac{\partial}{\partial x}\sum_{n=1}^{N}\left(\eta_{n-1}-\eta_n\right)\left(u_n - \frac{1}{6}\left(\eta_{n-1}^2 + \eta_{n-1}\eta_n + \eta_n^2 - 3\kappa_n^2\right)\frac{\partial Q_n}{\partial x}\right. \\ &\left.-\frac{1}{2}\left(\eta_{n-1}+\eta_n-2\kappa_n\right)\frac{\partial R_n}{\partial x}\right) = 0 \end{aligned} \tag{3.6}$$

$$\begin{aligned} &\frac{\partial u_1}{\partial t} + \frac{1}{2}\frac{\partial u_1^2}{\partial x} + g\frac{\partial\zeta}{\partial x} + \frac{1}{\rho}\frac{\partial p_{\text{atm}}}{\partial x} + \frac{\partial}{\partial t}\left(\frac{\kappa_1^2}{2}\frac{\partial Q_1}{\partial x} + \kappa_1\frac{\partial R_1}{\partial x}\right) + \frac{\partial}{\partial x}\left(\frac{\kappa_1^2}{2}u_1\frac{\partial Q_1}{\partial x}\right) \\ &+ \frac{\partial}{\partial x}\left(\kappa_1 u_1\frac{\partial R_1}{\partial x}\right) + \frac{\partial}{\partial x}\left(\frac{R_1^2}{2} - \zeta\frac{\partial R_1}{\partial t}\right) - \frac{\partial}{\partial x}\left(\zeta u_1\frac{\partial R_1}{\partial x}\right) \\ &+ \frac{\partial}{\partial x}\left(\zeta R_1 Q_1 - \frac{\zeta^2}{2}\frac{\partial Q_1}{\partial t}\right) - \frac{\partial}{\partial x}\left(\frac{\zeta^2}{2}u_1\frac{\partial Q_1}{\partial x}\right) + \frac{\partial}{\partial x}\left(\frac{\zeta^2}{2}Q_1^2\right) = 0 \end{aligned} \tag{3.7}$$

$$\begin{aligned} &u_n + \frac{\kappa_n^2-\eta_{n-1}^2}{2}\frac{\partial Q_n}{\partial x} + \left(\kappa_n-\eta_{n-1}\right)\frac{\partial R_n}{\partial x} - u_{n-1} \\ &- \frac{\kappa_{n-1}^2-\eta_{n-1}^2}{2}\frac{\partial Q_{n-1}}{\partial x} - \left(\kappa_{n-1}-\eta_{n-1}\right)\frac{\partial R_{n-1}}{\partial x} = 0\,,\ 2\leqslant n\leqslant N \end{aligned} \tag{3.8}$$

It is underlined that rotational terms, and thereby the z-dependency, of the two-dimensional momentum equation (2.67) disappear in (3.7) in the case of only one horizontal dimension, so that this equation can be solved directly without being necessarily integrated over the upper layer 1. Gathering some hyperbolic terms, equation (3.7) simplifies to

$$\begin{aligned} &\frac{\partial u_1}{\partial t} + \frac{1}{2}\frac{\partial u_1^2}{\partial x} + g\frac{\partial\zeta}{\partial x} + \frac{1}{\rho}\frac{\partial p_{\text{atm}}}{\partial x} + \frac{\partial}{\partial t}\left(\frac{\kappa_1^2}{2}\frac{\partial Q_1}{\partial x} + \kappa_1\frac{\partial R_1}{\partial x}\right) \\ &+ \frac{\partial}{\partial x}\left(\frac{\kappa_1^2-\zeta^2}{2}u_1\frac{\partial Q_1}{\partial x}\right) + \frac{\partial}{\partial x}\left(\left(\kappa_1-\zeta\right)u_1\frac{\partial R_1}{\partial x}\right) \\ &+ \frac{1}{2}\frac{\partial}{\partial x}\left[\left(\zeta Q_1 + R_1\right)^2\right] - \frac{\partial}{\partial x}\left(\frac{\zeta^2}{2}\frac{\partial Q_1}{\partial t} + \zeta\frac{\partial R_1}{\partial t}\right) = 0 \end{aligned} \tag{3.9}$$

The last two terms of this equation can be reformulated using the relations

$$\begin{aligned}\frac{\partial}{\partial x}\left(\frac{\zeta^2}{2}\frac{\partial Q_1}{\partial t}\right) &= \frac{\partial}{\partial x}\left(\frac{\partial}{\partial t}\left(\frac{\zeta^2}{2}Q_1\right) - \zeta_t\zeta Q_1\right)\\ \frac{\partial}{\partial x}\left(\zeta\frac{\partial R_1}{\partial t}\right) &= \frac{\partial}{\partial x}\left(\frac{\partial}{\partial t}\left(\zeta R_1\right) - \zeta_t R_1\right)\end{aligned} \tag{3.10}$$

So that the momentum equation (3.9) is then rewritten in the following way:

$$\begin{aligned}&\frac{\partial u_1}{\partial t} + \frac{1}{2}\frac{\partial u_1^2}{\partial x} + g\frac{\partial \zeta}{\partial x} + \frac{1}{\rho}\frac{\partial p_{\text{atm}}}{\partial x} + \frac{\partial}{\partial t}\left(\frac{\kappa_1^2}{2}\frac{\partial Q_1}{\partial x} + \kappa_1\frac{\partial R_1}{\partial x} - \frac{\partial}{\partial x}\left(\frac{\zeta^2}{2}Q_1\right) - \frac{\partial}{\partial x}\left(\zeta R_1\right)\right)\\ &+ \frac{\partial}{\partial x}\left(\frac{\kappa_1^2-\zeta^2}{2}u_1\frac{\partial Q_1}{\partial x}\right) + \frac{\partial}{\partial x}\left(\left(\kappa_1-\zeta\right)u_1\frac{\partial R_1}{\partial x}\right) + \frac{\partial}{\partial x}\left(\frac{\left(\zeta Q_1 + R_1\right)^2}{2} + \zeta_t\left(\zeta Q_1 + R_1\right)\right) = 0\end{aligned} \tag{3.11}$$

Finally, the unidirectional model (3.6), (3.11) and (3.8) can be written in the form of two decoupled systems: a dispersive system whose unknowns are the free surface elevation ζ and the horizontal velocity u_1 in the superficial layer, and an elliptic system which allows the calculation of velocities u_n, $2 \leqslant n \leqslant N$, in lower layers.

Where $\boldsymbol{\mathcal{U}}_n = (\zeta, u_1, ..., u_n)^{\mathrm{T}}$, $1 \leqslant n \leqslant N$, the governing equations then read

Dispersive system

$$\frac{\partial \boldsymbol{\mathcal{U}}_1}{\partial t} + \frac{\partial \boldsymbol{\mathcal{D}}}{\partial t} + \frac{\partial \boldsymbol{\mathcal{F}}_{\text{d}}}{\partial x} = \boldsymbol{\mathcal{S}}_{\text{d}} \tag{3.12}$$

where the terms $\boldsymbol{\mathcal{U}}_1$, $\boldsymbol{\mathcal{D}}$, $\boldsymbol{\mathcal{F}}_{\text{d}}$ and $\boldsymbol{\mathcal{S}}_{\text{d}}$ are expressed as

$$\boldsymbol{\mathcal{U}}_1 = \begin{pmatrix}\zeta\\ u_1\end{pmatrix}, \quad \boldsymbol{\mathcal{D}} = \begin{pmatrix}0\\ \dfrac{\kappa_1^2}{2}\dfrac{\partial Q_1}{\partial x} + \kappa_1\dfrac{\partial R_1}{\partial x} - \dfrac{\partial}{\partial x}\left(\dfrac{\zeta^2}{2}Q_1\right) - \dfrac{\partial}{\partial x}\left(\zeta R_1\right)\end{pmatrix}, \quad \boldsymbol{\mathcal{S}}_{\text{d}} = \begin{pmatrix}-h_t\\ -\dfrac{1}{\rho}\dfrac{\partial p_{\text{atm}}}{\partial x}\end{pmatrix}$$

$$\boldsymbol{\mathcal{F}}_{\text{d}} = \begin{pmatrix}\displaystyle\sum_{n=1}^{N}\left(\eta_{n-1}-\eta_n\right)\left(u_n - \frac{1}{6}\left(\eta_{n-1}^2 + \eta_{n-1}\eta_n + \eta_n^2 - 3\kappa_n^2\right)\frac{\partial Q_n}{\partial x} - \frac{1}{2}\left(\eta_{n-1}+\eta_n-2\kappa_n\right)\frac{\partial R_n}{\partial x}\right)\\ \dfrac{u_1^2}{2} + g\zeta + \dfrac{\kappa_1^2-\zeta^2}{2}u_1\dfrac{\partial Q_1}{\partial x} + \left(\kappa_1-\zeta\right)u_1\dfrac{\partial R_1}{\partial x} + \dfrac{\left(\zeta Q_1 + R_1\right)^2}{2} + \zeta_t\left(\zeta Q_1 + R_1\right)\end{pmatrix} \tag{3.13}$$

Elliptic system

$$\begin{aligned}&u_n + \frac{\kappa_n^2-\eta_{n-1}^2}{2}\frac{\partial Q_n}{\partial x} + \left(\kappa_n-\eta_{n-1}\right)\frac{\partial R_n}{\partial x} - u_{n-1}\\ &- \frac{\kappa_{n-1}^2-\eta_{n-1}^2}{2}\frac{\partial Q_{n-1}}{\partial x} - \left(\kappa_{n-1}-\eta_{n-1}\right)\frac{\partial R_{n-1}}{\partial x} = 0\,,\ 2 \leqslant n \leqslant N\end{aligned} \tag{3.14}$$

3.1.2 Rearrangement of terms

With the aim of elaborating a resolution strategy, let us start focusing on the main difficulty of the previous system (3.12): the treatment of the time derivative of the dispersive term $\boldsymbol{\mathcal{D}}$. Then to simplify this equation, a substitution method is proposed with the definition of a temporal velocity variable $\widetilde{u}_1$ so the system can be rewritten in the following way:

$$\frac{\partial \widetilde{\boldsymbol{\mathcal{U}}}_1}{\partial t} + \frac{\partial \boldsymbol{\mathcal{F}}_{\mathrm{d}}}{\partial x} = \boldsymbol{\mathcal{S}}_{\mathrm{d}} \tag{3.15}$$

with $\widetilde{\boldsymbol{\mathcal{U}}}_1 = \boldsymbol{\mathcal{U}}_1 + \boldsymbol{\mathcal{D}} = (\zeta, \widetilde{u}_1)^{\mathrm{T}}$.

As a consequence, an additional equation is introduced in the elliptic system (3.14) for the estimation of the upper layer velocity u_1, in function of $\widetilde{u}_1$:

$$\begin{cases} u_1 + \dfrac{\kappa_1^2}{2}\dfrac{\partial Q_1}{\partial x} + \kappa_1 \dfrac{\partial R_1}{\partial x} - \dfrac{\partial}{\partial x}\left(\dfrac{\zeta^2}{2} Q_1\right) - \dfrac{\partial}{\partial x}\left(\zeta R_1\right) = \widetilde{u}_1 \\ u_n + \dfrac{\kappa_n^2 - \eta_{n-1}^2}{2}\dfrac{\partial Q_n}{\partial x} + \left(\kappa_n - \eta_{n-1}\right)\dfrac{\partial R_n}{\partial x} - u_{n-1} \\ -\dfrac{\kappa_{n-1}^2 - \eta_{n-1}^2}{2}\dfrac{\partial Q_{n-1}}{\partial x} - \left(\kappa_{n-1} - \eta_{n-1}\right)\dfrac{\partial R_{n-1}}{\partial x} = 0\,,\ 2 \leqslant n \leqslant N \end{cases} \tag{3.16}$$

By defining the vectors $\boldsymbol{\mathcal{U}} = (u_1, ..., u_N)^{\mathrm{T}}$, so that $\boldsymbol{\mathcal{U}}_N = (\zeta, \boldsymbol{\mathcal{U}})^{\mathrm{T}}$, and $\widetilde{\boldsymbol{\mathcal{U}}} = (\widetilde{u}_1, 0, ..., 0)^{\mathrm{T}}$, a substitution of the expressions of auxiliary variables Q_n and R_n given in (3.1) and their first spatial derivative into (3.16), leads to the following form for the elliptic system of size N:

$$(\mathcal{I}_{\mathrm{d}} + \mathcal{A})\boldsymbol{\mathcal{U}} + \mathcal{B}\frac{\partial \boldsymbol{\mathcal{U}}}{\partial x} + \mathcal{C}\frac{\partial^2 \boldsymbol{\mathcal{U}}}{\partial x^2} = \boldsymbol{\mathcal{S}}_{\mathrm{e}} + \widetilde{\boldsymbol{\mathcal{U}}} \tag{3.17}$$

where $\mathcal{I}_{\mathrm{d}}$ denotes the identity matrix. Moreover, the three squared matrices $\mathcal{A}$, $\mathcal{B}$ and $\mathcal{C}$ are a function of the free surface elevation ζ and its two first spatial derivatives ζ_x and ζ_{xx}, while the source term $\boldsymbol{\mathcal{S}}_{\mathrm{e}}$ only depends on ζ and ζ_x:

$$\mathcal{A} = \begin{pmatrix} 0 & & & & a_{1,N} \\ -1 & \ddots & & 0 & \vdots \\ & \ddots & \ddots & & a_{n,N} \\ 0 & & \ddots & 0 & \vdots \\ & & & -1 & a_{N,N} \end{pmatrix}, \quad \mathcal{B} = \begin{pmatrix} b_{1,1} & \cdots & & b_{1,n} & \cdots & & b_{1,N} \\ & \ddots & \ddots & \vdots & & & \vdots \\ & & b_{n,n-1} & b_{n,n} & \cdots & b_{n,l} & \cdots & b_{n,N} \\ & 0 & & & \ddots & \ddots & & \vdots \\ & & & & & & b_{N,N-1} & b_{N,N} \end{pmatrix}$$

$$\mathcal{C} = \begin{pmatrix} c_{1,1} & \cdots & & c_{1,n} & & \cdots & & c_{1,N} \\ & \ddots & \ddots & \vdots & & & & \vdots \\ & & & c_{n,n-1} & c_{n,n} & \cdots & c_{n,l} & \cdots & c_{n,N} \\ & & 0 & & & \ddots & \ddots & & \vdots \\ & & & & & & & c_{N,N-1} & c_{N,N} \end{pmatrix}, \quad \boldsymbol{\mathcal{S}}_{\mathrm{e}} = \begin{pmatrix} s_{\mathrm{e}1} \\ \vdots \\ s_{\mathrm{e}n} \\ \vdots \\ s_{\mathrm{e}N} \end{pmatrix} \tag{3.18}$$

The components of $\mathcal{A}$, $\mathcal{B}$, $\mathcal{C}$ and $\boldsymbol{\mathcal{S}}_{\mathrm{e}}$ are given respectively by

	$b_{1,1} = (\eta_1 - \zeta)\,\zeta_x - (\kappa_1 - \zeta)\,\eta_{1x}$ $b_{1,n} = (\kappa_1 - \zeta)\,(\eta_{n-1x} - \eta_{nx}) - \zeta_x\,(\eta_{n-1} - \eta_n)$ $b_{1,N} = -\,(h + \eta_{N-1})\,\zeta_x + (\kappa_1 - \zeta)\,(2h_x + \eta_{N-1x})$
$a_{1,N} = (\kappa_1 - \zeta)\,h_{xx} - \zeta_x h_x$ $a_{n,N} = (\kappa_n - \kappa_{n-1})\,h_{xx}$ $a_{N,N} = (\kappa_N - \kappa_{N-1})\,h_{xx}$	$b_{n,n-1} = (\kappa_{n-1} - \eta_{n-1})\,\eta_{n-1x}$ $b_{n,n} = -\,(\kappa_{n-1} - \eta_{n-1})\,\eta_{n-1x} - (\kappa_n - \kappa_{n-1})\,\eta_{nx}$ $b_{n,l} = (\kappa_n - \kappa_{n-1})\,(\eta_{l-1x} - \eta_{lx})$ $b_{n,N} = (\kappa_n - \kappa_{n-1})\,(2h_x + \eta_{N-1x})$ $b_{N,N-1} = (\kappa_{N-1} - \eta_{N-1})\,\eta_{N-1x}$ $b_{N,N} = 2h_x\,(\kappa_N - \kappa_{N-1}) - (\kappa_{N-1} - \eta_{N-1})\,\eta_{N-1x}$
$c_{1,1} = (\kappa_1 - \zeta)\left(\frac{\kappa_1 + \zeta}{2} - \eta_1\right)$ $c_{1,n} = (\kappa_1 - \zeta)\,(\eta_{n-1} - \eta_n)$ $c_{1,N} = (\kappa_1 - \zeta)\,(h + \eta_{N-1})$ $c_{n,n-1} = -\frac{1}{2}\,(\kappa_{n-1} - \eta_{n-1})^2$ $c_{n,n} = \frac{\kappa_n^2 + \eta_{n-1}^2}{2} - \kappa_{n-1}\eta_{n-1} - (\kappa_n - \kappa_{n-1})\,\eta_n$ $c_{n,l} = (\kappa_n - \kappa_{n-1})\,(\eta_{l-1} - \eta_l)$ $c_{n,N} = (\kappa_n - \kappa_{n-1})\,(h + \eta_{N-1})$ $c_{N,N-1} = -\frac{1}{2}\,(\kappa_{N-1} - \eta_{N-1})^2$ $c_{N,N} = \frac{\kappa_N^2 + \eta_{N-1}^2}{2} - \kappa_{N-1}\eta_{N-1} + h\,(\kappa_N - \kappa_{N-1})$	$s_{\mathrm{e}1} = -\,(\kappa_1 - \zeta)\,h_{tx} + \zeta_x h_t$ $s_{\mathrm{e}n} = -\,(\kappa_n - \kappa_{n-1})\,h_{tx}$ $s_{\mathrm{e}N} = -\,(\kappa_N - \kappa_{N-1})\,h_{tx}$

(3.19)

As a mathematical trick to solve the elliptic system, it is proposed to rearrange terms in (3.17) and add an extra physically nonsense time derivative term $\partial_\tau \boldsymbol{\mathcal{U}}$, so that a new parabolic system can be written for $\boldsymbol{\mathcal{U}}\,(x, \tau)$ (the time variable t is no more a variable here):

$$\tau_{\mathrm{e}} \frac{\partial \boldsymbol{\mathcal{U}}}{\partial \tau} + (\mathcal{I}_{\mathrm{d}} + \mathcal{D})\,\boldsymbol{\mathcal{U}} + \frac{\partial}{\partial x}\,(\mathcal{E}\boldsymbol{\mathcal{U}}) + \frac{\partial}{\partial x}\left(\mathcal{C}\frac{\partial \boldsymbol{\mathcal{U}}}{\partial x}\right) = \boldsymbol{\mathcal{S}}_{\mathrm{e}} + \widetilde{\boldsymbol{\mathcal{U}}} \tag{3.20}$$

where $\mathcal{D} = \mathcal{A} - \mathcal{B}_x + \mathcal{C}_{xx}$, $\mathcal{E} = \mathcal{B} - \mathcal{C}_x$ and τ_{e} is a time to keep the homogeneity of the equation. For simplicity, τ_{e} will be set to unity in numerical calculations: $\tau_{\mathrm{e}} = 1$ s.

Finally, the solution of the elliptic system (3.17) can now be easily obtained by calculating the steady state of the parabolised elliptic system (3.20), with a simple iterative method in time τ and a convergence criterion, since time accuracy there is unimportant.

3.2 Local Discontinuous Galerkin scheme in space

The finite volume (FV) spatial discretisation framework is proved to be much more adequate and efficient than finite differences (FD) in CFD, for their shock-capturing capacities treated by the use of Riemann solvers to deal with discontinuities between adjacent cells. In view of the computational efficiency of the one-dimensional Godunov type hybrid Boussinesq-SWE numerical model used by Borthwick *et al.* (2006) to study the transformation of solitary waves, the present investigation proposes to apply the discontinuous Galerkin (DG) method to solve the one-dimensional version of the multi-layer Boussinesq type model previously described in chapter 2. Basically, the DG method is a direct extension to higher order of the FV method, in a more general context than total variation diminishing monotone upstream-centered schemes for conservation laws (TVD-MUSCL) finite volume enhancement techniques, initially developed to raise the order of FV schemes. Actually, the DG method is preferred here to avoid combining both FV and FD methods, which might lead to some "dilution" of the general benefits of FV for the final scheme.

Introduced for the first time by Reed and Hill (1973), to study the neutron transport described by a steady state linear hyperbolic equation, the use of the DG method in numerical modelling has dramatically increased in the last thirty years. In a series of papers, Shu (1987, 1988) and Cockburn *et al.* (1989, 1990, 1998) developed a solid methodology to solve nonlinear hyperbolic conservation laws using explicit, nonlinearly stable high order Runge-Kutta time discretisations, coupled with a DG discretisation in space, and present a validation with the Euler equations of compressible gas dynamics. Another application of the method to the (in)compressible Navier-Stokes equations can be found in Cockburn and Shu (2001).

If widely adopted for (non)linear shallow water models, the DG framework is still poorly applied to Boussinesq type equations, due to the presence of the high order dispersive terms. Recently, Eskilsson and Sherwin (2005, 2006) and Eskilsson *et al.* (2006) presented some spectral, discontinuous Galerkin methods for the weakly nonlinear dispersive Boussinesq equations of Peregrine (1967) and the enhanced Boussinesq type equations of Madsen and Sørensen (1992): they compared various formulations for the treatment of the third order mixed derivatives and their results are very encouraging. Lately, Engsig-Karup *et al.* (2006, 2008) utilised a discontinuous Galerkin finite element method (DG-FEM) solver to get a numerical approximation of the equations presented by Madsen *et al.* (2002) and obtained excellent results in 1D and 2D respectively. In order to control mild nonlinear instabilities, their method introduced artificial damping in the scheme. The discretisation presented below has been implemented from scratch, and notably does not seem to require the incorporation of any de-aliasing method or filter to maintain numerical stability, which should yield some gain in CPU time and could represent a serious advantage for 2D problems, where such techniques can be numerically expensive and almost impractical (Engsig-Karup *et al.*, 2006).

3.2.1 Overview of the DG method

Basically, the DG method consists in approximating the solution by the numerical calculation of its local projection onto a polynomial basis, using a weak formulation of the equations,

written on each cell. Indeed, the DG scheme is a high order generalisation of the classic first order FV scheme which uses piecewise constant polynomials. The fundamental part of the DG method, when applied to solve partial differential equations (PDEs), is the adequate design of numerical fluxes at cell interfaces to deal with the allowed jumps of the solution, since each cell is treated separately. Naturally, the choice of these fluxes can be borrowed from the framework of FV methods, which is theoretically well-established (see LeVeque, 2002). Moreover, the DG method is flexible to *hp* adaptivity with a high parallel efficiency, thanks to the local structure of data communication between immediate neighbours, and can handle complicated geometry by the use of unstructured irregular grids for 2D problems.

To illustrate the essence of the method, the derivation of the DG scheme in the case of a simple one-dimensional scalar conservation law equation is presented below:

$$\frac{\partial u}{\partial t} + \frac{\partial f(u)}{\partial x} = 0\,,\ x \in [a,b] \tag{3.21}$$

Let the $M+1$ subdivisions $a = x_{1/2} < x_{3/2} < ... < x_{M+1/2} = b$ be an ordered partition of some interval $\mathrm{I} = [a,b] \subset \mathbb{R}$: the induced one-dimensional mesh is composed of M cells $\mathrm{I}_i = \left[x_{i-1/2}, x_{i+1/2}\right]$, of center $x_i = 0.5\left(x_{i-1/2} + x_{i+1/2}\right)$ and width $\Delta x_i = x_{i+1/2} - x_{i-1/2}$. By multiplying (3.21) by an arbitrary test function v and integrating by parts over I_i, the weak formulation of the equation is obtained with less regularity demanded for the solution:

$$\int_{\mathrm{I}_i} \frac{\partial u}{\partial t} v \,\mathrm{d}x - \int_{\mathrm{I}_i} f(u) \frac{\partial v}{\partial x} \,\mathrm{d}x + f\left(u_{i+1/2}\right) v_{i+1/2} - f\left(u_{i-1/2}\right) v_{i-1/2} = 0 \tag{3.22}$$

Henceforward, the solution u and the test function v are chosen to be piecewise polynomials of degree up to k, $k \geqslant 0$. By denoting $\mathbb{P}^k(\mathrm{I}_i)$ the space of polynomials of degree at most k in each cell I_i, the solution space of the weak problem (3.22) is given by $\mathbb{V}^k$:

$$\mathbb{V}^k = \left\{ v : v \in \mathbb{P}^k(\mathrm{I}_i) \text{ for } x \in \mathrm{I}_i\,,\ i = 1, ..., M \right\} \tag{3.23}$$

Actually, this choice produces a clear ambiguity in equation (3.22) for the last two terms involving the boundary values at $x_{i\pm1/2}$, as the solution u is discontinuous at these points. These terms must be designed appropriately to ensure the numerical stability of the method. By denoting $u^-_{i+1/2}$ and $u^+_{i+1/2}$ the values of u at $x_{i+1/2}$ from the left cell I_i and the right cell I_{i+1}, the boundary terms $f\left(u_{i\pm1/2}\right)$ are treated by the so-called numerical fluxes:

$$\widehat{f}_{i\pm1/2} = \widehat{f}\left(u^-_{i\pm1/2}, u^+_{i\pm1/2}\right) \tag{3.24}$$

In general, these fluxes depend on both limits at the left and right side of a cell interface, and are defined by taking information from the characteristics as an upwinding mechanism. For the equation (3.22), the numerical flux $\widehat{f}_{i\pm1/2}$ is taken from FV schemes as a two-point, Lipschitz continuous in both arguments, consistent with $\widehat{f}(u,u) = f(u)$ and monotone flux, i.e. non decreasing in the first argument and non increasing in the second one (e.g. the Godunov, Lax-Friedrichs, Roe fluxes, etc...). As for the test function v evaluated at boundary points $x_{i\pm1/2}$, values are taken within the cell I_i where it is defined, i.e. $v^+_{i-1/2}$ and $v^-_{i+1/2}$.

Finally, the numerical DG weak problem for the hyperbolic conservation law (3.22) can be formulated as follows: Find $u \in \mathbb{V}^k$, such that $\forall v \in \mathbb{V}^k$, we have for all cells I_i

$$\int_{\mathrm{I}_i} \frac{\partial u}{\partial t} v \, \mathrm{d}x - \int_{\mathrm{I}_i} f(u) \frac{\partial v}{\partial x} \, \mathrm{d}x + \widehat{f}_{i+1/2} v^-_{i+1/2} - \widehat{f}_{i-1/2} v^+_{i-1/2} = 0 \tag{3.25}$$

The discretisation scheme is then obtained by choosing a suitable basis of the space $\mathbb{P}^k(\mathrm{I}_i)$, and applying the weak formulation (3.25) to each element of this basis as the test function.

3.2.2 Discretisation of governing equations

Following the framework introduced in the previous subsection, the L^2-orthogonal basis of Legendre polynomials $(L_l)_{0 \leqslant l \leqslant k}$ is used in the present investigation to cover the local polynomial space $\mathbb{P}^k(\mathrm{I}_i)$ (Figure 3.1). After a convenient redefinition of these polynomials from $[-1, 1]$ to the cell I_i, the local approximation $\varphi_i(x,t)$ of some variable $\varphi(x,t)$ on I_i can be expressed as a linear combination of the new basis function elements $\widetilde{L}_l$:

$$\varphi_i(x,t) = \sum_{l=0}^{k} \varphi_i^l(t) \, \widetilde{L}_l(x) \tag{3.26}$$

where the $k+1$ unknown coefficients φ_i^l, related to the cell I_i, correspond to the degrees of freedom of the method, for which at least a suboptimal order of accuracy k can be expected for smooth solutions: see Cockburn and Shu (1998) and Xu and Shu (2007).

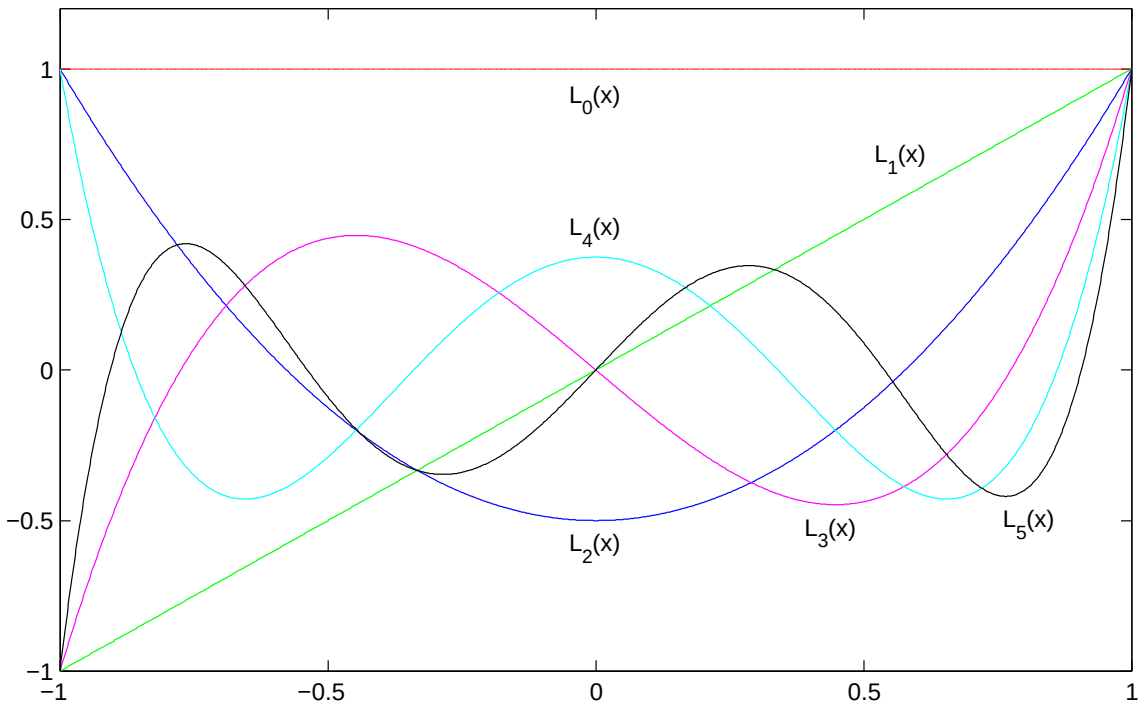

Figure 3.1: The first six elements of the Legendre polynomials family

Regarding now the further choice of numerical fluxes, a local Lax-Friedrichs flux will be employed for hyperbolic components, while for parabolic and dispersive terms the alternating fluxes methodology, summed up in Xu and Shu (2010), will be followed. The discretisation of both the dispersive (3.15) and parabolic (3.20) systems is presented below.

Dispersive system

In the previous dispersive system (3.15), auxiliary variables Q_n and R_n are developed to be able to separate convective, diffusive and dispersive parts of the flux. The resulting equation can then be expressed in the following way:

$$\frac{\partial \widetilde{\boldsymbol{\mathcal{U}}}_1}{\partial t} + \frac{\partial \boldsymbol{\mathcal{F}}_{\mathrm{dconv}}}{\partial x} + \frac{\partial \boldsymbol{\mathcal{F}}_{\mathrm{ddiff}}}{\partial x} + \frac{\partial \boldsymbol{\mathcal{F}}_{\mathrm{ddisp}}}{\partial x} + \frac{\partial \boldsymbol{\mathcal{F}}_{\mathrm{dbed}}}{\partial x} = \boldsymbol{\mathcal{S}}_{\mathrm{d}}\,,\ x \in [a,b]\ ,\ t>0 \tag{3.27}$$

where respective fluxes $\boldsymbol{\mathcal{F}}_{\mathrm{dconv}}$, $\boldsymbol{\mathcal{F}}_{\mathrm{ddiff}}$, $\boldsymbol{\mathcal{F}}_{\mathrm{ddisp}}$, $\boldsymbol{\mathcal{F}}_{\mathrm{dbed}}$ and the modified source term $\boldsymbol{\mathcal{S}}_{\mathrm{d}}$ read

$$\begin{aligned}
\boldsymbol{\mathcal{F}}_{\mathrm{dconv}} &= \begin{pmatrix} \displaystyle\sum_{n=1}^{N} (\eta_{n-1}-\eta_n)\, u_n - (h_{xx}u_N + h_{tx}) \sum_{n=1}^{N} b_n(\zeta) \\ \displaystyle\frac{1}{2}\left(u_1^2 + h_x^2 u_N^2\right) + g\zeta + d(\boldsymbol{\mathcal{U}}_1)(h_{xx}u_N + h_{tx}) + h_t h_x u_N \end{pmatrix} \\
\boldsymbol{\mathcal{F}}_{\mathrm{ddiff}} &= \begin{pmatrix} -2h_x \dfrac{\partial u_N}{\partial x} \displaystyle\sum_{n=1}^{N} b_n(\zeta) - \sum_{n=1}^{N-1} b_n(\zeta) \sum_{m=n}^{N-1} \eta_{mx} \left(\dfrac{\partial u_{m+1}}{\partial x} - \dfrac{\partial u_m}{\partial x}\right) \\ d(\boldsymbol{\mathcal{U}}_1)\left(2h_x \dfrac{\partial u_N}{\partial x} + \displaystyle\sum_{m=1}^{N-1} \eta_{mx}\left(\dfrac{\partial u_{m+1}}{\partial x} - \dfrac{\partial u_m}{\partial x}\right)\right) \\ + \left(\zeta_t + h_x u_N + h_t + \dfrac{1}{2}\displaystyle\sum_{m=1}^{N} (\eta_{m-1}-\eta_m)\dfrac{\partial u_m}{\partial x}\right) \displaystyle\sum_{m=1}^{N} (\eta_{m-1}-\eta_m)\dfrac{\partial u_m}{\partial x} \end{pmatrix} \\
\boldsymbol{\mathcal{F}}_{\mathrm{ddisp}} &= \begin{pmatrix} -h\dfrac{\partial^2 u_N}{\partial x^2} \displaystyle\sum_{n=1}^{N} b_n(\zeta) - \sum_{n=1}^{N} a_n(\zeta)\dfrac{\partial^2 u_n}{\partial x^2} - \sum_{n=1}^{N-1} b_n(\zeta) \sum_{m=n}^{N-1} \eta_m \left(\dfrac{\partial^2 u_{m+1}}{\partial x^2} - \dfrac{\partial^2 u_m}{\partial x^2}\right) \\ c(\boldsymbol{\mathcal{U}}_1)\dfrac{\partial^2 u_1}{\partial x^2} + d(\boldsymbol{\mathcal{U}}_1)\left(h\dfrac{\partial^2 u_N}{\partial x^2} + \displaystyle\sum_{m=1}^{N-1} \eta_m \left(\dfrac{\partial^2 u_{m+1}}{\partial x^2} - \dfrac{\partial^2 u_m}{\partial x^2}\right)\right) \end{pmatrix} \\
\boldsymbol{\mathcal{F}}_{\mathrm{dbed}} &= \begin{pmatrix} 0 \\ \zeta_t (h_x u_N + h_t) \end{pmatrix}, \quad \boldsymbol{\mathcal{S}}_{\mathrm{d}} = \begin{pmatrix} -h_t \\ -h_t h_{tx} - \dfrac{1}{\rho}\dfrac{\partial p_{\mathrm{atm}}}{\partial x} \end{pmatrix}
\end{aligned} \tag{3.28}$$

and coefficients $a_n(\zeta)$, $b_n(\zeta)$, $c(\boldsymbol{\mathcal{U}}_1)$ and $d(\boldsymbol{\mathcal{U}}_1)$ are given by

$$\begin{aligned}
a_n(\zeta) &= \frac{\eta_{n-1}^3 - \eta_n^3}{6} - \frac{\kappa_n^2(\eta_{n-1}-\eta_n)}{2}, \quad b_n(\zeta) = \frac{\eta_{n-1}^2 - \eta_n^2}{2} - \kappa_n(\eta_{n-1}-\eta_n) \\
c(\boldsymbol{\mathcal{U}}_1) &= \frac{\kappa_1^2 - \zeta^2}{2} u_1\,, \quad d(\boldsymbol{\mathcal{U}}_1) = (\kappa_1 - \zeta)\, u_1
\end{aligned} \tag{3.29}$$

The total flux is then recovered by the sum $\boldsymbol{\mathcal{F}}_{\mathrm{d}} = \boldsymbol{\mathcal{F}}_{\mathrm{dconv}} + \boldsymbol{\mathcal{F}}_{\mathrm{ddiff}} + \boldsymbol{\mathcal{F}}_{\mathrm{ddisp}} + \boldsymbol{\mathcal{F}}_{\mathrm{dbed}}$.

Owing to the presence of high order spatial derivatives, the local discontinuous Galerkin (LDG) method is defined by degenerating equation (3.27) to a first order system:

$$\begin{aligned}
&\frac{\partial \widetilde{\boldsymbol{\mathcal{U}}}_1}{\partial t} + \frac{\partial}{\partial x}\boldsymbol{\mathcal{F}}_{\mathrm{d}}\left(\boldsymbol{\mathcal{U}}_N, \boldsymbol{\mathcal{U}}'_N, \boldsymbol{\mathcal{U}}''\right) = \boldsymbol{\mathcal{S}}_{\mathrm{d}}\,,\ x \in [a,b]\ ,\ t>0 \\
&\boldsymbol{\mathcal{U}}''_N - \boldsymbol{\mathcal{U}}'_{Nx} = 0 \\
&\boldsymbol{\mathcal{U}}'_N - \boldsymbol{\mathcal{U}}_{Nx} = 0
\end{aligned} \tag{3.30}$$

The corresponding numerical weak formulation is obtained by multiplying the system (3.30) by the elements $\widetilde{L}_p$, $0 \leqslant p \leqslant k$, of the Legendre basis of the space $\mathbb{P}^k(\mathrm{I}_i)$ as test functions, integrating over the cell I_i and finally performing an integration by parts: $\forall\ 0 \leqslant p \leqslant k$,

$$\begin{aligned}
&\int_{\mathrm{I}_i} \frac{\partial \widetilde{\boldsymbol{\mathcal{U}}}_1}{\partial t}\widetilde{L}_p(x)\ \mathrm{d}x - \int_{\mathrm{I}_i} \widetilde{L}'_p(x)\,\boldsymbol{\mathcal{F}}_{\mathrm{d}}\ \mathrm{d}x + \widehat{\boldsymbol{\mathcal{F}}}_{\mathrm{d}i+1/2}\widetilde{L}_p\left(x_{i+1/2}\right) - \widehat{\boldsymbol{\mathcal{F}}}_{\mathrm{d}i-1/2}\widetilde{L}_p\left(x_{i-1/2}\right) = \int_{\mathrm{I}_i} \boldsymbol{\mathcal{S}}_{\mathrm{d}}\widetilde{L}_p(x)\ \mathrm{d}x \\
&\int_{\mathrm{I}_i} \boldsymbol{\mathcal{U}}''_N\widetilde{L}_p(x)\ \mathrm{d}x + \int_{\mathrm{I}_i} \widetilde{L}'_p(x)\boldsymbol{\mathcal{U}}'_N\ \mathrm{d}x - \widehat{\boldsymbol{\mathcal{U}}'_N}_{i+1/2}\widetilde{L}_p\left(x_{i+1/2}\right) + \widehat{\boldsymbol{\mathcal{U}}'_N}_{i-1/2}\widetilde{L}_p\left(x_{i-1/2}\right) = 0 \\
&\int_{\mathrm{I}_i} \boldsymbol{\mathcal{U}}'_N\widetilde{L}_p(x)\ \mathrm{d}x + \int_{\mathrm{I}_i} \widetilde{L}'_p(x)\boldsymbol{\mathcal{U}}_N\ \mathrm{d}x - \widehat{\boldsymbol{\mathcal{U}}_N}_{i+1/2}\widetilde{L}_p\left(x_{i+1/2}\right) + \widehat{\boldsymbol{\mathcal{U}}_N}_{i-1/2}\widetilde{L}_p\left(x_{i-1/2}\right) = 0
\end{aligned} \tag{3.31}$$

where variables with the hat sign are the numerical fluxes, evaluated at cell interfaces $x_{i\pm1/2}$. Using the local expansion of variables (3.26) and the orthogonality property of Legendre polynomials, the LDG scheme of the dispersive system finally reads: $\forall\ 0 \leqslant p \leqslant k$,

$$\begin{aligned}
&\frac{\Delta x}{2p+1}\frac{\mathrm{d}\widetilde{\boldsymbol{\mathcal{U}}}^p_{1i}}{\mathrm{d}t} - \int_{\mathrm{I}_i} \widetilde{L}'_p(x)\,\boldsymbol{\mathcal{F}}_{\mathrm{d}}\ \mathrm{d}x + \widehat{\boldsymbol{\mathcal{F}}}_{\mathrm{d}i+1/2} - (-1)^p\,\widehat{\boldsymbol{\mathcal{F}}}_{\mathrm{d}i-1/2} = \int_{\mathrm{I}_i} \boldsymbol{\mathcal{S}}_{\mathrm{d}}\widetilde{L}_p(x)\ \mathrm{d}x \\
&\frac{\Delta x}{2p+1}\boldsymbol{\mathcal{U}}''^p_{Ni} + \int_{\mathrm{I}_i} \widetilde{L}'_p(x)\boldsymbol{\mathcal{U}}'_N\ \mathrm{d}x - \widehat{\boldsymbol{\mathcal{U}}'_N}_{i+1/2} + (-1)^p\,\widehat{\boldsymbol{\mathcal{U}}'_N}_{i-1/2} = 0 \\
&\frac{\Delta x}{2p+1}\boldsymbol{\mathcal{U}}'^p_{Ni} + \int_{\mathrm{I}_i} \widetilde{L}'_p(x)\boldsymbol{\mathcal{U}}_N\ \mathrm{d}x - \widehat{\boldsymbol{\mathcal{U}}_N}_{i+1/2} + (-1)^p\,\widehat{\boldsymbol{\mathcal{U}}_N}_{i-1/2} = 0
\end{aligned} \tag{3.32}$$

The main flux is treated separately according to the order of spatial derivatives:

$$\widehat{\boldsymbol{\mathcal{F}}}_{\mathrm{d}} = \widehat{\boldsymbol{\mathcal{F}}}_{\mathrm{dconv}} + \widehat{\boldsymbol{\mathcal{F}}}_{\mathrm{ddiff}} + \widehat{\boldsymbol{\mathcal{F}}}_{\mathrm{ddisp}} + \widehat{\boldsymbol{\mathcal{F}}}_{\mathrm{dbed}} \tag{3.33}$$

For the convective term, the two-point Lipschitz continuous, consistent and monotone local Lax-Friedrichs flux is chosen here as it is relatively efficient and easy to implement:

$$\widehat{\boldsymbol{\mathcal{F}}}_{\mathrm{dconv}} = \frac{1}{2}\left[\boldsymbol{\mathcal{F}}_{\mathrm{d}^-_{\mathrm{conv}}} + \boldsymbol{\mathcal{F}}_{\mathrm{d}^+_{\mathrm{conv}}} - \vartheta_{\mathrm{d}}\left(\boldsymbol{\mathcal{U}}_1^+ - \boldsymbol{\mathcal{U}}_1^-\right)\right] \tag{3.34}$$

where - and + appendages refer to values at the left and right sides of the interfaces between adjacent cells, and ϑ_{d} is given by the eigenvalues $\lambda_{\mathrm{d}j}$ of the jacobian matrix $\boldsymbol{\mathcal{F}}'_{\mathrm{dconv}}(\boldsymbol{\mathcal{U}}_1)$:

$$\vartheta_{\mathrm{d}} = \max_{1\leqslant j\leqslant 2}\left(\left|\lambda^-_{\mathrm{d}j}\right|, \left|\lambda^+_{\mathrm{d}j}\right|\right) \tag{3.35}$$

In order to ensure the numerical stability of the scheme, the higher order fluxes can be chosen according to some rules, as recalled by Xu and Shu (2010): basically, upwinding is considered for odd derivatives which correspond to waves, while a symmetric treatment, such as an alternating choice of the fluxes for a quantity and its derivative, is used for even derivatives. The alternating fluxes methodology is described in Yan and Shu (2002). In that way, diffusive and dispersive components of the total flux in (3.33) can be simply given by

$$\begin{aligned} &\widehat{\boldsymbol{\mathcal{F}}}_{\mathrm{ddiff}}\left(\boldsymbol{\mathcal{U}}_N'^{+}\right) \ , \ \widehat{\boldsymbol{\mathcal{F}}}_{\mathrm{ddisp}}\left(\boldsymbol{\mathcal{U}}''^{+}\right) \\ &\widehat{\boldsymbol{\mathcal{U}}_N'} \text{ upwind} \\ &\widehat{\boldsymbol{\mathcal{U}}_N} = \boldsymbol{\mathcal{U}}_N^{-} \end{aligned} \tag{3.36}$$

So that for instance, by denoting $\boldsymbol{\mathcal{F}}_{\mathrm{ddisp}} = \left(\mathcal{F}_{\mathrm{ddisp1}}, \mathcal{F}_{\mathrm{ddisp2}}\right)^{\mathrm{T}}$, the first component of the dispersive flux can be expressed as the scalar product $\mathcal{F}_{\mathrm{ddisp1}} = \boldsymbol{f}\left(\zeta\right).\boldsymbol{\mathcal{U}}''$ of the form:

$$\mathcal{F}_{\mathrm{ddisp1}} = \sum_{n=1}^{N} f_n\left(\zeta\right) \mathcal{U}_n'' \, , \tag{3.37}$$

and the corresponding numerical flux is obtained as follows:

$$\widehat{\mathcal{F}}_{\mathrm{ddisp1}} = \sum_{n=1}^{N} \widehat{f_n\left(\zeta\right)\mathcal{U}_n''} = \sum_{n=1}^{N} \frac{F_n\left(\zeta^{+}\right) - F_n\left(\zeta^{-}\right)}{\zeta^{+} - \zeta^{-}} \mathcal{U}_n''^{+} \tag{3.38}$$

where F_n is a primitive function of f_n. The choice of fluxes is not unique here: in fact, the crucial part is taking $\widehat{\boldsymbol{\mathcal{U}}_N}$ and $\widehat{\boldsymbol{\mathcal{F}}}_{\mathrm{ddiff}}\left(\boldsymbol{\mathcal{U}}_N'\right)$, $\widehat{\boldsymbol{\mathcal{F}}}_{\mathrm{ddisp}}\left(\boldsymbol{\mathcal{U}}''\right)$ from opposite sides.

Regarding the isolated numerical flux $\boldsymbol{\mathcal{F}}_{\mathrm{dbed}}$, an empirical design of the second component $\mathcal{F}_{\mathrm{dbed2}}$ was shown to maintain the stability of the scheme and is adopted here:

$$\mathcal{F}_{\mathrm{dbed2}} = \frac{\zeta_t^{-} + \zeta_t^{+}}{2} \left(h_x \frac{u_N^{-} + u_N^{+}}{2} + h_t \right) \tag{3.39}$$

Integrals in the LDG scheme (3.32) of the dispersive system are replaced by a Gauss-Legendre quadrature rule of order $2k+1$, using the $k+1$ zeros of the polynomial $\widetilde{L}_{k+1}$ as the quadrature nodes (see the next subsection 3.2.3). At this point, it is important to note that the global order k of the approximation is maintained for the two first spatial derivatives $\boldsymbol{\mathcal{U}}_N'$ and $\boldsymbol{\mathcal{U}}_N''$, of the solution $\boldsymbol{\mathcal{U}}_N$. Furthermore, the time derivative of the free surface elevation in the second component of the dispersive system is present, which is determined by the first component. Therefore, it is necessary to solve these components separately.

Basically, a set of $k+1$ subsystems of ordinary differential equations (ODEs) is obtained from (3.32) for each cell, which in a more compact form would result in the general system

$$\frac{\mathrm{d}\widetilde{\boldsymbol{\mathfrak{U}}}_1}{\mathrm{d}t} = \boldsymbol{\mathfrak{L}}_{\mathrm{d}}\left(t, \boldsymbol{\mathfrak{U}}_N, \boldsymbol{\mathfrak{U}}_N', \boldsymbol{\mathfrak{U}}''\right) \tag{3.40}$$

where $\widetilde{\boldsymbol{\mathfrak{U}}}_1$ contains the degrees of freedom $\widetilde{\boldsymbol{\mathcal{U}}}_{1i}^{p}$, $0 \leqslant p \leqslant k$, of each cell I_i, $1 \leqslant i \leqslant M$:

$$\widetilde{\boldsymbol{\mathfrak{U}}}_1 = \left(..., \widetilde{\boldsymbol{\mathcal{U}}}_{1i}^{0}, ..., \widetilde{\boldsymbol{\mathcal{U}}}_{1i}^{p}, ..., \widetilde{\boldsymbol{\mathcal{U}}}_{1i}^{k}, ... \right)^{\mathrm{T}} \tag{3.41}$$

Parabolised elliptic system

The LDG numerical discretisation of the parabolised elliptic system is very similar to that of the dispersive system. The identification of the convective $\boldsymbol{\mathcal{F}}_{\mathrm{econv}} = \boldsymbol{\mathcal{E}}\boldsymbol{\mathcal{U}}$ and diffusive $\boldsymbol{\mathcal{F}}_{\mathrm{ediff}} = \boldsymbol{\mathcal{C}}\boldsymbol{\mathcal{U}}_x$ parts of the flux in (3.20) leads to the following equation:

$$\tau_{\mathrm{e}}\frac{\partial \boldsymbol{\mathcal{U}}}{\partial \tau} + (\mathcal{I}_{\mathrm{d}} + \mathcal{D})\boldsymbol{\mathcal{U}} + \frac{\partial \boldsymbol{\mathcal{F}}_{\mathrm{econv}}}{\partial x} + \frac{\partial \boldsymbol{\mathcal{F}}_{\mathrm{ediff}}}{\partial x} = \boldsymbol{\mathcal{S}}_{\mathrm{e}} + \widetilde{\boldsymbol{\mathcal{U}}}\,,\ x \in [a,b]\ ,\ \tau > 0 \tag{3.42}$$

The degeneration of equation (3.42) to a first order system reads

$$\begin{aligned} &\tau_{\mathrm{e}}\frac{\partial \boldsymbol{\mathcal{U}}}{\partial \tau} + (\mathcal{I}_{\mathrm{d}} + \mathcal{D})\boldsymbol{\mathcal{U}} + \frac{\partial}{\partial x}\boldsymbol{\mathcal{F}}_{\mathrm{e}}\left(\boldsymbol{\mathcal{U}}, \boldsymbol{\mathcal{U}}'\right) = \boldsymbol{\mathcal{S}}_{\mathrm{e}} + \widetilde{\boldsymbol{\mathcal{U}}}\,,\ x \in [a,b]\ ,\ \tau > 0 \\ &\boldsymbol{\mathcal{U}}' - \boldsymbol{\mathcal{U}}_x = 0 \end{aligned} \tag{3.43}$$

where the total flux corresponds to the sum $\boldsymbol{\mathcal{F}}_{\mathrm{e}} = \boldsymbol{\mathcal{F}}_{\mathrm{econv}} + \boldsymbol{\mathcal{F}}_{\mathrm{ediff}}$.

The LDG scheme of the parabolised elliptic system is then given by: $\forall\ 0 \leqslant p \leqslant k$,

$$\begin{aligned} &\frac{\Delta x}{2p+1}\left(\tau_{\mathrm{e}}\frac{\mathrm{d}\boldsymbol{\mathcal{U}}_i^p}{\mathrm{d}\tau} + \boldsymbol{\mathcal{U}}_i^p\right) + \int_{\mathrm{I}_i} \mathcal{D}\boldsymbol{\mathcal{U}}\widetilde{L}_p(x)\ \mathrm{d}x - \int_{\mathrm{I}_i} \widetilde{L}'_p(x)\,\boldsymbol{\mathcal{F}}_{\mathrm{e}}\,\mathrm{d}x + \widehat{\boldsymbol{\mathcal{F}}}_{\mathrm{e}i+1/2} \\ &-(-1)^p\,\widehat{\boldsymbol{\mathcal{F}}}_{\mathrm{e}i-1/2} = \int_{\mathrm{I}_i} \boldsymbol{\mathcal{S}}_{\mathrm{e}}\widetilde{L}_p(x)\ \mathrm{d}x + \frac{\Delta x}{2p+1}\widetilde{\boldsymbol{\mathcal{U}}}_i^p \\ &\frac{\Delta x}{2p+1}\boldsymbol{\mathcal{U}}_i'^p + \int_{\mathrm{I}_i} \widetilde{L}'_p(x)\boldsymbol{\mathcal{U}}\,\mathrm{d}x - \widehat{\boldsymbol{\mathcal{U}}}_{i+1/2} + (-1)^p\widehat{\boldsymbol{\mathcal{U}}}_{i-1/2} = 0 \end{aligned} \tag{3.44}$$

with the total numerical flux calculated separately according to the nature of the terms:

$$\widehat{\boldsymbol{\mathcal{F}}}_{\mathrm{e}} = \widehat{\boldsymbol{\mathcal{F}}}_{\mathrm{econv}} + \widehat{\boldsymbol{\mathcal{F}}}_{\mathrm{ediff}} \tag{3.45}$$

The convective part is again evaluated using the local Lax-Friedrichs flux:

$$\widehat{\boldsymbol{\mathcal{F}}}_{\mathrm{econv}} = \frac{1}{2}\left[\boldsymbol{\mathcal{F}}^-_{\mathrm{econv}} + \boldsymbol{\mathcal{F}}^+_{\mathrm{econv}} - \vartheta_{\mathrm{e}}\left(\boldsymbol{\mathcal{U}}^+ - \boldsymbol{\mathcal{U}}^-\right)\right] \tag{3.46}$$

with ϑ_{e} given this time by the eigenvalues λ_{en} of the matrix $\mathcal{E}$:

$$\vartheta_{\mathrm{e}} = \max_{1\leqslant n\leqslant N}\left(\left|\lambda^-_{en}\right|, \left|\lambda^+_{en}\right|\right) \tag{3.47}$$

and the same alternating flux methodology is followed for the diffusive term:

$$\begin{aligned} &\widehat{\boldsymbol{\mathcal{F}}}_{\mathrm{ediff}}\left(\boldsymbol{\mathcal{U}}'^+\right) \\ &\widehat{\boldsymbol{\mathcal{U}}} = \boldsymbol{\mathcal{U}}^- \end{aligned} \tag{3.48}$$

The ODE system resulting from equation (3.44) can be written in this way:

$$\frac{\mathrm{d}\mathfrak{U}}{\mathrm{d}\tau} = \mathfrak{L}_{\mathrm{e}}\left(\mathfrak{U}, \mathfrak{U}'\right) \tag{3.49}$$

with

$$\mathfrak{U} = \left(..., \boldsymbol{\mathcal{U}}_i^0, ..., \boldsymbol{\mathcal{U}}_i^p, ..., \boldsymbol{\mathcal{U}}_i^k, ...\right)^{\mathrm{T}} \tag{3.50}$$

Remaining integrals in (3.44) are approximated in a similar way to the dispersive system, by means of the same Gauss-Legendre quadrature rule. To get the desired steady state solution, the latter system, defined in (3.49), is finally iterated in time through the use of the following explicit Euler forward scheme until a suitable convergence criterion is satisfied:

$$\begin{aligned} &\mathfrak{U}^{(0)} = \mathfrak{U}^n \\ &\mathfrak{U}^{(m+1)} = \mathfrak{U}^{(m)} + \Delta\tau \mathfrak{L}_{\mathrm{e}} \left(\mathfrak{U}^{(m)}, \mathfrak{U}'^{(m)}\right) \\ &\mathfrak{U}^{n+1} = \mathfrak{U}^{(+\infty)} \end{aligned} \tag{3.51}$$

3.2.3 Gauss-Legendre quadrature

As previously mentioned for the LDG discretisation of both the dispersive and the parabolised elliptic systems, remaining integrals in numerical schemes (3.32) and (3.44) can be evaluated by means of quadrature rules, selected to an adequate order. To be consistent with a $\mathbb{P}^k$-based method, a quadrature rule of order $2k+1$ is required (Cockburn and Shu, 1989).

Given a family of orthogonal polynomials $(p_l)_{0 \leqslant l \leqslant +\infty}$ and the corresponding non negative integrable weight function w, we recall the following Gauss integration theorem. *Let* $(\alpha_l)_{0 \leqslant l \leqslant k}$ *denote the* $k+1$ *zeros of the polynomial* p_{k+1}*, belonging to the orthogonal family and located in the open interval* $]-1, 1[$ *with* $\alpha_0 < ... < \alpha_k$*. It exists* $k+1$ *positive constants* $\lambda_0, ..., \lambda_k$ *such that the following relationship holds for all polynomials up to degree* $2k+1$:

$$\int_{-1}^{1} w(x) f(x) \, \mathrm{d}x = \sum_{l=0}^{k} \lambda_l f(\alpha_l) \ , \ \forall f \in \mathbb{P}^{2k+1} \tag{3.52}$$

For polynomials with a degree larger than $2k+1$ or non polynomial functions, the Gauss integration scheme (3.52) with $k+1$ nodes yields an approximate value of $\int_{-1}^{1} w(x) f(x) \, \mathrm{d}x$ with an error, the leading term of which is proportional to $f^{(2k+2)}(\alpha)$, with $-1 < \alpha < 1$. The quantities $(\alpha_l)_{0 \leqslant l \leqslant k}$ and $(\lambda_l)_{0 \leqslant l \leqslant k}$ are known as the Gauss integration nodes and weights.

In the particular case of the Legendre polynomials family $(L_l)_{0 \leqslant l \leqslant +\infty}$, the weight function is $w(x) = 1$ and the Gauss-Legendre integration scheme of order $2k+1$ reads for any $g \in \mathrm{L}^2(\mathrm{I})$:

$$\begin{aligned} &\int_{-1}^{1} g(x) \, \mathrm{d}x \approx \sum_{l=0}^{k} \lambda_l g(\alpha_l) \\ &\alpha_l \ : \ \text{zeros of } L_{k+1} \, , \ 0 \leqslant l \leqslant k \\ &\lambda_l = \frac{2}{(1-\alpha_l^2) \, L_{k+1}'^2(\alpha_l)} \, , \ 0 \leqslant l \leqslant k \end{aligned} \tag{3.53}$$

3.2.4 Boundary conditions

To perform feasible numerical simulations, it is important to be able to confine the infinite region of interest $\mathbb{R}$ into the relatively small finite domain $\mathrm{I} \subset \mathbb{R}$ bounded by some boundary a and b. This can be done by imposing outer boundary conditions at these domain boundaries. Besides, the design of such conditions is fundamental for the numerical stability of a confined simulation. Up to now, three kinds of boundary conditions are implemented into the code: a wave inlet condition for the left border, a fully reflective rigid wall type closed condition for both borders, and a set of periodic conditions to connect the borders.

Given the left $x_{1/2}$ and right $x_{M+1/2}$ borders of the calculation domain, the outer values $\varphi^-_{1/2}$ and $\varphi^+_{M+1/2}$ of some variable $\varphi = \zeta, \zeta_x, \zeta_t, u_1, u_{1x}, u_{1xx}$ can be defined as follows for the calculation of numerical fluxes, according to the nature of the boundary condition desired:

- Inlet left boundary condition: $\varphi^-_{1/2} = \varphi\left(x_{1/2}\right)\ \forall\varphi$, i.e. the explicit expressions of the wave theory to be propagated are evaluated at the left border of the domain;
- Closed boundary conditions: at the right border $\varphi^+_{M+1/2} = \varphi^-_{M+1/2}$ for $\varphi = \zeta, \zeta_t, u_{1x}$ and $\varphi^+_{M+1/2} = -\varphi^-_{M+1/2}$ for $\varphi = \zeta_x, u_1, u_{1xx}$ (the condition is similar at the left border);
- Periodic boundary conditions: $\varphi^-_{1/2} = \varphi^-_{M+1/2}$ and $\varphi^+_{M+1/2} = \varphi^+_{1/2}\ \forall\varphi$.

Actually, the closed boundary condition at the right border $x_{M+1/2} = b$ is designed by first considering the classic mirror analogy, i.e. by setting $\zeta^+ = \zeta^-$, $\zeta^+_t = \zeta^-_t$ and $u^+_1 = -u^-_1$. Then, to find the somewhat less intuitive conditions for the spatial derivatives of ζ and u_1, it only depends on the assumed symmetry or antisymmetry of the variable at b:

$$\begin{aligned} &\text{symmetry}: \quad \varphi(b+x) = \varphi(b-x) \\ &\text{antisymmetry}: \quad \varphi(b+x) = -\varphi(b-x) \end{aligned} \tag{3.54}$$

So that for a symmetric ζ and an antisymmetric u_1, the corresponding boundary conditions for ζ_x, u_{1x} and u_{1xx} are thereby easily determined from the derivation rule:

$$\begin{aligned} &\text{symmetry}: \quad \frac{\mathrm{d}^n}{\mathrm{d}x^n}\varphi(b+x) = (-1)^n \frac{\mathrm{d}^n}{\mathrm{d}x^n}\varphi(b-x) \\ &\text{antisymmetry}: \quad \frac{\mathrm{d}^n}{\mathrm{d}x^n}\varphi(b+x) = (-1)^{n+1} \frac{\mathrm{d}^n}{\mathrm{d}x^n}\varphi(b-x) \end{aligned} \tag{3.55}$$

and the outer derivative values are set to $\zeta^+_x = -\zeta^-_x$, $u^+_{1x} = u^-_{1x}$ and $u^+_{1xx} = -u^-_{1xx}$.

3.3 Advancing in time

While the spatial discretisation of governing equations is fully performed above, the time discretisation remains outstanding to advance the propagation of water waves in time.

3.3.1 A Runge-Kutta type method

It is proposed to solve The ODE system (3.40) with the total variation diminishing (TVD) Runge-Kutta time discretisation. This was introduced by Shu (1988) for steady state calculations with large Courant-Friedrichs-Lewy (CFL) coefficients, and later developed by Shu and Osher (1988) for an efficient implementation of the high resolution, essentially non-oscillatory (ENO), schemes for systems of hyperbolic conservation laws.

An explicit single-step r-stage TVD Runge-Kutta scheme thereby reads for (3.40):

$$\begin{aligned}
&\widetilde{\mathfrak{U}}_1^{(0)} = \widetilde{\mathfrak{U}}_1^n \\
&\widetilde{\mathfrak{U}}_1^{(i)} = \sum_{j=0}^{i-1} \left[\alpha_{ij} \widetilde{\mathfrak{U}}_1^{(j)} + \beta_{ij} \Delta t \mathfrak{L}_{\mathrm{d}} \left(t^n + d_j \Delta t, \mathfrak{U}_N^{(j)}, \mathfrak{U}_N^{\prime(j)}, \mathfrak{U}^{\prime\prime(j)} \right) \right], \ i = 1, ..., r \\
&\widetilde{\mathfrak{U}}_1^{n+1} = \widetilde{\mathfrak{U}}_1^{(r)}
\end{aligned} \tag{3.56}$$

where coefficients α_{ij}, β_{ij} and d_j can be designed to achieve a desired order of accuracy. Such a set of coefficients is not necessarily unique for a given order and is generally chosen to render the stability of the method with optimal CFL conditions.

3.3.2 Coefficients for 2^{nd} and 3^{rd} orders

For $r \leqslant 4$, this solver can be made r^{th} order accurate, as stated in Cockburn and Shu (1989). The first order scheme corresponds to the classical forward Euler scheme with $\alpha_{10} = \beta_{10} = 1$, while the optimal second and third order schemes are characterised by the following sets of coefficients, according to the values proposed by Shu and Osher (1988):

- Second order $r = 2$:

$$\alpha_{10} = \beta_{10} = d_1 = 1 \,, \ \alpha_{20} = \alpha_{21} = \beta_{21} = \frac{1}{2} \,, \ \beta_{20} = d_0 = 0 \tag{3.57}$$

- Third order $r = 3$:

$$\begin{aligned}
&\alpha_{10} = \beta_{10} = d_1 = 1 \,, \ \alpha_{20} = \frac{3}{4} \,, \ \beta_{20} = \beta_{30} = \alpha_{31} = \beta_{31} = d_0 = 0 \,, \\
&\alpha_{21} = \beta_{21} = \frac{1}{4} \,, \ \alpha_{30} = \frac{1}{3} \,, \ \alpha_{32} = \beta_{32} = \frac{2}{3} \,, \ d_2 = \frac{1}{2}
\end{aligned} \tag{3.58}$$

From a computational point of view, the main drawback in using a Runge-Kutta type scheme here is that for an order of more than one, the calculation of intermediate stages $\widetilde{\mathfrak{U}}_1^{(i)}$ in (3.56) requires the evaluation of $\mathfrak{U}_N^{(j)}$ in function of $\widetilde{\mathfrak{U}}_1^{(j)}$ (actually $\mathfrak{U}^{(j)}$ in function of $\widetilde{\mathfrak{U}}_1^{(j)}$). This implies the solution of the elliptic system $r-1$ times per time step, plus the final evaluation of $\mathfrak{U}^{n+1}$ in function of $\widetilde{\mathfrak{U}}_1^{n+1}$, thus increasing calculation times significantly.

Due to the high order spatial derivatives of the PDE (3.27), this explicit and local time discretisation suffers from a severe time step restriction. In fact, it is recognised that further enhancements are needed in terms of the temporal discretisation, for example by considering either nonlocal or implicit techniques (see Xu and Shu, 2010).

Chapter 4

Validation and application of the one-layer model

In order to validate the one-dimensional numerical tool, this chapter introduces the reproduction of two classic benchmark test cases. Firstly, the propagation over a flat bed of solitary waves with different nonlinearity is considered, using the framework of Boussinesq theory (1872). Secondly, two wave dispersion scenarios over a submerged bar are simulated using laboratory data presented and used by Dingemans (1994). Finally, an application of the model to pressure forced storm surges and solitary wave shoaling is presented.

One-layer results are exclusively presented here, as the multi-layer option is still under implementation into the code. As discussed in subsection 2.4.1 of chapter 2, the horizontal velocity u_1 can be chosen to be evaluated at the specific depth $\kappa_1 = -0.53h$, as suggested by Nwogu (1993) through an optimisation of the linear dispersion relationship of the model.

Hereafter, the appendage "kr" attached to the words scheme and run refers to the overall order of accuracy of the numerical approximation, as a combination of the spatial discretisation order k in (3.26) with the temporal discretisation order r in (3.56). A priori independent from each other, k and r are generally set to the same value to guarantee a certain consistency for the overall order of the scheme.

4.1 Solitary wave propagation

The solitary wave is of finite amplitude and permanent form, resulting from the balance between nonlinear and dispersive effects. Initially observed in 1834 by Scott Russell, while conducting some experiments to determine the most efficient design for canal boats, this "wave of translation" was further presented in the experimental reports of Scott Russell (1844), Bazin (1862) and Clapeyron (1863). A decade later, Boussinesq (1871, 1872) published a general theoretical description of the solitary wave in which he obtained an analytical solution for the wave profile, wave propagation speed and water particle velocities, thus validating the empirical relationship proposed by Bazin for the wave speed. Since then, several attempts, summed up in Lee *et al.* (1982), have been made to get a higher order theory

and improve upon this solution (e.g. up to ninth order by Fenton, 1972). Lately, Tanaka (1986) developed a very accurate iterative scheme for the solution of the full boundary value problem, which allows the simulation of highly nonlinear solitary waves.

Owing to the low nonlinearity of the solitary waves simulated here, Boussinesq's (1872) explicit expressions of the free surface elevation and the horizontal velocity are used as the "analytical" forcing solution for simplicity in the following comparisons to validate the model:

$$\begin{aligned} \zeta(x,t) &= a\sec^2\left(\sqrt{\frac{3a}{4h^3}}(x-ct)\right) \\ U(x,z,t) &= \sqrt{gh}\left(\frac{\zeta}{h}-\frac{1}{4}\frac{\zeta^2}{h^2}+\frac{h}{3}\left(1-\frac{3}{2}\frac{(z+h)^2}{h^2}\right)\frac{\mathrm{d}^2\zeta}{\mathrm{d}x^2}\right) \end{aligned} \tag{4.1}$$

where h is the local water depth, a the wave amplitude and c the wave speed given by

$$c=\sqrt{g(h+a)} \tag{4.2}$$

Both expressions in (4.1) are evaluated at each time step to force the free surface elevation ζ and the velocity u_1 at the left border of the calculation domain as an inlet boundary condition. A still water initial state is imposed, with no wave motion $\zeta(x,0)=u_1(x,0)=0$.

4.1.1 Validation of the numerical scheme

Three typical solitary waves are investigated, with amplitudes $a=0.1$ m, 0.2 m and 0.3 m, propagating over a uniform bed of constant depth $h=1$ m. Simulations are performed over a 110 m horizontal distance partitioned into $M=110$ cells. Figure 4.1 shows a comparison between the analytical solution and numerical results to orders $kr=01$, 11 and 22.

As expected, the higher the order of the scheme, the more precise and slicker is the numerical curve. For the first case (a), close to a linear situation, an excellent agreement between analytical and numerical 11 and 22 solutions is observed. Then, a loss of matching of numerical curves with the analytical solution can be noticed in panels (b) and (c), with a gently decreasing amplitude and a growing phase shift, when the nonlinearity parameter $\varepsilon_0=a/h$ is incremented. The finite volume forward Euler method, corresponding to runs 01, is the most diffusive here; however this purely numerical issue can be easily eliminated by raising the overall order of the discretisation scheme, as shown by runs 11 and 22.

Generally, the one-layer model results are quite good and very close to the solution of Boussinesq (1872), despite the nonlinear phase shift. In fact, these discrepancies can be expected to abate by increasing the number of layers in the model. Obviously, it is important to keep in mind that Boussinesq's analytical expressions are not an exact solution of the present multi-layer model, which contains some more nonlinear terms. Actually, the most linear situation (a) is the only relevant case for conclusions to be made as to the accuracy of the model compared to this analytical solution. Higher order solitary wave theories should therefore be considered (e.g. Tanaka, 1986) to reproduce highly nonlinear conditions.

In addition, an initial small overestimation of the amplitude of the soliton, on coming into the domain, and the appearance of a dispersive tail of shorter waves behind should be noted with the increase of the nonlinearity parameter. These fluctuations tend to decrease in time and seem to be part of the transient state mentioned by Wei and Kirby (1995) and Gobbi *et al.* (2000) as a consequence of the fact that the inlet condition of Boussinesq (1872) does not

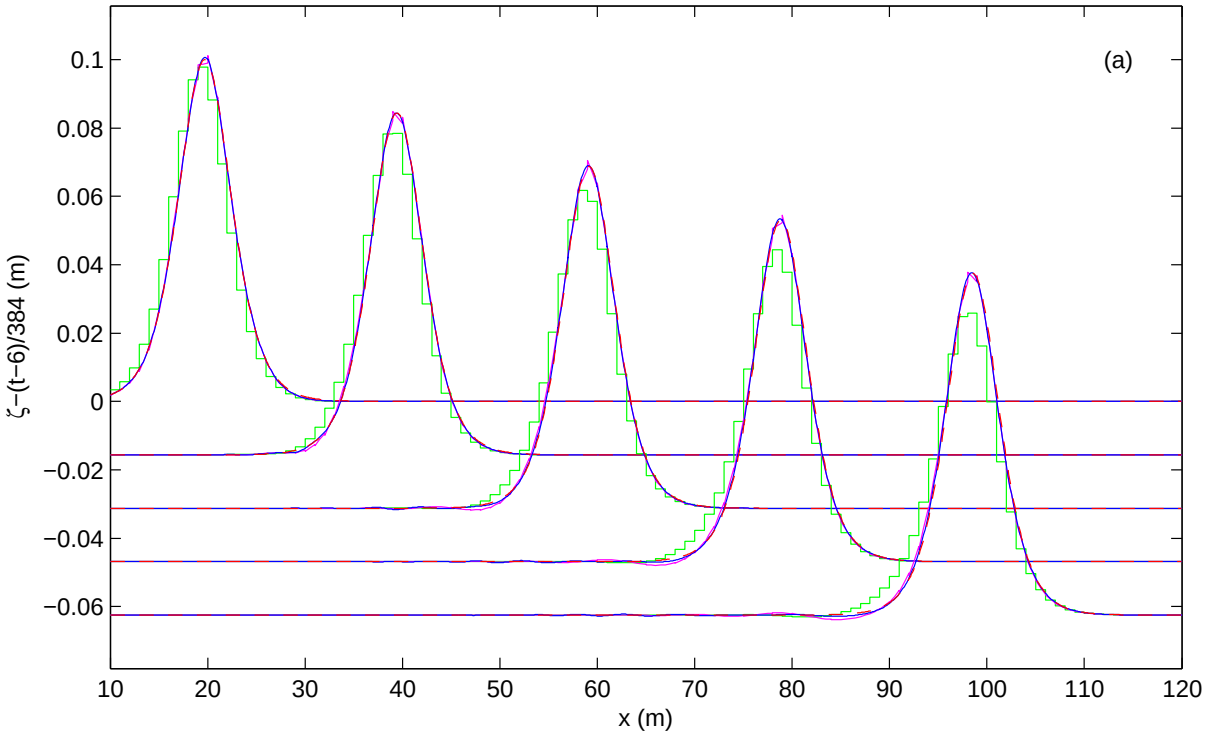

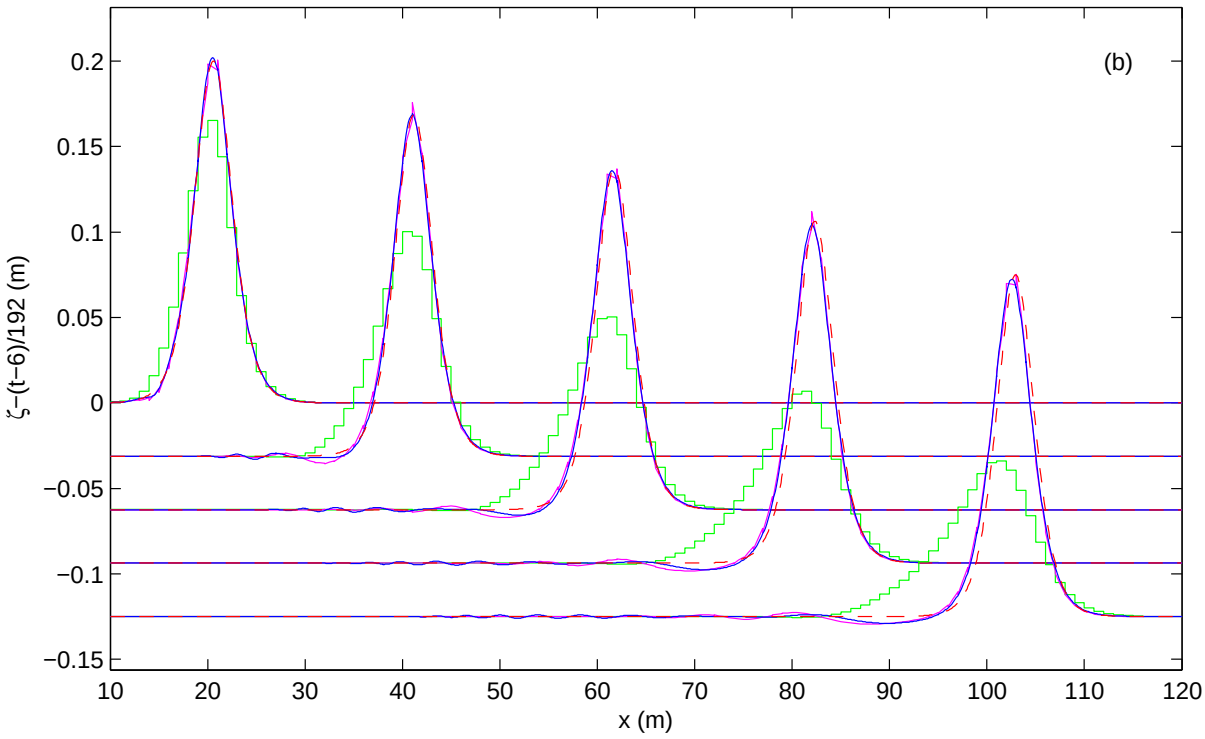

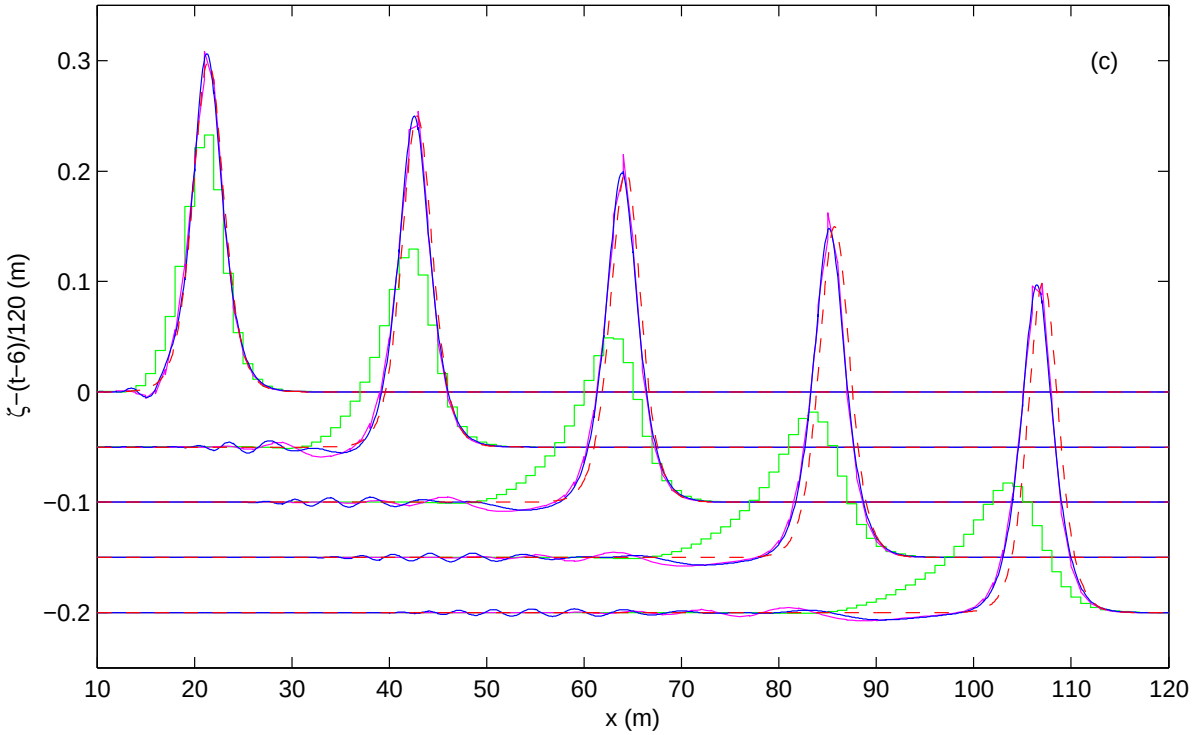

Figure 4.1: Comparison between analytical (- -) and numerical 01 (-), 11 (-) and 22 (-) free surface elevations displayed each 6 s for three solitary waves of nonlinearity $\varepsilon = \frac{a}{h}$ (a) 0.1, (b) 0.2 and (c) 0.3

satisfy the model. Nonetheless, since the primary wave travels faster than the tail, this should be left far behind without interfering with the soliton, and the permanent form solitary wave can be expected after a relatively long time, depending on the amplitude of the wave.

4.1.2 Comparison Boussinesq versus RANS

These positive waves are also reproduced by using the COBRAS model (COrnell BReaking wave And Structure), within a 110 m long and 1.5 m high domain in the vertical plane which is numerically represented with a grid comprised of 2200 x 50 cells. The same soliton of Boussinesq (1872) is forced at the left boundary, a free slip rigid wall is used for the bottom and an open boundary condition is chosen for the top and right borders of the domain. COBRAS is a two-dimensional model that solves the Reynolds Averaged Navier-Stokes (RANS) equations for the mean flow field with a modified k-ε turbulence closure based on the nonlinear eddy viscosity assumption and a volume of fluid (VOF) method for free surface tracking. Details about this very well known wave model can be found in the papers of Lin and Liu (1998a, 1998b) and Liu *et al.* (1999). The one-layer model results of previous runs 22 are now compared to RANS simulations in Figure 4.2.

A similar behaviour can be generally observed for both Boussinesq and RANS type numerical models in each case, in spite of some additional noisy oscillations and a clear non-zero offset before and after the soliton identified for RANS curves, and probably due to the low vertical

resolution of the grid. Going into detail, the Boussinesq model is seen to maintain the amplitude of the soliton in a better way than the RANS model for growing nonlinearities. Finally, the presence of the dispersive tail detected behind the soliton is confirmed by the RANS model, while stretched over a longer distance than in the case of Boussinesq.

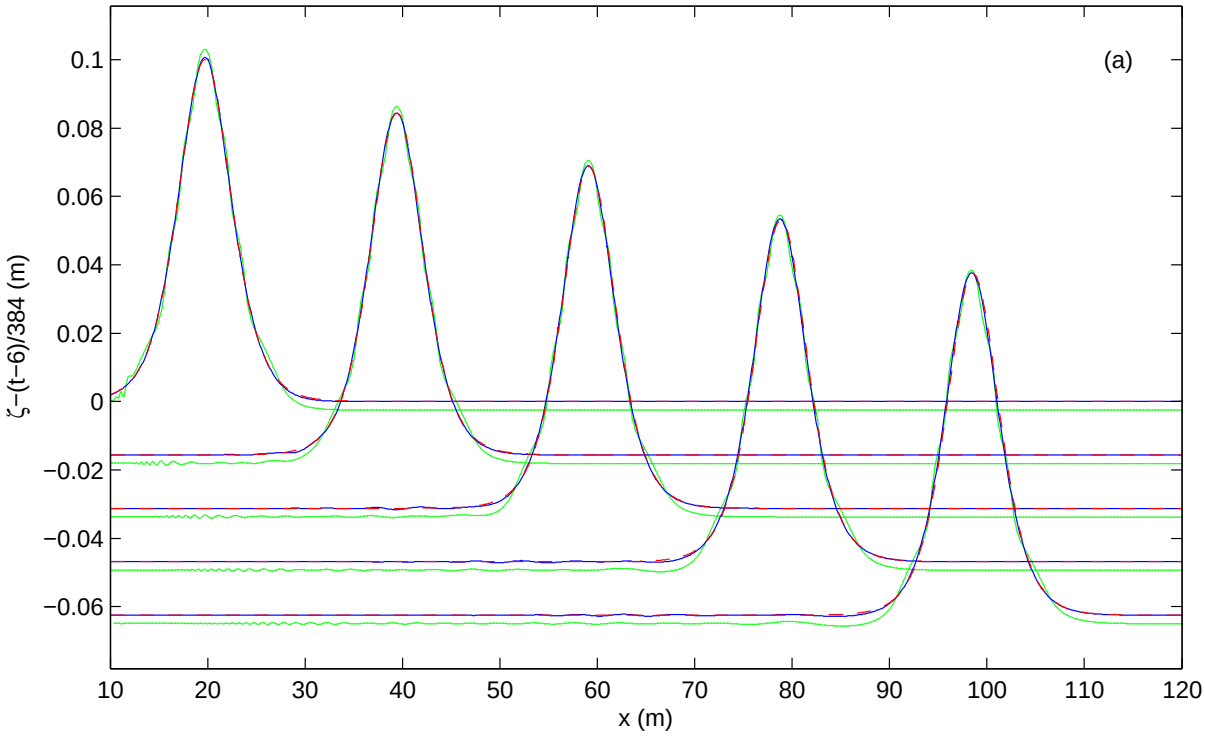

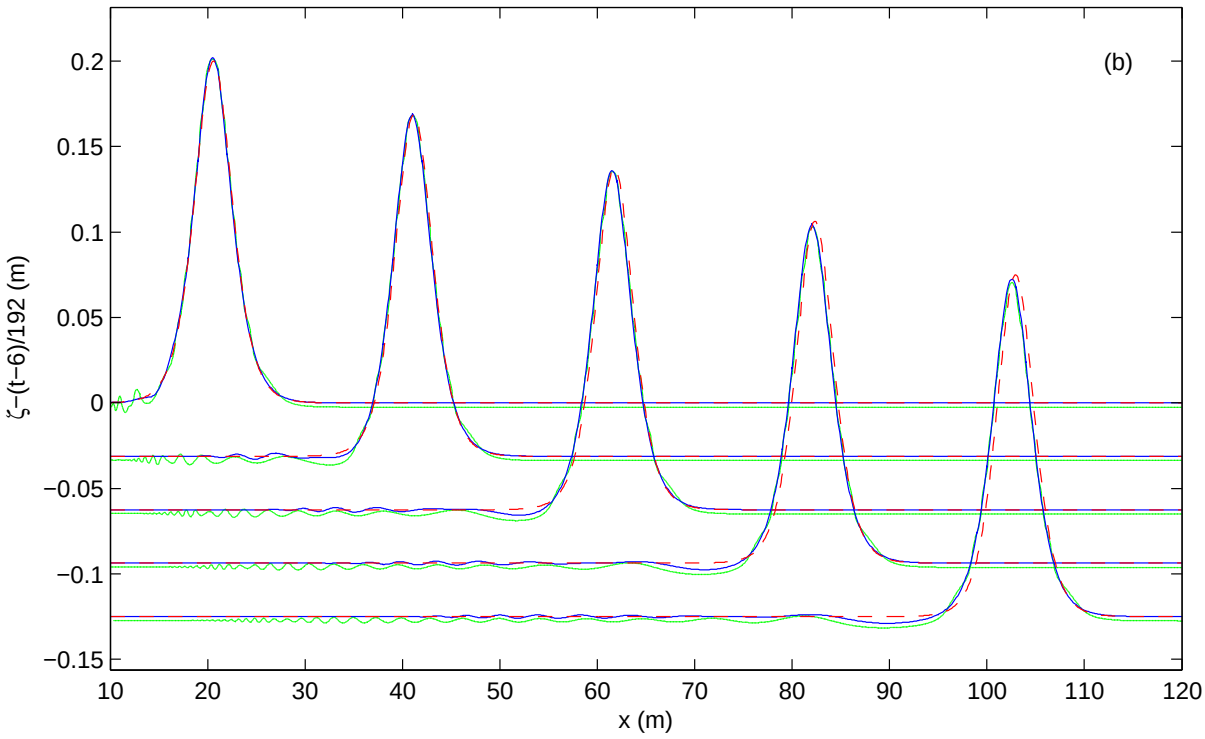

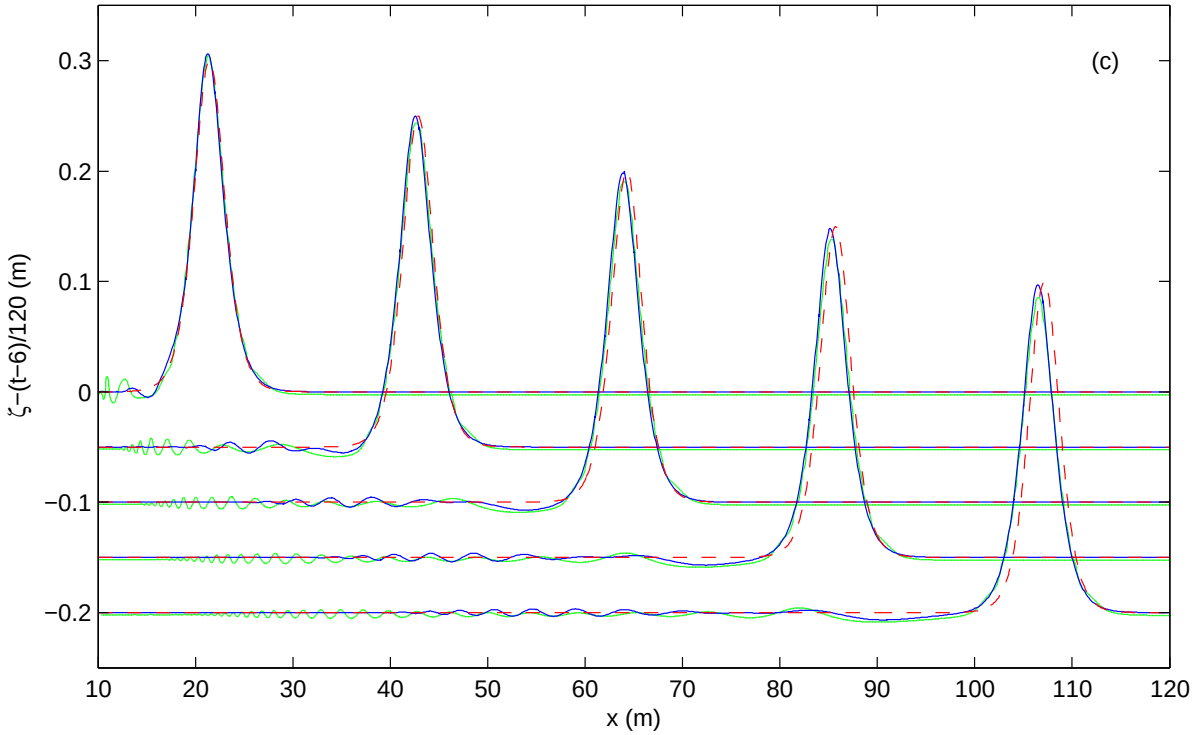

Figure 4.2: Comparison between analytical (- -) and numerical RANS (-), Boussinesq 22 (-) free surface elevations displayed each 6 s for three solitary waves of nonlinearity $\varepsilon = \frac{a}{h}$ (a) 0.1, (b) 0.2 and (c) 0.3

It can be concluded from this comparison that the present Boussinesq type model, run at its lowest level of accuracy with only one layer for the vertical profile representation of the wave motion, is shown to achieve at least the same accuracy as a more sophisticated model solving the RANS equations, for a lower resolution.

4.2 Wave evolution over a submerged bar

To validate the model for space varying bathymetries, the laboratory data of Dingemans (1994), dealing with the generation of harmonic waves over a submerged bar, are used. Since the model does not take into account the energy dissipation mechanism due to wave breaking, only the two non-breaking experimental situations A and C are examined and numerically reproduced. The model is forced at the left boundary to generate the inlet wave into the domain, using the second order theory of Stokes (1847), for which the free surface elevation and the horizontal velocity are given by the following expressions:

$$\zeta(x,t) = a\cos(kx-\sigma t) + \frac{ka^2}{4}\frac{\cosh(kh)}{\sinh^3(kh)}(2+\cosh(2kh))\cos(2(kx-\sigma t))$$
$$U(x,z,t) = \sigma a\frac{\cosh(k(z+h))}{\sinh(kh)}\cos(kx-\sigma t) + \frac{3k\sigma a^2}{4}\frac{\cosh(2k(z+h))}{\sinh^4(kh)}\cos(2(kx-\sigma t)) \tag{4.3}$$

where h is still the local water depth and a the wave amplitude. The wavenumber $k = \frac{2\pi}{L}$ and the angular wave frequency $\sigma = \frac{2\pi}{T}$ are inversely proportional to the wave length L and the wave period T. As for the solitary wave forcing, both the free surface elevation ζ and the velocity u_1 are specified in time at the left border of the calculation domain using (4.3) and the initial inner conditions are set to zero, i.e. $\zeta(x,0) = u_1(x,0) = 0$.

4.2.1 Comparison to experimental data

The experimental measurements, performed by Professor Gert Klopman of Delft Hydraulics in 1993, are an exact recreation of the original tests done by Beji and Battjes (1993), but with a linear scale of 2. The scaled profile of the bar can be appreciated in Figure 4.3. The scaled forcing conditions are $T = 2.02\sqrt{2}$ s and $a = 0.02$ m for case A, and $T = 1.01\sqrt{2}$ s and $a = 0.041$ m for case C. The numerical setup is composed of five wave gauges, whose locations are indicated above the bar in Figure 4.3, and correspond to the experimental setup of the measurement series 01 in the report of Dingemans (1994). For both cases, schemes 22 and 33 are run with a number $M = 100$ of cells ($\Delta x = 0.5$ m). Additional runs with a higher resolution $M = 160$ ($\Delta x = 0.3125$ m) are performed for case C. Comparisons of the free surface elevation time series, between model predictions and experimental observations, are presented for each sensor in the next three Figures.

Basically, as it approaches the bar, the wave starts changing form and steepens due to nonlinear shoaling. Nonlinear energy transfers, occurring above the bar, induce the dispersion of the wave and its decomposition into shorter superharmonic waves. These harmonics, then moving away from the bar become deep water waves with higher kh values that should belong to the range of validity of the model to be reproduced properly.

The forced wave of case A, characterised by an initial $kh = 0.7$, is perfectly well captured by the two first sensors, located upstream from the bar, for both numerical simulations of Figure 4.3. From there, some discrepancies appear at the three other positions for scheme 22, while the wave field is still well reproduced by scheme 33 for sensors 3 and 4. The small phase shift, observed from the third sensor for both schemes, is ascribed to the linear dispersion accuracy limit of the model near $kh \approx \pi$, exceeded by the presence of dominant $kh \approx 4$ waves (Lynett and Liu, 2004a) behind the bar. At sensor 5, scheme 33 gets much closer to the measurements than scheme 22, and even slightly better than the one-layer simulation of Lynett and Liu (2004a) at the corresponding sensor #3; however both one-layer results still present the same deviation from the experimental dots in the largest trough of this time series, owing to the nonlinear inaccuracy of the model for such deep water kh values.

Regarding case C, the wave enters the domain with a $kh = 1.8$ and waves of $kh = 6.3$ are reported behind the bar by Lynett and Liu (2004a) for the second harmonic. As expected, numerical results are not as good in Figure 4.4 as for the previous case A for the same resolution, due to the presence of deeper water waves. A finer mesh ($\Delta x = 0.3125$ m) makes scheme 33 tend to capture better the nonlinear shape and amplitudes of the wave field (Figure 4.5). Nevertheless, the one-layer model becomes inaccurate when applied to simulate such highly dispersive waves. Actually, a more precise set of equations is required in such cases,

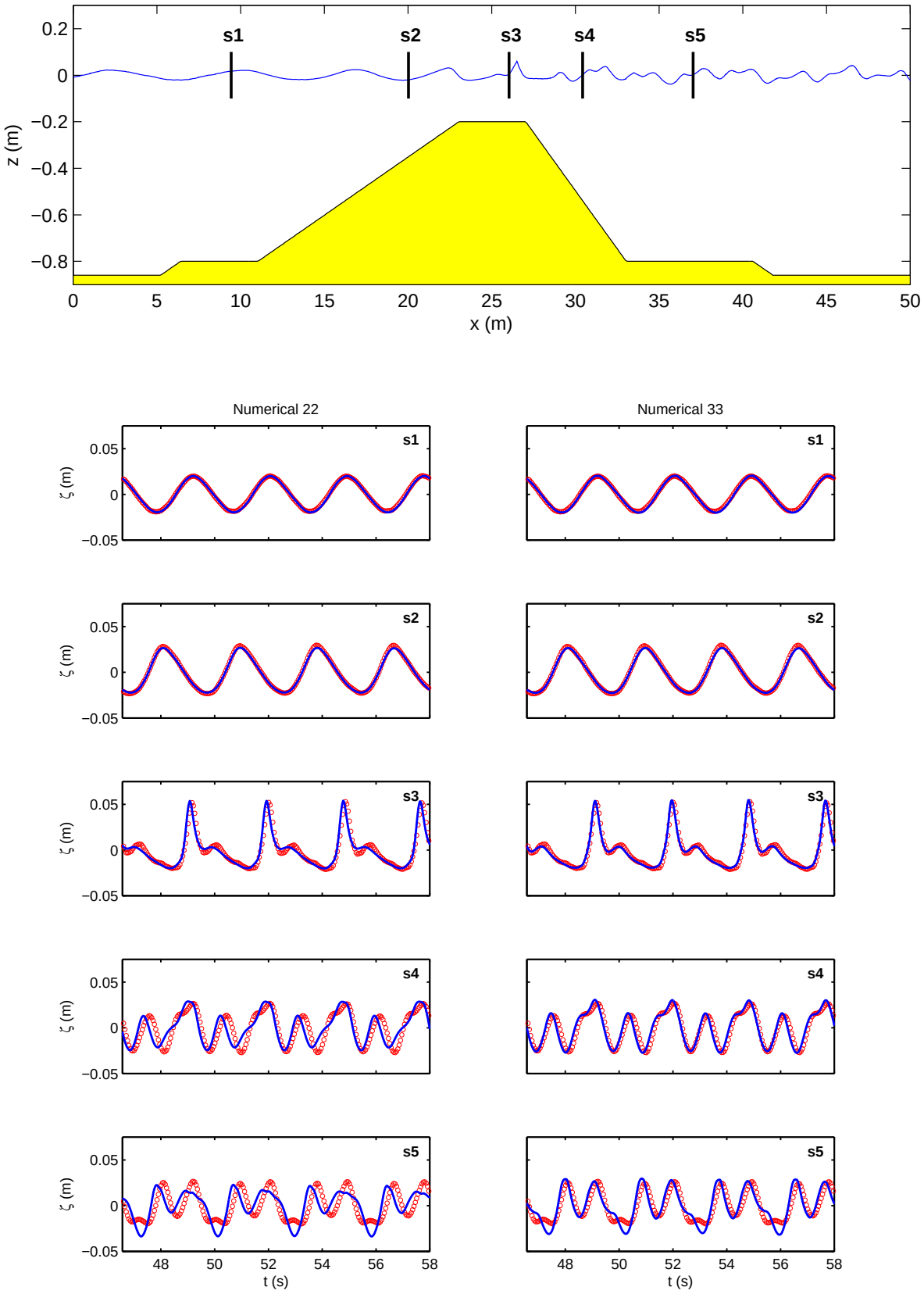

Figure 4.3: Case A ($M = 100$): computed 33 free surface elevation displayed at time $t = 58$ s, and comparisons between experimental (○) and numerical (-) time series of the wave field registered by five sensors for schemes 22 and 33

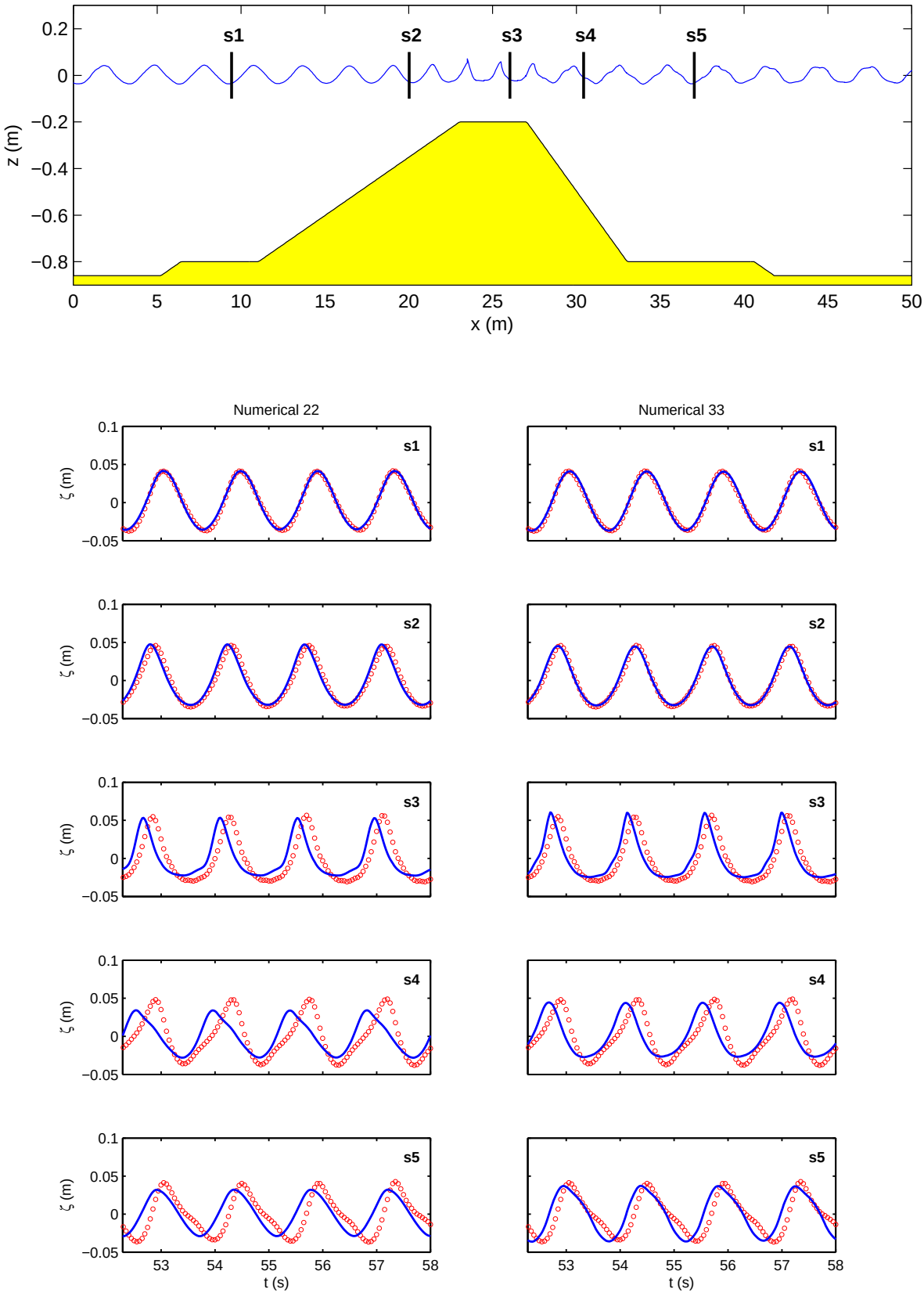

Figure 4.4: Case C ($M = 100$): computed 33 free surface elevation displayed at time $t = 58$ s, and comparisons between experimental (○) and numerical (-) time series of the wave field registered by five sensors for schemes 22 and 33

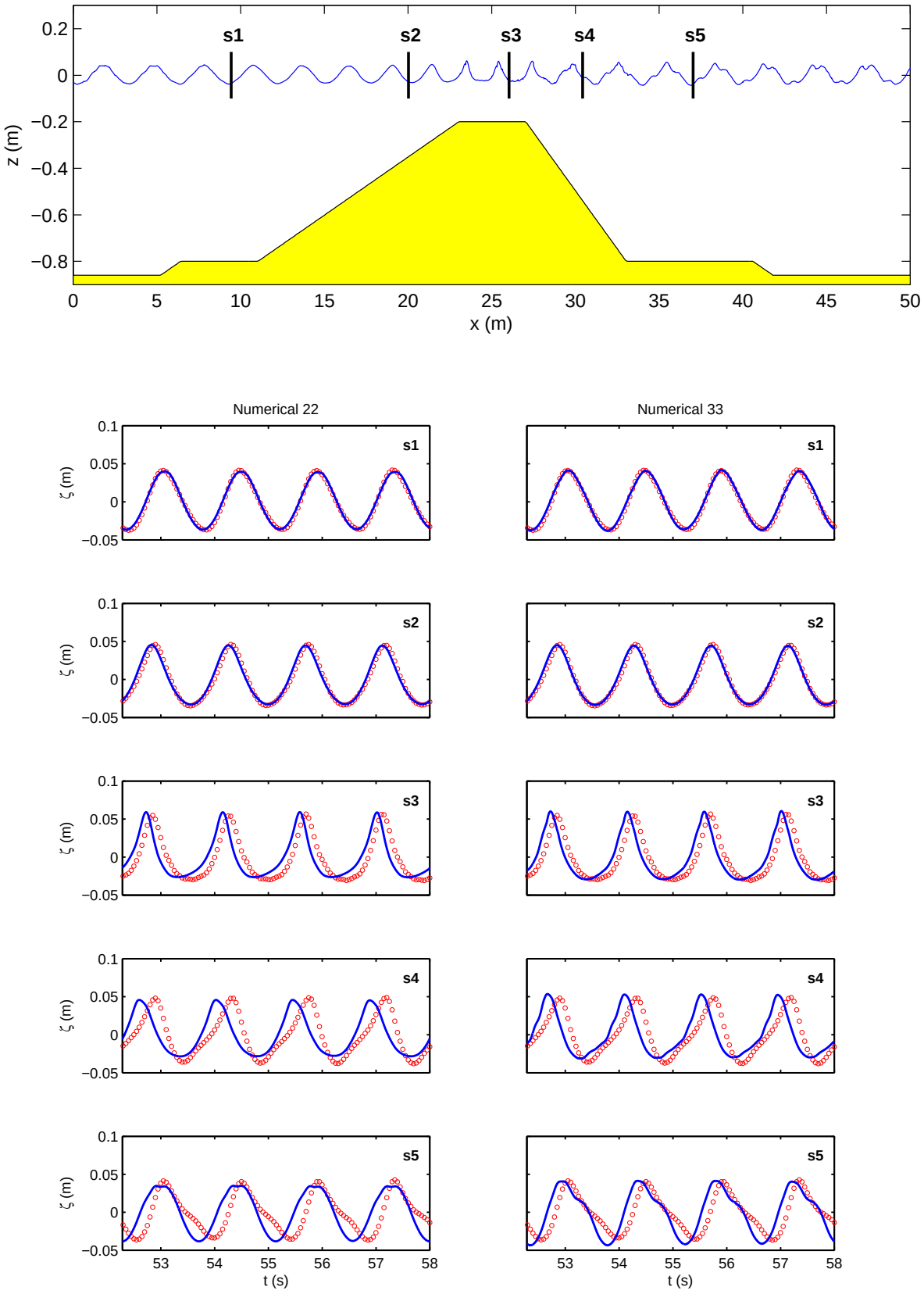

Figure 4.5: Case C ($M = 160$): computed 33 free surface elevation displayed at time $t = 58$ s, and comparisons between experimental (○) and numerical (-) time series of the wave field registered by five sensors for schemes 22 and 33

and the implementation into the code of the more general N-layer system analysed by Lynett and Liu (2004b) is underway.

4.2.2 CPU efficiency of the code

The main objective of numerical simulation resides in approaching the convergence of the scheme as quickly as possible. This is the very essence of the efficiency of a numerical code. To illustrate the efficiency of the model, CPU running times, corresponding to the simulation of the previous experimental situation C of Dingemans (1994), are now compared for both schemes 22 and 33 with different mesh resolutions in Figure 4.6. For reference, the model was executed and run on a Windows XP operating system platform by an Intel® Core™2 Quad CPU Q9300 @ 2.50GHz 2.48GHz multiprocessor. Given the underlined inaccuracy of the one-layer model in that case, the finest run (scheme 33 with $M = 160$) is taken here as the reference solution instead of measurements for the numerical convergence.

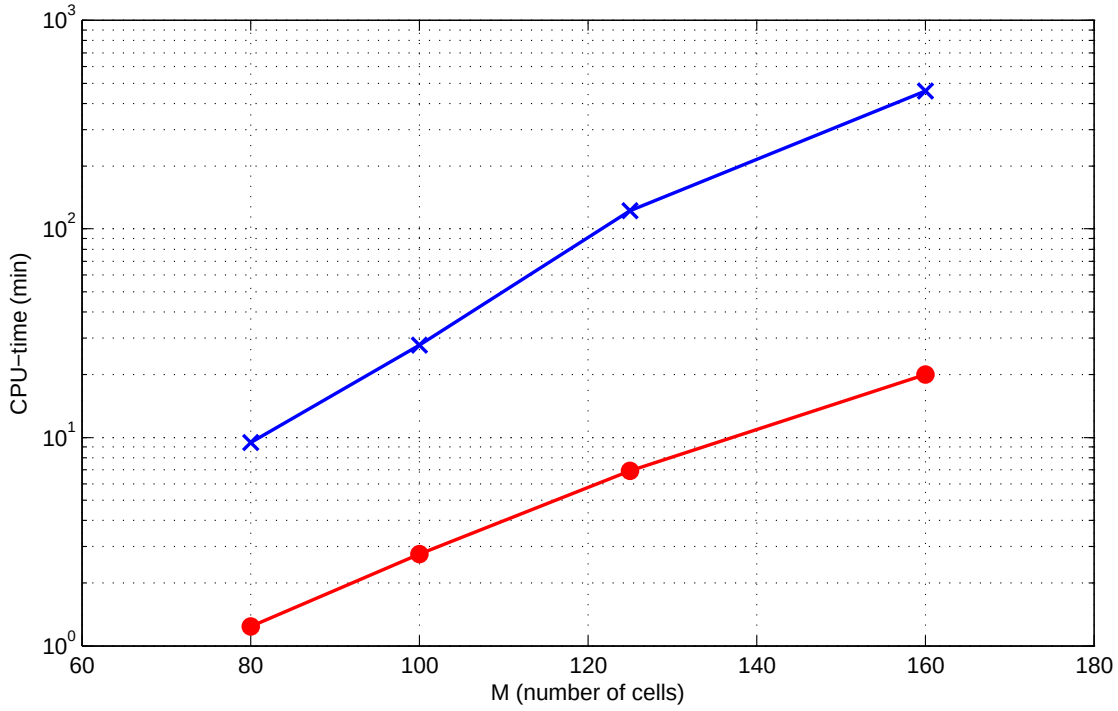

Figure 4.6: Computing times of schemes 22 (•) and 33 (×)

At first sight, the code can run very fast as well as very slowly: from about one minute for scheme 22 with $M = 80$, to several hours for scheme 33 with a double spatial resolution. This is not surprising if we consider the additional complexity induced in the scheme when raising the orders k and r. Regarding the spatial discretisation, the size of the final ODE system to solve increases M times with the order k, and calculations are duplicated for numerical fluxes and quadrature rules. Moreover, as discussed in the time discretisation section 3.3 of chapter 3, the Runge-Kutta method is not an optimal choice here, since it might cause drastic effects on CPU times to high r orders, due to the increasing number of intermediate stage evaluations necessary, in addition to the severe time step restrictions.

The determining choice of both the overall order of the numerical discretisation and the mesh resolution then remains up to the user, depending on his needs in terms of accuracy and speed required for the simulation, and first and foremost on the expected sophistication of the wave field to be reproduced. For instance, as we can catch a brief glimpse in Figures 4.4 and 4.5 of case C, scheme 33 with $M = 100$ gets slightly closer to the reference solution than scheme 22 with $M = 160$ (sensors 3, 4 and 5), and despite the run taking 40% longer to finish, it is certainly the better of these two options given the relatively short additional CPU running time, in the order of eight minutes.

As the sloping tendency of CPU time in function of the mesh resolution is higher for scheme 33 than for scheme 22 in Figure 4.6, some methodology to get CPU efficient accurate runs may be inferred: while manipulating the order does not break the efficiency so much at quite small M values, it would be preferable to refine the mesh rather than raising the order for large M values. This is obviously not a rigorous inference, since one would need to compare the CPU times of different runs which provide the same accuracy.

4.3 Pressure forced storm surge modelling

As discussed in chapter 1, storm surges driven by low pressure weather systems represent a real threat of inland flooding for both Pacific and Atlantic coasts in Mexico. In the hurricane season, it is usually necessary to evacuate large areas, thereby causing major socio-economic problems in addition to irreversible ecological damage, in particular when coastal infrastructure is not properly planned. So, to get a better understanding of transient stages of storm surges, the one-layer model is applied to examine a numerical Boussinesq type dispersive response to a moving low pressure system forcing.

Here, storm surges are generated ideally from the only pressure gradient source term, without considering the wind effect. Simulations are initiated from a calm sea state set of initial conditions $\zeta(x,0) = u_1(x,0) = 0$, and are performed at an overall order 22, on a uniform bed of constant depth $h = 20$ m, with a moving Gaussian trough pressure forcing:

$$p_{\text{atm}} = p_0 \exp\left(-\frac{(x-ct)^2}{R^2}\right) \tag{4.4}$$

Where p_0 is the lowest pressure value of the function, R some characteristic evaluation of the Gaussian radius and c the celerity of the forcing. Four situations can be identified and are reproduced in Figure 4.7 for the displacement of this low pressure function:

$$c = 0\,,\ c < \sqrt{gh}\,,\ c \approx \sqrt{gh}\,,\ c > \sqrt{gh} \tag{4.5}$$

In each case, a dispersion of the two free waves travelling in opposite directions can be observed, which was not taken into account in the non dispersive analytical solution of the wave equation for forced small amplitude shallow water waves, presented by Nielsen *et al.* (2008). In the second panel (b), it is interesting to see how the superharmonics of the right free wave go over the asymptotic steady forced positive surge. Panel (c) shows a resonance

phenomenon, with an increasingly growing wave height under the pressure trough. Actually, such a situation is hardly observable as the speed of hurricanes varies in time. Besides, it would be interesting to investigate a moving pressure system with a time varying celerity c.

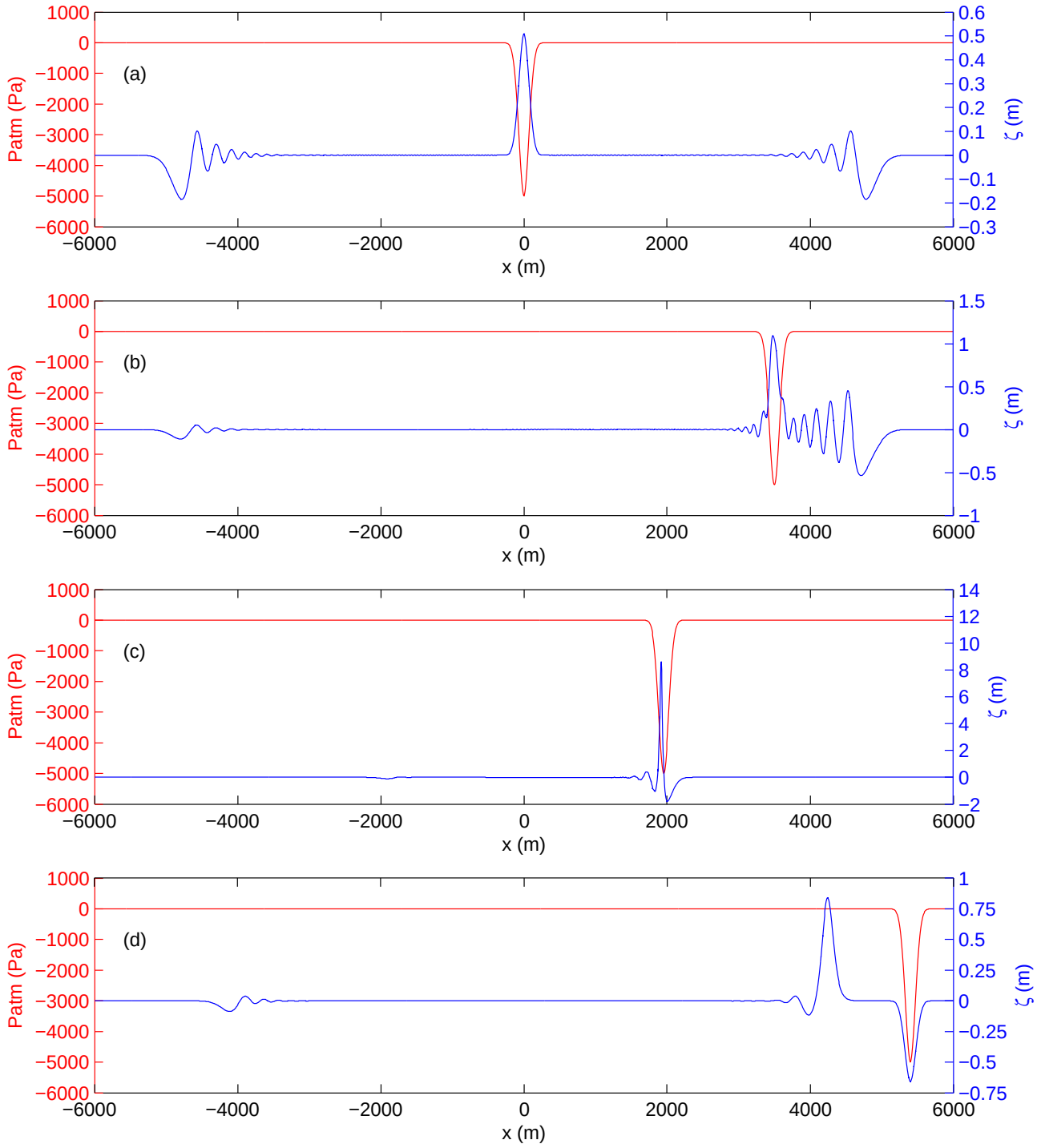

Figure 4.7: Numerical free surface response to a Gaussian trough atmospheric pressure forcing, displayed at times (a) $t = 350$ s for $c = 0$, (b) $t = 350$ s for $c < \sqrt{gh}$, (c) $t = 140.5$ s for $c \approx \sqrt{gh}$ and (d) $t = 300$ s for $c > \sqrt{gh}$

Furthermore, it clearly appears that for both directions, a negative surge will always precede a positive one, which can be seen as a recession of the coastline followed by smaller waves or a higher positive surge, depending on the celerity c of the low pressure system.

As for an attempt to corroborate the qualitative aspect of numerical results, the free surface residual time series of a measured storm in Campeche (2009), obtained after the extraction of the reconstructed astronomical tide component, is shown in Figure 4.8. Finally, a similar behaviour between field data and case (b) can be identified.

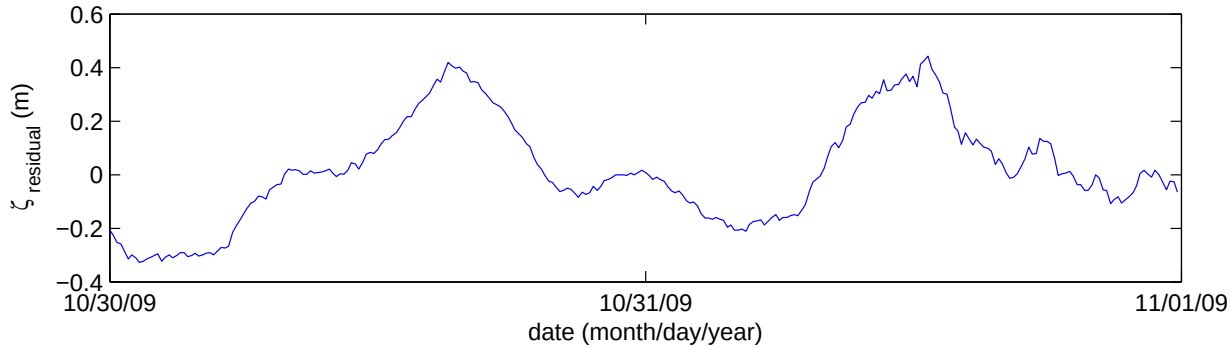

Figure 4.8: Extract from a measured storm surge, Campeche Mexico (2009)

4.4 Shoaling of a weakly nonlinear solitary wave

Referring now to the other major maritime threat in Mexico, this section presents an additional simulation for the shoaling of a weakly nonlinear solitary wave, in order to illustrate the applicability of the one-layer model to tsunami waves. A soliton of Boussinesq (1872) of nonlinearity $\varepsilon_0 = 0.2$ is propagated through the inlet boundary condition on a slope 1:15 (see Figure 4.9), by using the previous explicit expressions in (4.1).

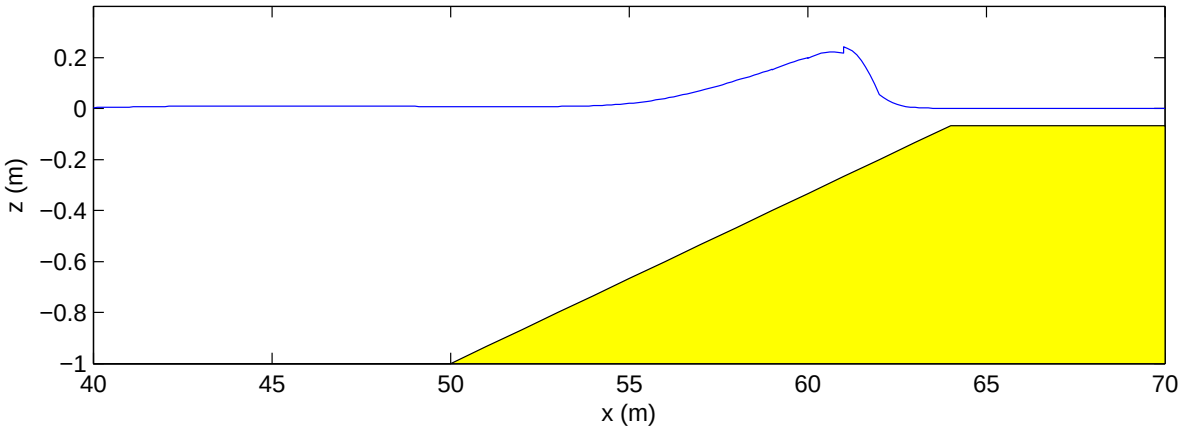

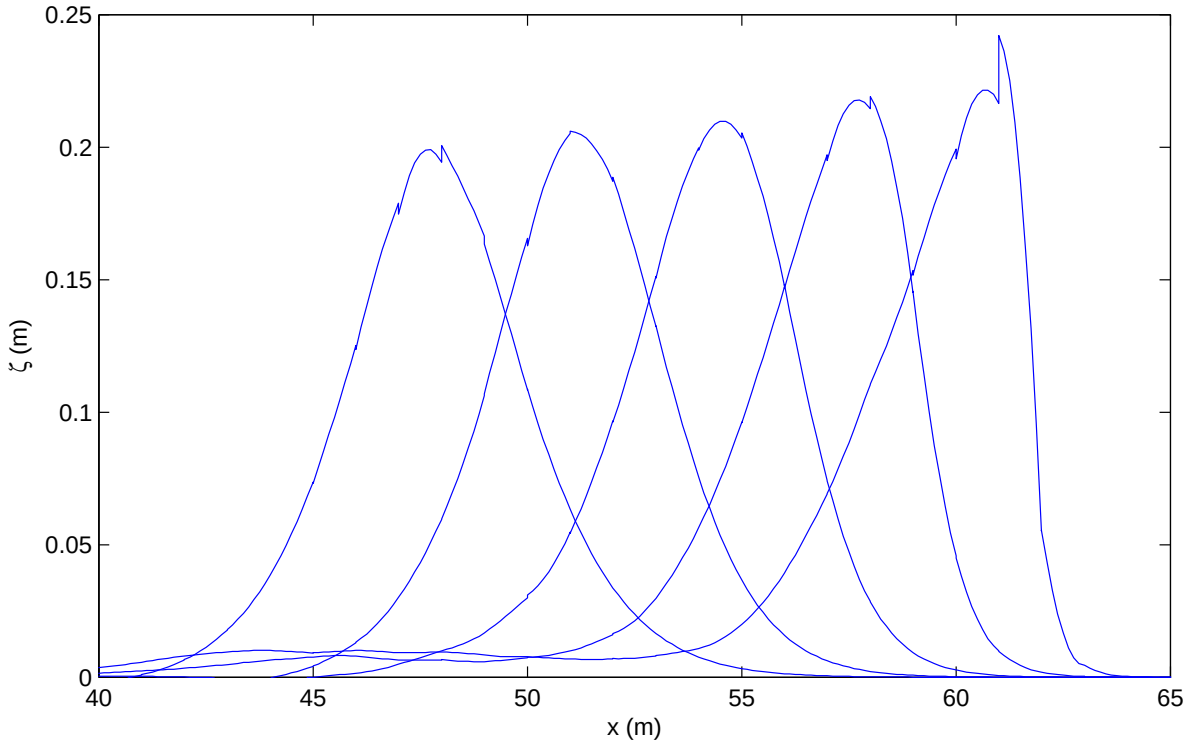

Figure 4.9: Numerical free surface elevations of a shoaling solitary wave of nonlinearity $\varepsilon = \frac{a}{h} = 0.2$, displayed at time $t = 18$ s (top) and each second from time $t = 14$ s (bottom)

The simulation is performed on a 1 m mesh resolution at an overall order 22, from a calm sea state of initial conditions $\zeta(x,0) = u_1(x,0) = 0$ perturbed by the entrance of the soliton into the domain. The wave first propagates over a 40 m long flat bottom before shoaling over the slope. The run is stopped just prior to breaking so as to avoid unwanted numerical noise. As expected, the wave crest grows in height over the slope and nonlinearity effects alter the wave form to an asymmetric profile like a tsunami wave front.

Chapter 5

Conclusions

Coastal engineering issues, when facing extreme maritime phenomena, are first introduced and the case of Mexico is adressed through an evaluation of hurricane induced storm surge and tsunami threats. Both theoretical and numerical approaches for the characterisation of water waves are then examined. A quite exhaustive revision of the state of the art about water wave propagation modelling is presented, that covers the main mathematical techniques in current use, from the simple phase-resolving linear mild slope equation to the most sophisticated high order Boussinesq type models. The selected multi-layer Boussinesq type model, developed in this thesis, is based on a first order expansion in dispersion and a subdivision into layers of the water column for a piecewise description of the vertical profile of the flow. A new set of two-dimensional governing equations is derived with the inclusion of vertical vorticity terms, that describes the fully nonlinear, horizontally rotational and dispersive shallow water flow dynamics of an incompressible and inviscid fluid system over uneven bidirectional bathymetries, with some variation in time of the seafloor for the simulation of submarine landslides. The one horizontal dimension equations are solved in space by the DG method, a class of finite element methods using discontinuous basis functions, usually chosen as piecewise polynomials, to approach the solution over the whole calculation domain. The spatial discretisation scheme of order $k \geqslant 0$ employs a local Lax-Friedrichs flux for hyperbolic components, while for parabolic and dispersive terms an alternating fluxes methodology is followed. The DG scheme is advanced in time by a TVD Runge-Kutta type algorithm of order $r \geqslant 1$. Finally, the numerical solver is tested and validated for one layer on classic benchmark test cases and show very good behaviour within the range of validity of the model.

5.1 Concluding remarks

It is clear that a full resolution of the three-dimensional Navier-Stokes equations is still far from being a worth considering option in large scale ocean modelling due to the current computing limitations. Actually, amongst the remaining modelling techniques, the Boussinesq type depth-integration of the equations is, to date, surely the most advanced and efficient alternative, while extending the validity of the shallow water depth-averaged equations to at least intermediate water conditions $\left(\frac{\pi}{10} \leqslant kh \leqslant \pi\right)$, through the addition of dispersive terms. Moreover, a multi-layer description of the system makes a Boussinesq

type model of a given order able to overcome the accuracy of any other higher order Boussinesq type model, while maintaining lower order derivatives in the governing equations and a relatively simple discretisation scheme. Regarding the vertical vorticity of Boussinesq type models, rotational terms should not be neglected in the momentum equations, and particularly to simulate tsunami waves into a harbour correctly. In addition, keeping a set of free coefficients, like for the location of layer variables in the present model, generally results very useful to calibrate the model properties to the analytical deep water theory of Stokes (1847). As discussed at the end of chapter 2, various linear and nonlinear characteristics might be involved within this procedure. The truth is that the optimisation strategy for such a calibration remains up to the user and the physical situation to be simulated and numerically reproduced, so as to be able to focus on certain properties only.

A unified LDG approach was undertaken for a new numerical implementation of the one-dimensional high order multi-layer Boussinesq type model, that takes full advantage of the capacities and numerical efficiency of the DG method. Numerical fluxes are designed so as to ensure numerical stability and a Gauss-Legendre quadrature rule is utilised to a consistent order with the spatial discretisation order of the scheme. The solver can be run for arbitrary orders of accuracy in space and time. An arbitrary number of layers for the vertical distribution of the internal kinematics of the flow is also prone to be a user-defined parameter very soon; the implementation into the code of the general multi-layer system is underway. The MUOLDAO model is very easy to be run with only one short input file to be filled in, according to the details of the simulation to be performed. Basically, it deals with solitary wave, first and second order Stokes (1847) type forcing, with inlet, closed and periodic boundary conditions and an arbitrary bottom function $h\left(x,t\right)$.

As a flat bottom validation test-case, the propagation of solitary waves, based on the analytical theory of Boussinesq (1872), was investigated. The one-layer model is shown to achieve the same accuracy as a more sophisticated model solving the RANS equations, for a lower resolution. The development of the dispersive tail behind the soliton, part of a known transient state resulting from the non-matching nonlinearity between Boussinesq's solution and Boussinesq type models, is then confirmed by the model with increasing nonlinearity and accredited by RANS type simulations with the same forcing conditions. The one-layer model was further applied to reproduce the laboratory data of Dingemans (1994) about the generation of harmonics above a submerged bar experimental test: for both cases simulated, a relatively good agreement between model predictions and experimental data was observed, even if as expected, the one-layer model turns out to be inadequate for simulating highly dispersive waves with $kh > \pi$ values.

As an application test case, the Boussinesq type response of the one-layer model to a moving Gaussian trough pressure forcing was examined as an ideal storm surge generation. As expected, the simulation allows the reproduction of the dispersion of the two opposite free waves into a long wave train, independently of the steady forced surge. Besides, these results can be qualitatively extrapolated, from the one-dimensional simulation to the two-dimensional reality, so as to be able to anticipate the behaviour of a storm surge approaching the coast, according to the celerity of a hurricane and the local bathymetry.

Finally, regarding the CPU efficiency of the code: raising the order of the polynomial basis rather than the mesh resolution, seems to be a good option to approach the convergence of the scheme with still relatively fast runs, as long as the number of cells remains quite small. Otherwise, the inverse methodology is recommended. Notwithstanding, a manipulation of the order of the scheme could play its full role in efficiency for two-dimensional problems, where the number of cells grows as M^2 in the simple case of a Cartesian grid.

While the MUOLDAO model is not directly applicable to the simulation of real physical situations, due to the one horizontal dimension limitation, it actually constitutes a very helpful numerical tool for academic research. In this way, it can be utilised to corroborate experimental laboratory studies, with wave-structure interaction and cross-shore sediment transport modelling as for some coastal engineering applications.

5.2 Future lines of work

The numerical code, developed from scratch during this investigation, represents a reliable base in high order Boussinesq type modelling to simulate the propagation and transformation of water waves in one dimension. Naturally, the next big step would be the two-dimensional implementation of the model as a culmination of the work. Furthermore, additional specific ideas can be mentioned as for some future lines of research, and are exposed below:

- Finish the extension of the solver to an arbitrary number N of layers as a user-defined parameter to be chosen in the input file, and complete the validation of the multi-layer model in chapter 4 in that regard, by running the code with $N > 1$.

- Implement a slope limiting routine to avoid non physical spurious oscillations close to contact discontinuities of the weak solution, and control thereby the numerical stability of the scheme: indeed the simulations of Dingemans' (1994) experimental cases were shown to present some transient instabilities close to the left border of the domain due to the initial discontinuity of velocity in the inlet Stokes (1847) type forcing condition.

- Investigate the implementation of a wave breaking criterion and validate it with the experimental situation B of Dingemans (1994). Design a wetting/drying numerical algorithm to reproduce beach flooding and validate it with the analytical solution of Carrier and Greenspan (1958) for sine wave runup on a planar beach, and the experimental results of Synolakis (1986, 1987) for solitary wave runup. Add the wind shear stress and bottom friction to the model as other energy dissipation mechanisms. Extend the model to porous media, with maybe an extra momentum equation to describe the flow within the permeable bottom layer.

- Implement a suitable open numerical boundary condition to allow the infinite radiation of all wave lengths at the borders of the calculation domain, so as to avoid a contamination of the solution induced by a reflection of waves inward.

- Apply the model to the generation of waves by a time moving seabed, as a submarine landslide type simulation. Compare the accuracy and performance of the N-layer model to other high order Boussinesq type numerical tools.
- Implement a parallel version of the code.

Actually, this pending work is still quite heavy and the author will likely continue the investigation under these lines of research in a close future.

Bibliography

[1] Abbott, M.B., McCowan, A.D. and Warren, I.R. (1984). Accuracy of Short-Wave Numerical Models. Journal of Hydraulic Engineering, 110(10), pp. 1287-1301.

[2] Abernethy, C.L. and Gilbert, G. (1975). Refraction of wave spectra. Hydraulics Research Station, Wallingford Report INT117.

[3] Agnon, Y., Madsen, P.A. and Schäffer, H.A. (1999). A new approach to high-order Boussinesq models. J. Fluid Mech., 399, pp. 319-333.

[4] Airy, G.B. (1845). Tides and waves. Encyclopedia Metropolitana, London, 192(5), pp. 241-396.

[5] Al-Mashouk, M., Reeve, D.E., Li, B. and Fleming, C.A. (1992). ARMADA: an efficient spectral wave model. Proc. 2nd Int. Conf. Hydr. Env. Modelling of Coastal, Estuarine and River Waters. Ashgate, 1, pp. 433-444.

[6] Barré de Saint-Venant, A.J.C. (1871). Théorie du mouvement non-permanent des eaux, avec application aux crues des rivières et à l'introduction des marées dans leur lit. C.R. Acad. Sc. Paris, 73, pp. 147-154.

[7] Bazin, H. (1862). Expériences sur les ondes et la propagation des remous. Comptes Rendus des Séances de l'Académie des Sciences, Paris, 55, pp. 353-357.

[8] Beji, S. and Battjes, J.A. (1993). Experimental investigation of wave propagation over a bar. Coastal Engineering, 19, pp. 151-162.

[9] Berkhoff, J.C.W. (1972). Computation of combined refraction-diffraction. Proc. 13th Intl Conf. Coastal Engng. ASCE, Vancouver, Canada, pp. 471-490.

[10] Bingham, H.B., Madsen, P.A., Fuhrman, D.R. (2009). Velocity potential formulations of highly accurate Boussinesq-type models. Coastal Engineering, 56, pp. 467-478.

[11] Booij, N. (1983). A note on the accuracy of the mild-slope equation. Coastal Engineering, 7, pp. 191-203.

[12] Borthwick, A.G.L., Ford, M., Weston, B.P., Taylor, P.H. and Stansby, P.K. (2006). Solitary wave transformation, breaking and run-up at a beach. Proceedings of the Institution of Civil Engineers, Maritime Engineering 159 Issue MA3, pp. 97-105.

[13] Boussinesq, J. (1871). Théorie de l'intumescence liquide appelée onde solitaire ou de translation, se propageant dans un canal rectangulaire. Comptes Rendus des Séances de l'Académie des Sciences, Paris, 72, pp. 755-759.

[14] Boussinesq, J. (1872). Théorie des ondes et des remous qui se propagent le long d'un canal rectangulaire horizontal, en communiquant au liquide contenu dans ce canal des vitesses sensiblement pareilles de la surface au fond. Journal de Mathématiques Pures et Appliquées 2e série, 17, pp. 55-108.

[15] Bouws, E., Günther, H., Rosenthal, W. and Vincent, C.L. (1985). Similarity of the Wind Wave Spectrum in Finite Depth Water, 1. Spectral Form. J. Geophys. Res., 90, pp. 975-986.

[16] Carrier, G.F. and Greenspan, H.P. (1958). Water waves of finite amplitude on a sloping beach. Journal of Fluid Mechanics, 4(1), pp. 97-109.

[17] Castanedo Bárcena, S. (2000). Desarrollo de un modelo hidrodinámico tridimensional para el estudio de la propagación de ondas largas en estuarios y zonas someras. Tesis doctoral, Escuela Técnica Superior de Ingenieros de Caminos, Canales y Puertos, Universidad de Cantabria, España.

[18] CFE. (2012). Manual De Diseño De Obras Civiles, Sección A: Hidrotecnia, Tema 2: Hidráulica, Capítulo 13: Hidráulica marítima. Comisión Federal de Electricidad, México D.F.

[19] Chamberlain, P.G. and Porter, D. (1995). The modified mild-slope equation. J. Fluid Mech., 291, pp. 393-407.

[20] Chen, Q. (2006). Fully Nonlinear Boussinesq-Type Equations for Waves and Currents over Porous Beds. Journal of Engineering Mechanics, 132(2), pp. 220-230.

[21] Clapeyron, E. (1863). Rapport sur la partie du mémoire de M. Bazin, relative aux remous et à la propagation des ondes. Comptes Rendus des Séances de l'Académie des Sciences, Paris, 57, pp. 302-312.

[22] Cockburn, B. and Shu, C.-W. (1989). TVB Runge-Kutta Local Projection Discontinuous Galerkin Finite Element Method for Conservation Laws II: General Framework. Mathematics of Computation, 52(186), pp. 411-435.

[23] Cockburn, B. and Lin, S.-Y. and Shu, C.-W. (1989). TVB Runge-Kutta Local Projection Discontinuous Galerkin Finite Element Method for Conservation Laws III: One-Dimensional Systems. Journal of Computational Physics, 84, pp. 90-113.

[24] Cockburn, B., Hou, S. and Shu, C.-W. (1990). The Runge-Kutta local projection discontinuous Galerkin finite element method for conservation laws IV: the multidimensional case. Mathematics of Computation, 54(190), pp. 545-581.

[25] Cockburn, B. and Shu, C.-W. (1998a). The Runge-Kutta Discontinuous Galerkin Method for Conservation Laws V: Multidimensional Systems. Journal of Computational Physics, 141, pp. 199-224.

[26] Cockburn, B. and Shu, C.-W. (1998b). The local discontinuous Galerkin method for time-dependent convection-diffusion systems. SIAM J. Numer. Anal., 35(6), pp. 2440-2463.

[27] Cockburn, B. and Shu, C.-W. (2001). Runge-Kutta Discontinuous Galerkin Methods for Convection-Dominated Problems. Journal of Scientific Computing, 16(3), pp. 173-261.

[28] Copeland, G.J.M. (1985). A practical alternative to the "mild-slope" wave equation, Coastal Engineering, 9, pp. 125-149.

[29] Dalrymple, R.A. and Kirby, J.T. (1988). Models for very wide-angle water waves and wave diffraction. J. Fluid Mech., 192, pp. 33-50.

[30] Dalrymple, R.A. (1991). REFRACT: A refraction program for water waves, Version 2.0. CACR Report No. 91-09, Center for Applied Coastal Research, Department of Civil Engineering, University of Delaware, Newark DE USA.

[31] Dean, R.G. (1965). Stream function representation of nonlinear ocean waves. Journal of Geophysical Research, 70, pp. 4561-4572.

[32] Dean, R.G. (1974). Evaluation and development of water wave theories for engineering application. Special Report No. 1, U.S. Army Coastal Engineering Research Center, Ft. Belvoir VA.

[33] Dean, R.G., Dalrymple, R.A. (1991). Water wave mechanics for engineers and scientists, Advanced Series on Ocean Engineering, Vol. 2, World Scientific, Singapore.

[34] DHI Water and Environment. (2007a). Mike 21 EMS, Elliptic Mild-Slope Wave Module, User Guide. DHI software, Danish Hydraulic Institute, Hørsholm Denmark.

[35] DHI Water and Environment. (2007b). Mike 21 PMS, Parabolic Mild-Slope Wave Module, User Guide. DHI software, Danish Hydraulic Institute, Hørsholm Denmark.

[36] DHI Water and Environment. (2007c). Mike 21 BW, Boussinesq Waves Module, User Guide. DHI software, Danish Hydraulic Institute, Hørsholm Denmark.

[37] Dingemans, M.W. (1973). Water wave over uneven bottom; a discussion of long wave equations. Delft Hydraulics Report R729, part 2.

[38] Dingemans, M.W. (1994). Comparison of computations with Boussinesq-like models and laboratory measurements. MAST G8-M Delft Hydraulics, Report H1684.12.

[39] Dingemans, M.W. (1997a). Water wave propagation over uneven bottoms, Part 1 - Linear Wave Propagation, Advanced Series on Ocean Engineering, Vol. 13, World Scientific, Singapore.

[40] Dingemans, M.W. (1997b). Water wave propagation over uneven bottoms, Part 2 - Non-linear Wave Propagation, Advanced Series on Ocean Engineering, Vol. 13, World Scientific, Singapore.

[41] Engsig-Karup, A.P., Hesthaven, J.S., Bingham H.B. and Madsen, P.A. (2006). Nodal DG-FEM solution of high-order Boussinesq-type equations. J. Eng. Math., 56, pp. 351-370.

[42] Engsig-Karup, A.P., Hesthaven, J.S., Bingham H.B. and Warburton T. (2008). DG-FEM solution for nonlinear wave-structure interaction using Boussinesq-type equations. Coastal Engineering, 55, pp. 197-208.

[43] Escudero Castillo, M., Mendoza Baldwin, E., Silva Casarin, R., Posada Vanegas, G., Arganis Juaréz, M. (2012). Characterization of Risks in Coastal Zones: A Review. Clean - Soil, Air, Water, 40(9), pp. 894-905.

[44] Eskilsson, C. and Sherwin, S.J. (2005). Discontinuous Galerkin Spectral/hp Element Modelling of Dispersive Shallow Water Systems. Journal of Scientific Computing, 22-23, pp. 269-288.

[45] Eskilsson, C., Sherwin, S.J. (2006). Spectral/hp discontinuous Galerkin methods for modelling 2D Boussinesq equations. Journal of Computational Physics, 212, pp. 566-589.

[46] Eskilsson, C., Sherwin, S.J., Bergdahl, L. (2006). An unstructured spectral/hp element model for enhanced Boussinesq-type equations. Coastal Engineering, 53, pp. 947-963.

[47] Fenton, J. (1972). A ninth-order solution for the solitary wave. J. Fluid Mech., 53(2), pp. 257-271.

[48] GIOC. (1999). OLUCA-RD, Modelo integral de propagación de oleaje y corrientes en playas. Manual de referencia, Grupo de Ingeniería Oceanográfica y de Costas, Universidad de Cantabria, Ministerio del Medio Ambiente, Santander Cantabria Spain.

[49] GIOC. (2000). OLUCA-SP, Modelo espectral de propagación de oleaje y corrientes en playas. Manual de referencia, Grupo de Ingeniería Oceanográfica y de Costas, Universidad de Cantabria, Ministerio del Medio Ambiente, Santander Cantabria Spain.

[50] Gobbi, M.F., Kirby, J.T. (1999). Wave evolution over submerged sills: tests of a high-order Boussinesq model. Coastal Engineering, 37, pp. 57-96.

[51] Gobbi, M.F., Kirby, J.T. and Wei, G. (2000). A fully nonlinear Boussinesq model for surface waves. Part 2. Extension to O(kh)4. J. Fluid Mech., 405, pp. 181-210.

[52] Hedges, T.S. (1995). Regions of validity of analytical wave theories. Proc. ICE, Water, Maritime and Energy Journal, 112, pp. 111-114.

[53] Holthuijsen, L.H. (2007). Waves in Oceanic and Coastal Waters. Cambridge University Press. Cambridge UK.

[54] Hsiao, S.-C., Liu, P.L.-F. and Chen, Y. (2002). Nonlinear water waves propagating over a permeable bed. Proc. R. Soc. Lond. A, 458, pp. 1291-1322.

[55] Jayasuriya, S. and McCawley, P. (2010). The Asian Tsunami: Aid and Reconstruction after a Disaster, Edward Elgar, Cheltenham Glos UK and Northampton Massachusetts USA.

[56] Kennedy, A.B., Kirby, J.T., Chen, Q., Dalrymple, R.A. (2001). Boussinesq-type equations with improved nonlinear performance. Wave motion, 33, pp. 225-243.

[57] Kim, D.-H., Lynett, P.J., Socolofsky, S.A. (2009). A depth-integrated model for weakly dispersive, turbulent, and rotational fluid flows. Ocean Modelling, 27, pp. 198-214.

[58] Kirby, J.T. (1986a). A general wave equation for waves over rippled beds. J. Fluid Mech., 162, pp. 171-186.

[59] Kirby, J.T. (1986b). Rational approximations in the parabolic equation method for water waves. Coastal Engineering, 10, pp. 355-378.

[60] Kirby, J.T., Wei, G., Chen, Q., Kennedy, A.B., and Dalrymple, R.A. (1998). FUNWAVE 1.0, Fully Nonlinear Boussinesq Wave Model, Documentation and User's Manual. Research Report NO. CACR-98-06, Center for Applied Coastal Research, Department of Civil Engineering, University of Delaware, Newark DE USA.

[61] Kirby, J.T., Dalrymple, R.A. and Shi, F.(2002). Combined Refraction/Diffraction Model, REF/DIF 1, Version 3.0, Documentation and User's Manual. Research Report NO. CACR-02-02, Center for Applied Coastal Research, Department of Civil and Environmental Engineering, University of Delaware, Newark DE USA.

[62] Knauss, J.A. (1996). Introduction to Physical Oceanography, Second Edition. Prentice-Hall, Upper Saddle River NJ USA.

[63] Korteweg, D.J. and de Vries, G. (1895). On the change of form of long waves, advancing in a rectangular canal and on a new type of long stationary waves. Philos. Mag., series 5, 39, pp. 422-443.

[64] Laitone, E.V. (1960). The second approximation to cnoidal and solitary waves. J. Fluid Mech., 9, pp. 430-444.

[65] Lee, J.-J., Skjelbreia, J.E. and Raichlen, F. (1982). Measurement of velocities in solitary waves. Journal of the Waterway, Port, Coastal and Ocean Division, 108(2), pp. 200-218.

[66] LeVeque, R.J. (2002). Finite Volume Methods for Hyperbolic Problems. Cambridge University Press, Cambridge UK.

[67] LeVeque, R.J., George, D.L. and Berger, M.J. (2011). Tsunami modelling with adaptively refined finite volume methods. Acta Numerica, Cambridge University Press, pp. 211-289.

[68] Li, B. and Anastasiou, K. (1992). Efficient elliptic solvers for the mild-slope equation using the multigrid technique. Coastal Engineering, 16(3), pp. 245-266.

[69] Li, B., Reeve, D.E. and Fleming, C.A. (1993). Numerical solution of the elliptic mild-slope equation for irregular wave propagation. Coastal Engineering, 20, pp. 85-100.

[70] Li, B. (1994). A generalized conjugate gradient model for the mild slope equation. Coastal Engineering, 23(3-4), pp. 215-225.

[71] Lin, P. and Liu, P.L.-F. (1998a). A numerical study of breaking waves in the surf zone. J. Fluid Mech., 359, pp. 239-264.

[72] Lin, P. and Liu, P.L.-F. (1998b). Turbulence transport, vorticity dynamics, and solute mixing under plunging waves in surf zone. Journal of Geophysical Research, 103(C8), pp. 15,677-15,694.

[73] Liu, P.L.-F. (1994). Model equations for wave propagation from deep to shallow water. In Advances in coastal engineering (ed. P.L.-F. Liu), 1, pp. 125-157, World Scientific, Singapore.

[74] Liu, P.L.-F., Lin, P., Chang, K.-A. and Sakakiyama, T. (1999). Numerical Modeling of Wave Interaction with Porous Structures. Journal of Waterway, Port, Coastal, and Ocean Engineering, 125(6), pp. 322-330.

[75] Losada, I.J., Silva, R., Losada, M.A. (1996). 3-D non-breaking regular wave interaction with submerged breakwaters. Coastal Engineering, 28, pp. 229-248.

[76] Lynett, P.J. (2002). A multi-layer approach to modeling generation, propagation, and interaction of water waves. Ph.D. thesis, Cornell University.

[77] Lynett, P.J. & Liu, P.L.-F. (2002). Modeling Wave Generation, Evolution, and Interaction with Depth-Integrated, Dispersive Wave Equations, COULWAVE Code Manual, Cornell University Long and Intermediate Wave Modeling Package. School of Civil and Environmental Engineering, Cornell University, Ithaca NY USA.

[78] Lynett, P.J. and Liu, P.L.-F. (2004a). A two-layer approach to wave modelling. Proc. R. Soc. Lond. A, 460, pp. 2637-2669.

[79] Lynett, P.J., Liu, P.L.-F. (2004b). Linear analysis of the multi-layer model. Coastal Engineering, 51, pp. 439-454.

[80] Lynett, P.J., Borrero, J.C., Weiss, R., Son, S., Greer, D., Renteria, W. (2012). Observations and modeling of tsunami-induced currents in ports and harbors. Earth and Planetary Science Letters, 327-328, pp. 68-74.

[81] Madsen, O.S. and Mei, C.C. (1969). The transformation of a solitary wave over an uneven bottom. J. Fluid Mech., 39(4), pp. 781-791.

[82] Madsen, P.A., Murray, R. and Sørensen, O.R. (1991). A new form of the Boussinesq equations with improved linear dispersion characteristics. Coastal Engineering, 15(4), pp. 371-388.

[83] Madsen, P.A. and Sørensen, O.R. (1992). A new form of the Boussinesq equations with improved linear dispersion characteristics. Part 2. A slowly-varying bathymetry. Coastal Engineering, 18(3-4), pp. 183-204.

[84] Madsen, P.A. and Schäffer, H.A. (1998). Higher-order Boussinesq-type equations for surface gravity waves: derivation and analysis. Phil. Trans. R. Soc. Lond. A, 356, pp. 3123-3184.

[85] Madsen, P.A. and Schäffer, H.A. (1999). A review of Boussinesq-type equations for surface gravity waves. In Advances in Coastal and Ocean Engineering (ed. P.L.-F. Liu), 5, pp. 1-94, World Scientific, Singapore.

[86] Madsen, P.A., Bingham H.B. and Liu, H. (2002). A new Boussinesq method for fully nonlinear waves from shallow to deep water. J. Fluid Mech., 462, pp. 1-30.

[87] Madsen, P.A., Bingham, H.B. and Schäffer, H.A. (2003). Boussinesq-type formulations for fully nonlinear and extremely dispersive water waves: derivation and analysis. Proc. R. Soc. Lond. A, 459, pp. 1075-1104.

[88] Madsen, P.A., Fuhrman, D.R., Wang, B. (2006). A Boussinesq-type method for fully nonlinear waves interacting with a rapidly varying bathymetry. Coastal Engineering, 53, pp. 487-504.

[89] Mase, H. and Takeba, K. (1994). Bragg Scattering of Waves over Porous Rippled Bed. Proc 24th ICCE. ASCE, Kobe, Japan, pp. 635-649.

[90] Massel, S.R. (1993). Extended refraction-diffraction equation for surface waves. Coastal Engineering, 19, pp. 97-126.

[91] McCowan, J. (1891). On the solitary wave. London, Edinburgh Dublin Mag. J. Sci., 32, pp. 45-58.

[92] McDaniel, S.T. (1975). Parabolic approximations for underwater sound propagation. J. Acoust. Soc. Am., 58, pp. 1178-1185.

[93] Mei, C.C. and Le Méhauté B. (1966). Note on the Equations of Long Waves over an Uneven Bottom. Journal of Geophysical Research, 71(2), pp. 393-400.

[94] Mei, C.C. (1983). The applied dynamics of ocean surface waves. John Wiley & Sons, New York NY USA.

[95] Nielsen, P., de Brye, S., Callaghan, D.P., Guard, P.A. (2008). Transient dynamics of storm surges and other forced long waves. Coastal Engineering, 55, pp. 499-505.

[96] Nwogu, O. (1993). Alternative Form of Boussinesq Equations for Nearshore Wave Propagation. Journal of Waterway, Port, Coastal, and Ocean Engineering, 119(6), pp. 618-638.

[97] Peregrine, D.H. (1967). Long waves on a beach. J. Fluid Mech., 27(4), pp. 815-827.

[98] Porter, D. and Staziker, D.J. (1995). Extensions of the mild-slope equation. J. Fluid Mech., 300, pp. 367-382.

[99] Posada Vanegas, G., Durán Valdez, G., Silva Casarín, R., Maya Magaña, M.E., Salinas Prieto, J.A. (2010). Vulnerability to coastal flooding induced by tropical cyclones. Proceedings of 32nd Conference on Coastal Engineering, Shanghai, China.

[100] Reed, W.H. and Hill, T.R. (1973). Triangular mesh methods for the neutron transport equation. Los Alamos Scientific Laboratory Report. LA-UR-73-479.

[101] Reeve, D.E., Li, B. and Fleming, C.A. (1996). Validation of storm wave forecasting. Proc. 31st MAFF Conf. River Coastal Eng., Keele, UK, 3-5 july, pp. 4.3.1-4.3.12.

[102] Reeve, D., Chadwick, A. and Fleming, C. (2004). Coastal engineering: processes, theory and design practice, Spon Press, Abingdon Oxon UK.

[103] Rojanakamthorn, S., Isobe, M. and Watanabe, A. (1989). A mathematical model of wave transformation over a submerged breakwater. Coastal Eng. Jpn., 32(2), pp. 209-234.

[104] Rojanakamthorn, S., Isobe, M. and Watanabe, A. (1990). Modeling of wave transformation on submerged breakwater. Proc. 22nd ICCE. ASCE, New-York, USA, pp. 1060-1073.

[105] Ruiz Martínez, G. (2009). Determinación del estado morfodinámico de segmentos de playa que poseen obstáculos sumergidos y emergidos, Tesis Doctoral, Instituto de Ingeniería, Universidad Nacional Autónoma de México, Mexico.

[106] Schäffer, H.A., Madsen, P.A. (1995). Further enhancements of Boussinesq-type equations. Coastal Engineering, 26, pp. 1-14.

[107] Schäffer, H.A. (1996). Second-order wavemaker theory for irregular waves. Ocean Engineering, 23(1), pp. 47-88.

[108] Schröter, A., Mayerle, R. and Zielke, W. (1994). Optimized dispersion characteristics of the Boussinesq wave equations. Proc. Waves - Physical and Numerical Modelling, Vancouver, Canada, pp. 416-425.

[109] Scott Russell, J. (1844). Report on Waves. Fourteenth meeting of the British Association for the Advancement of Science, York, September 1844 (London 1845), pp. 311-390.

[110] Serre, P.F. (1953). Contribution à l'étude des écoulements permanents et variables dans les canaux. La Houille Blanche, pp. 374-388, 830-872.

[111] Shore Protection Manual. (1984). Fourth Edition, 2 Vol., Coastal Engineering Research Center, Department of the Army, Waterways Experiment Station, Corps of Engineers. U.S. Government Printing Office, Washington D.C. USA.

[112] Shu, C.-W. (1987). TVB Uniformly High-Order Schemes for Conservation Laws. Mathematics of Computation, 49(179), pp. 105-121.

[113] Shu, C.-W. (1988). Total-Variation-Diminishing time discretizations. SIAM J. Sci. Stat. Comput., 9, pp. 1073-1084.

[114] Shu, C.-W. and Osher, S. (1988). Efficient Implementation of Essentially Non-oscillatory Shock-Capturing Schemes. Journal of Computational Physics, 77, pp. 439-471.

[115] Silva, R., Salles, P., Palacio, A. (2002). Linear waves propagating over a rapidly vaying finite porous bed. Coastal Engineering, 44, pp. 239-260.

[116] Silva, R., Salles, P., Govaere, G. (2003). Extended solution for waves travelling over a rapidly changing porous bottom. Ocean Engineering, 30, pp. 437-452.

[117] Silva, R., Borthwick, A.G.L., Eatock Taylor, R. (2005). Numerical implementation of the harmonic modified mild-slope equation. Coastal Engineering, 52, pp. 391-407.

[118] Silva, R., Mendoza, E., Losada, M.A. (2006a). Modelling linear wave transformation induced by dissipative structures - Regular waves. Ocean Engineering, 33, pp. 2150-2173.

[119] Silva, R., Losada, M.A., Salles, P. (2006b). Modelling linear wave transformation induced by dissipative structures - Random waves. Ocean Engineering, 33, pp. 2174-2194.

[120] Silva Casarín, R. (2008). Manual del usuario y documento de referencia del programa MWAPO3. Instituto de Ingeniería, Universidad Nacional Autónoma de México, México D.F.

[121] Silva Casarín, R., Mendoza Baldwin, E., Escalante Mancera, E., Mariño Tapia, I., Ruiz Rentería, F. (2009). Oleaje inducido por el huracán Wilma en Puerto Morelos, Quintana Roo, México. Ingeniería hidráulica en México, XXIV(2), pp. 93-109.

[122] Silva Casarin, R., Ruiz Martinez, G., Mariño-Tapia, I., Posada Vanegas, G., Mendoza Baldwin, E., Escalante Mancera, E. (2012). Manmade Vulnerability of the Cancun Beach System: The Case of Hurricane Wilma. Clean - Soil, Air, Water, 40(9), pp. 911-919.

[123] Smith, R. and Sprinks, T. (1975). Scattering of surface waves by a conical island. J. Fluid Mech., 72, pp. 373-384.

[124] Sollitt, C.K. and Cross, R.H. (1972). Wave transmission through permeable breakwaters. Proceedings of the 13th International Conference on Coastal Engineering. ASCE, Vancouver, Canada, pp. 1827-1846.

[125] Sorensen, R.M. (1993). Basic wave mechanics for coastal and ocean engineers. John Wiley & Sons, New York NY USA.

[126] Stokes, G.G. (1847). On the theory of oscillatory waves. Transactions of the Cambridge Philosophical Society, 8, pp. 441-455.

[127] Svendsen, I.A. (1974). Cnoidal waves over a gently sloping bottom. Ser. Pap. 6, Inst. Hydrodyn. and Hydraul. Eng., Technical University of Denmark, Lyngby Denmark.

[128] Synolakis, C.E. (1986). The runup of long waves. California Institute of Technology, Pasadena California USA.

[129] Synolakis, C.E. (1987). The runup of solitary waves. J. Fluid Mech., 185, pp. 523-545.

[130] Tanaka, M. (1986). The stability of solitary waves. Phys. Fluids, 29(3), pp. 650-655.

[131] Wei, G. and Kirby, J.T. (1995). Time-Dependent Numerical Code for Extended Boussinesq Equations. Journal of Waterway, Port, Coastal, and Ocean Engineering, 121(5), pp. 251-261.

[132] Wei, G., Kirby, J.T., Grilli, S.T. and Subramanya R. (1995). A fully nonlinear Boussinesq model for surface waves. Part 1. Highly nonlinear unsteady waves. J. Fluid Mech., 294, pp. 71-92.

[133] Whitham, G.B. (1974). Linear and nonlinear waves. John Wiley & Sons, New York NY USA.

[134] Wiegel, R.L. (1960). A presentation of cnoidal wave theory for practical application. J. Fluid Mech., 7, pp. 273-286.

[135] Wiegel, R.L. (1964). Oceanographical engineering, Prentice-Hall, Englewood Cliffs NJ USA.

[136] Witting, J.M. (1984). A unified model for the evolution of nonlinear water waves. Journal of Computational Physics, 56(2), pp. 203-236.

[137] Xie, J.-J., Liu, H.-W. (2012). An exact analytic solution to the modified mild-slope equation for waves propagating over a trench with various shapes. Ocean Engineering, 50, pp. 72-82.

[138] Xu, Y., Shu, C.-W. (2007). Error estimates of the semi-discrete local discontinuous Galerkin method for nonlinear convection-diffusion and KdV equations. Computer methods in applied mechanics and engineering., 196, pp. 3805-3822.

[139] Xu, Y. and Shu, C.-W. (2010). Local Discontinuous Galerkin Methods for High-Order Time-Dependent Partial Differential Equations. Commun. Comput. Phys., 7(1), pp. 1-46.

[140] Yan, J. and Shu, C.-W. (2002). Local Discontinuous Galerkin Methods for Partial Differential Equations with Higher Order Derivatives. Journal of Scientific Computing, 17(1-4), pp. 27-47.

[141] Zou, Z.L. (1999). Higher order Boussinesq equations. Ocean Engineering, 26, pp. 767-792.

[142] Zou, Z.L. (2000). A new form of higher order Boussinesq equations. Ocean Engineering, 27, pp. 557-575.

[143] Zou, Z.L., Fang, K.Z. (2008). Alternative forms of the higher-order Boussinesq equations: Derivations and validations. Coastal Engineering, 55, pp. 506-521.